University of Texas at Arlington

# MavMatrix

2023

# PROCESS-DRIVEN MICROSTRUCTURE TAILORING DURING ADDITIVE MANUFACTURING OF Ti-6Al-4V

Ahmet Alptug Tanrikulu

Follow this and additional works at: https://mavmatrix.uta.edu/materialscieng_dissertations

Part of the Materials Science and Engineering Commons

## Recommended Citation

**PROCESS-DRIVEN MICROSTRUCTURE TAILORING DURING ADDITIVE**

**MANUFACTURING OF Ti-6Al-4V**

by:

AHMET ALPTUĞ TANRIKULU

DISSERTATION

Submitted in partial fulfillment of the requirements
For the degree of Doctor of Philosophy at
The University of Texas at Arlington
December, 2023

Arlington, Texas

Supervising Committee:

Amerihesam Amerinatanzi, Supervising Professor
Atilla Doğan
Efstathios I. Meletis
Ye Cao
Robert M. Taylor
Yaowu Hao

**ABSTRACT**

PROCESS-DRIVEN MICROSTRUCTURE TAILORING DURING ADDITIVE

MANUFACTURING OF Ti-6Al-4V

Ahmet Alptug Tanrikulu, Ph.D.

The University of Texas at Arlington, 2023

Supervising Professor: Amir Ameri

In recent years, additive manufacturing (AM) has attracted the attention of many researchers due to the technology providing opportunities in terms of improved functionality, production repeatability, efficiency, and cost and time issues. While AM techniques made possible the realization of complex geometries, their use in critical applications have faced challenges due to the anisotropic characteristic of AM-built parts. More specifically, non-equilibrium AM processes involve steep temperature gradients and rapid solidification, yielding a unique microstructure, e.g., columnar-shaped grains with preferred texture, in final AM-built products and hence anisotropic mechanical properties.

Despite significant studies on improving the microstructure of AM-built parts, it remains a major challenge to create products with more isotropic properties. The practiced approaches include optimizing AM process parameters, remelting of each layer during fabrication, or post-process heat treatments. This has raised a question of whether or not it is possible to perform in-situ layerwise microstructure modifications during AM processes, rather than relying only on process parameters optimization, or post-process heat treatment strategies. If successful, it would be possible to create parts with engineered, more isotropic microstructure and properties, e.g., a part with a relatively harder surface for crack initiation resistance and a relatively soft core for high-impact toughness. In addition, the obtained knowledge and understanding could be employed to perform pre-designed local microstructure modifications on each layer of AM, and create composite parts without the use of two single powders.

## DEDICATION

*I dedicate my humble study to my wife Ayça Tanrıkulu, whose enduring support has been my strength, and*

*motivation to give my best.*

*To my cherished son, Kayra Tanrıkulu, whose love warms my heart and encourages me to dedicate myself*

*to my work and my family to be a source of inspiration for him.*

LIST OF FIGURES

LIST OF TABLES

# ABSTRACT

PROCESS-DRIVEN MICROSTRUCTURE TAILORING DURING ADDITIVE

MANUFACTURING OF Ti-6Al-4V

Ahmet Alptug Tanrikulu, Ph.D.

The University of Texas at Arlington, 2023

Supervising Professor: Amir Ameri

In recent years, additive manufacturing (AM) has attracted the attention of many researchers due to the technology providing opportunities in terms of improved functionality, production repeatability, efficiency, and cost and time issues. While AM techniques made possible the realization of complex geometries, their use in critical applications have faced challenges due to the anisotropic characteristic of AM-built parts. More specifically, non-equilibrium AM processes involve steep temperature gradients and rapid solidification, yielding a unique microstructure, e.g., columnar-shaped grains with preferred texture, in final AM-built products and hence anisotropic mechanical properties.

Despite significant studies on improving the microstructure of AM-built parts, it remains a major challenge to create products with more isotropic properties. The practiced approaches include optimizing AM process parameters, remelting of each layer during fabrication, or post-process heat treatments. This has raised a question of whether or not it is possible to perform in-situ layerwise microstructure modifications during AM processes, rather than relying only on process parameters optimization, or post-process heat treatment strategies. If successful, it would be possible to create parts with engineered, more isotropic microstructure and properties, e.g., a part with a relatively harder surface for crack initiation resistance and a relatively soft core for high-impact toughness. In addition, the obtained knowledge and understanding could be employed to perform pre-designed local microstructure modifications on each layer of AM, and create composite parts without the use of two single powders.

**TABLE OF CONTENTS**

# 1.  INTRODUCTION

## 1.1. Motivation

It is always a challenging task to manufacture parts with complex geometries using conventional manufacturing techniques, particularly because of the additional steps that are required such as machining and joining. Additive manufacturing (AM), on the other hand, allows the fabrication of complex shapes with a tremendous degree of flexibility and freedom. AM processes involve rapid solidification and cooling rates, thus creating parts with unique microstructure and preferential texture, totally different from those fabricated conventionally. Such unique microstructure/texture results in anisotropic properties in the final parts, which are not always desirable and need to be addressed at least to some extent.

The literature involves significant work focusing on approaches to improve the microstructure of AM-built parts and create more standard parts with improved mechanical properties and less anisotropic behavior. One widely used technique to regulate the microstructure has been the *changing of AM process parameters*, such as laser power, scan speed, hatch spacing, layer thickness, and scan strategy. While some improvements have been made, it is found that process parameter optimization could not be a good solution, and at least has to be combined with other new strategies. Post-process heat treatments have also been performed on AM-built parts. However, such treatments are found to be undesirable because they are associated with increased time and cost. Particularly, for materials such as titanium that have high oxygen affinity, post-process heat treatments require to be conducted in a furnace with a controlled atmosphere, which makes the process even more costly and time-consuming.

It is ideal to come up with new strategies to control and improve the microstructure during AM processes, rather than relying only on AM process parameters optimization, or post-process heat treatment strategies.  If successful, it would be possible to create parts with engineered microstructure and properties. For example, a part could be designed with different microstructure properties in different regions, like in

1

a composite structure. As another example, a part could be fabricated with a relatively harder surface for crack initiation resistance, and a relatively soft core for high-impact toughness.

## 1.2. Objectives

The primary focus of this research is to perform layerwise microstructure modifications in AM, rather than relying on post-process treatment techniques, with the ultimate goal of improving the mechanical and fatigue properties of AM-fabricated parts. More specifically, this research will address three research objectives: (i) to reveal how pre-heating of each layer could alter the evolution of microstructure, compared to when preheating is not performed, and its subsequent effect on the mechanical and fatigue properties, (ii) to elucidate how pre-heating of each layer, if combined with post-heating of that layer, could improve the microstructure and hence the mechanical, and **(iii)** to unveil how the microstructure modifications, if performed locally such as in composite parts, could influence the anisotropic properties of the final fabricated parts.

## 1.3. Approach

In order to study the identified objectives, a comprehensive literature review was conducted on the topic to learn about the knowledge gaps, to learn from the findings in the literature, and to ensure the proposed methodologies are not studied by other researchers. More specifically, the literature review was conducted on the microstructure properties of AM-built Ti6Al4V parts, beta phase decomposition below the allotropic transformation temperature, slip mechanisms of the Ti-HCP, lattice distortion during the HCP to BCC transformation, martensitic transformation of the Ti6Al4V and mechanical and fatigue responses of unique microstructure of SLM-built Ti6Al4V.

For objective 1, in order to come up with appropriate process parameters for preheating of each layer, a series of samples with different process parameters were first fabricated through a design of experiment methodology, followed by conducting microstructure characterization on those samples. Upon analyzing the microstructure results, different sets of process parameters for the preheating of each layer were identified. Next, a series of microstructure samples were fabricated by performing preheating via the

laser prior to laser melting of each layer. Based upon the obtained microstructure results (i.e., alpha phase lath thickness, HCP lattice parameters, the amount of the alpha and beta phase), a series of tensile coupons were fabricated and the improvement in the mechanical properties was obtained.

Objective 2 aims to explore the in-situ thermal process which combines the preheating and post-heating laser scan application. A combination of different preheating laser scan powers, preheating laser scan speeds, post-heating laser power, and post-heating laser scan speeds derived from a design of experiment method. The microstructure of each different case was evaluated and the best results in terms of internal process-induced defects were selected for further evaluation. A series of microstructure characterization techniques (X-ray diffraction, SEM, image processing, Bragg's law, and Williamson-Hall model) were applied to unveil the effect of the studied in-situ thermal processing on the microstructure and its mechanical response. The tensile testing revealed a significant improvement in the mechanical properties of the material.

A post-heating laser scan was utilized at the selected regions of the specimen's cross-section to modify the microstructure as the third objective of the presented study. Objective 3 aims to mimic the functions of the fibers in composite materials by generating pillar regions with modified microstructure in the specimens. In this novel approach rather than the existing functionally graded material applications the chemical composition of the material did not change. The grain morphology of the material was modified by controlled cooling rates with precise laser parameter tuning. Advanced microstructure characterization was conducted to monitor the impact of the single-material composite metal additive manufacturing application. Results exhibited a remarkable improvement in the mechanical strength of the material as well as in the elongation of the material which makes this application unique.

1.4. Outline

In Chapter 1, the motivation, objectives, approach, and contributions of the present study are discussed. In Chapter 2, a comprehensive literature review on the additive manufacturing of different materials, particularly Ti6Al4V, the microstructure and mechanical properties of AM-built parts, and the knowledge gaps are provided. In Chapter 3, which focuses on studying objective 1, an introduction to the

objective goal, materials and methods, results, discussions, and conclusion are included. In Chapter 4, a novel in-situ thermal process which represents objective 2 of the study was investigated from both microstructure and mechanical property perspectives. Chapter 5 presented Objective 3, which focuses on the impact of the modified microstructure in selective regions of the studied specimens. Finally, in Chapter 6 findings of the Chapter 3,4,5 were summarized and future studies were discussed.

## 1.5. Contribution

The contributions of this study include: (i) Revealing the evolution of microstructure (e.g., allotropic transformation, lattice structure, and interstitial solution) in AM-built Ti6Al4V specimens that are created based on the concept of preheating prior to laser melting. (ii) Revealing the relationships between the process, microstructure, and properties of fabricated specimens, which would enable the design for specific needs. (iii) Enabling the fabrication of composite structures through AM techniques without the need for two different materials.

2.  BACKGROUND AND LITERATURE REVIEW

2.1. Additive Manufacturing (AM) Processes

AM processes involve the fabrication of a three-dimensional part in a layer-by-layer manner. Based upon the ASTM 52900-21, AM is defined as the '*process of joining materials to make parts from 3D model data, usually layer upon layer, as opposed to subtractive manufacturing and formative manufacturing methodologies*' [1]. With the development of stereolithography, the AM technology was invented in the 1980s [2]. This technology became popular during the last few decades, particularly because of its ability to produce parts with complex geometries, which are not achievable using conventional fabrication methods [3]. In the following, an introduction to AM techniques, advantages and disadvantages of these methods, effective parameters that have influence on the properties of final parts, and techniques that have been conducted to improve the microstructure and mechanical properties of Ti6Al4V are presented.

2.1.1. A Brief History of Additive Manufacturing

Charles W. Hull created the first 3D-printed part in 1983 [4] after his invention of stereolithography [5]. One year, after the first 3D printed part was introduced by Hull, Deckard, and Beaman, started to perform research studies on powder materials in 1984 [6,7] using a 100W YAG laser heat source [7]. The results of their work ended up in a patent that was filed in 1989 at the University of Texas at Austin [8,9], which is known as the selective laser sintering (SLS) technology. Six years after this patent invention, in 1995, EOS introduced the first direct metal laser sintering (DMLS) printer [10]. Later in 1999, selective laser melting (SLM) technology was invented by Fockele and Schwarze [11] with the support of the Fraunhofer Institute of Laser Technology [12]. The first commercial SLM 3D printer was released in 2004 by MCP Tooling Technologies, which was named Realizer 250 SLM [12]. Lars-Erik Andersson & Morgan Larsson invented an electron beam heat source for powder-based 3D printing in 2000, which is currently known as the electron beam melting (EBM) process [13]. The EBM technology was later commercialized by Arcam AB (Note: GE acquired the controlling shares of Arcam AB in 2016) by assigning the patent in 2008 [14]. Both SLM and EBM technologies are considered powder bed fusion (PBF) systems.

2.1.2. Recent Trends in AM

AM has gained significant attention in recent years, particularly in industries that require components with complex geometry, such as aerospace, automotive, space, oil and gas, and biomedical industries [15,16]. As a few examples, lightweight components for aerospace engineering [17,18], and tailored body implants for biomedical engineering [19] can be produced using AM techniques due to their capability to fabricate near-net shape complex geometries from CAD data [20–22].

When it comes to complex geometries, conventional subtractive fabrication techniques produce increased material waste and high energy consumption. As an example, it has been reported that the material waste for some components is 30 times higher than the material that is used for the component itself [23]. Nowadays, AM has become one of the most promising technologies for reducing material and energy waste, particularly for parts with complex geometries. Previous studies on metal AM have proved that it is possible to produce lighter parts without sacrificing mechanical strength [24,25].

2.1.3. Advantages and Disadvantages of AM

AM processes offer numerous advantages to a wide variety of industries which makes it a hot topic not only for research studies but also for real engineering applications. To name a few, AM eliminates the need for complementary processes such as assembly, produces near-net shape components with minimal material/waste energy, creates light-weight components and increases the energy efficiency of vehicles, eliminates the additional design process required for molding and machining, enables the fabrication of consolidated multiple parts, and eliminates the multiple production steps and decreases the total production time [26]. These benefits are the main keys that have attracted a wide variety of industries to this technology. The global market for AM was valued at $16.6M in 2020, and according to Mordor Intelligence, it is expected to exceed $70M by 2026 [27].

Despite the extensive benefits and huge market potential for AM, however, there are some challenges associated with the process that need further attention. Rapid solidification and cooling rates associated with AM processes result in unstable microstructure in terms of residual stresses [28] and strains [29]. More specifically, the inherent directional solidification of the process leads to the preferred grain

texture in the microstructure [30], which in turn results in an anisotropic mechanical response in the final part [31]. In addition to the microstructural challenges of the process, the associated staircase effect [32] limits the use of AM for applications that require high-end surface finish quality. Costs associated with feedstock powder material and powder recycling are also further objections to this technology.

## 2.1.4. AM Applications

During the last three decades, extensive research studies on AM have been conducted. Even though this technology has been studied only for a couple of decades, great knowledge and understanding of the material behaviors and mechanical responses of AMed parts are already available, thus leading to the integration of this technology into the industry. In Figure 2.1, several examples of the applications of AM technology in the aerospace and medical industry are provided.
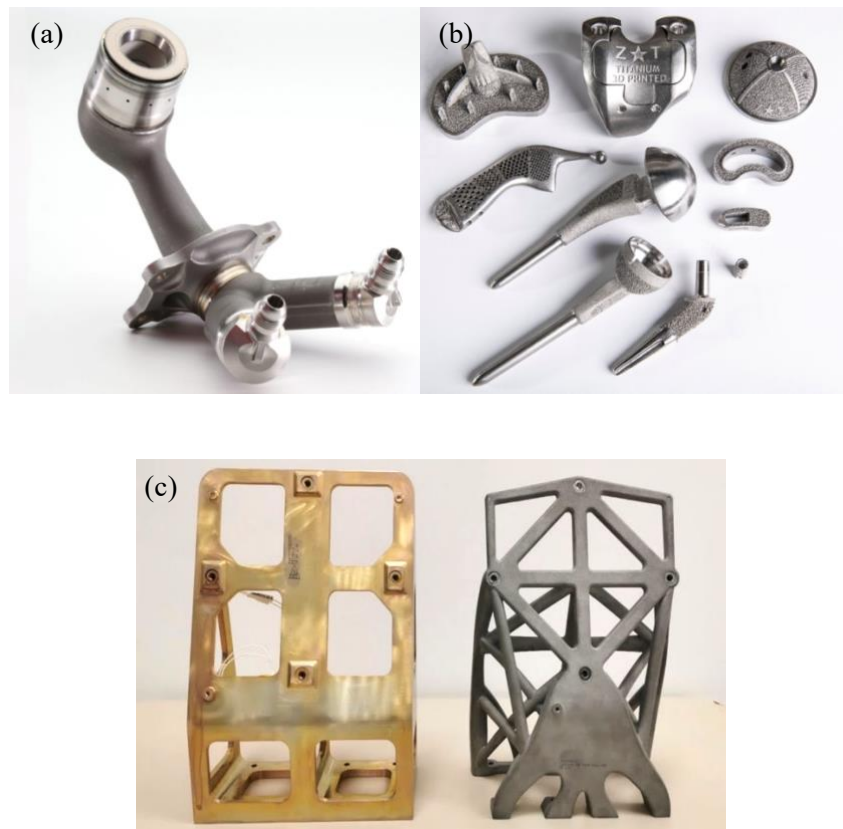


*Figure 2.1. Several applications of the AM technology in the aerospace and medical industry: (a) LEAP fuel nozzle -GE Aerospace [33], (b) Internal body implants by GE Additive Arcam Q10+ [34], and (c) Satellite star tracker bracket produced by conventional and AM processes – Turkish Aerospace [24].*

2.1.5. AM Technologies: State of the Art and Trends

To date, there have been multiple classifications and explanations for AM techniques terminology. The ISO/ASTM 52900:2021 (E) standard, 'Additive Manufacturing – General Principles – Fundamentals and Vocabulary' [1] is one of the most comprehensive references for the terminology and classification of AM technology. According to ASTM, AM can be classified into seven different groups, as outlined in Figure 2.2 [1]. Among these techniques, laser powder bed fusion (LPBF) is the most common and adopted method for the fabrication of metallic components [35]. In the literature, the classification of AM techniques has been done in other ways too, e.g., based on the process steps such as single step versus multi-step, or based on materials such as metal, ceramic, polymer, and composite.
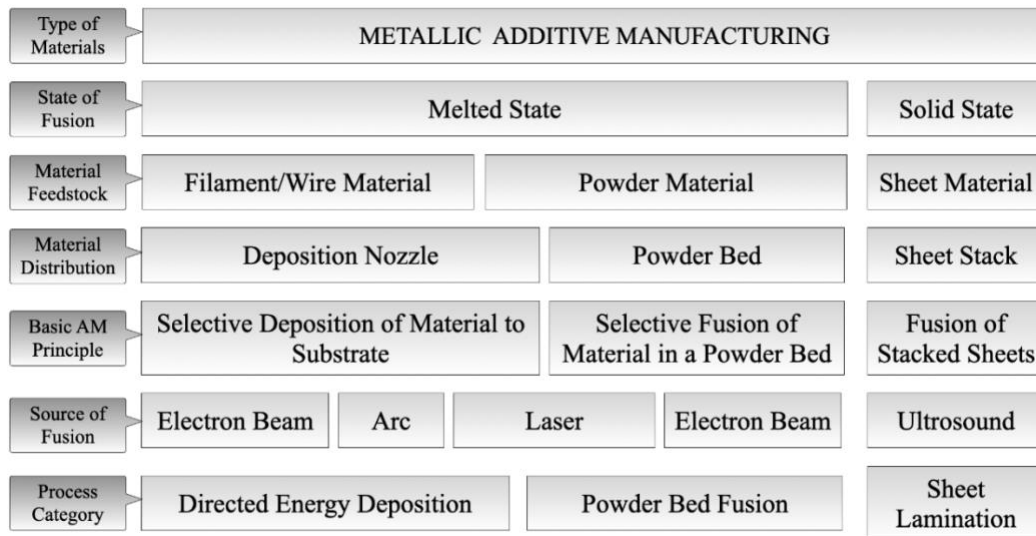


*Figure 2.2. Overview of single-step AM processing principles for metallic materials [1].*

2.1.6. Selective Laser Melting (SLM) Processes

Among different AM technologies, laser powder bed fusion (PBF), particularly selective laser melting (SLM) is one of the most common processes due to its ability to fabricate almost fully dense complex shape components with high dimensional precision [36]. In the SLM processes, a build file must be first created from the CAD data of the part of interest, followed by its slicing according to the set layer thickness, and the laser parameters and path strategy of each layer. The 3D printer software and controllers apply the data of the building file during the process. Additional process parameters such as building plate

preheating temperature and powder spreading-related parameters must also be predefined using the AM software. A schematic view of the PBF systems is depicted in Figure 2.3.
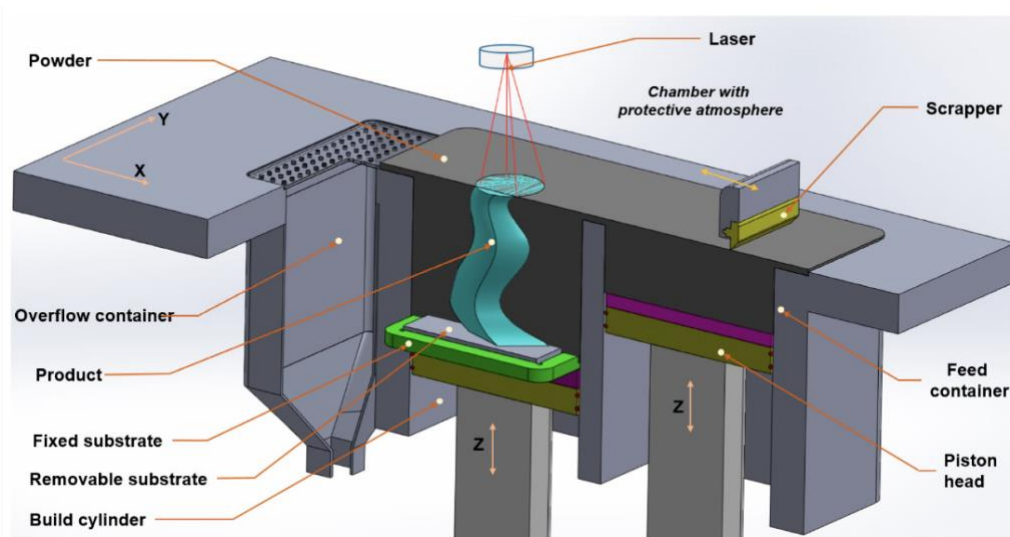


*Figure 2.3. A schematic view of a powder bed fusion (PFB) process inside an AM printer [37].*

One main advantage of SLM processes is its capability to produce high-resolution features and internal design cavities with accurate dimension control [38], along with a wide variety of material selections [39]. When compared to other PBF technologies or EBM methodologies, SLM delivers a significantly denser microstructure because of the relatively high energy input that is used and produces finer geometrical features due to the relatively thinner layer thickness that is employed in this technique.

2.1.7. Effective Parameters in SLM-built Parts

In an SLM process, multiple effective parameters can control the process and result in different microstructural and hence mechanical properties. These parameters include, but are not limited to the laser power, scanning speed, hatch spacing, layer thickness, scanning strategy, laser spot size, and powder particle size. Due to the high number of variables involved, it has not yet been possible to consider all the parameters in a single study. On the other hand, the focus has mainly been on limited parameters that have huge effects on the microstructure and mechanical behavior of the fabricated parts [40]. To simultaneously understand the effects of these parameters, Thijs *et al.* [40] proposed an energy density equation (see

Equation 1), where $E_v$ is the energy density, $P$ is the laser power (W), $v$ is the laser scanning speed (mm/s), $t$ is the layer thickness (mm), and $h$ is the hatch spacing (mm).

$$E_v = \frac{P}{v.h.t}$$ Eq (2.1)

Noteworthy is that, in addition to the energy density parameters, powder material characteristics have also great impacts on the microstructure and mechanical response of SLMed part [41]. In the following, a brief explanation on the influencing parameters in SLM processes is presented.

2.1.7.1. Laser Power and Spot Size

Laser power has an important effect on the melt pool formation during SLM processes, which in turn governs the microstructure of resultant parts. For instance, insufficient laser power results in partial melting of deposited powder particles [42], which in turn causes the formation of bridges between the particles, thereby leading to powder agglomerations [43]. The associated cavities formed between the agglomerated powder lead to an increase in porosity in the final parts [42]. Another example, significantly high laser power promotes the evaporation of materials [44,45] and causes the formation of defects and porosities, incomplete fusion holes, cracks, and impurities [46].

The laser spot size is another important factor in SLM processes, which defines the energy transfer dynamics from the laser source to the surface of the powder layer. The laser spot in SLM applications has a Gaussian energy distribution, in which the point $e^{-2}$ for the laser peak intensity of a beam depicts the diameter of the laser spot size [47]. Since the laser spot transmits the energy of the laser to the powder layer, it has a great impact on heat transfer phenomena. Additionally, it influences the precision and fabrication speed of the SLMed parts. The scan total area depends on the laser spot size.

2.1.7.2. Hatch Spacing

The distance between two neighboring scan tracks is referred to as hatch spacing, hatch distance, or scan spacing. Hatch spacing can be calculated by measuring the distance between the center beams of adjacent scans [48]. There is an adverse relation between the hatch spacing and the fabrication time, which means that the higher the hatch spacing is, the lower is the total fabrication time. In addition to hatch

spacing, there is another parameter that has an important effect on SLMed parts, i.e., the hatch angle, which is the scanning orientation between the consecutive layers. Robinson *et al.* [49] investigated the effect of the hatch angle orientation on SLMed parts and reported that the hatch angle has a great influence on the density, surface finish, and tensile properties of the parts.

2.1.7.3. Layer Thickness

Layer thickness is the dimension of the layer height of each consecutive layer during the SLM process. Because of the associated staircase effect, the higher the level of layer thickness, the rougher the resultant surface is [32,50]. This is of particular importance because the surface finish of the final part has an important effect on the mechanical behavior of the component. As an example, a thicker layer thickness results in a rough surface and hence lower strength and higher plasticity, compared to when a low layer thickness is chosen [50]. In SLM applications layer thickness mostly vary between 20µm to 50µm.

2.1.7.4. Scan Speed

Scanning speed is the laser track velocity during SLM processes, which has a great influence on the heat input, energy density, and fabrication time. A relatively higher scan speed decreases the energy input, which may result in insufficient input heat for the melting of the deposited powder layer. This could be accompanied by a lack of fusion and balling effect during the process [46,51,52]. A lower scan speed increases the energy density and may cause overheating of the powder layer, which could promote material evaporation and porosity formation [46]. In SLM applications, the scan speed is mostly between 800 mm/s to 2000 mm/s depending on the material type, laser power, layer thickness, and scanning strategy.

2.1.7.5. Scan Strategy

Scanning strategy in SLM processes is defined as the route that the laser track follows at each layer according to the part geometry. The starting point of the scan track and the sequence of scanning regions with hatch orientation and hatch distance compose the scan strategy. Additionally, the contour, upper, and down skin scans can be considered as other elements of the scanning strategy. The selection of these variables designates the degree of distortion, residual stress formation, and strains of the final part. Thus,

the optimization of these parameters is essential for a reliable fabrication. In SLM processes, the high energy input at confined regions and uneven temperature distributions lead to high-temperature gradient, thermal stress, and warpage, all of which have to be taken into account when optimizing the scan strategy [53].

2.1.7.6. Powder Particle Morphology

It is essential to understand the feedstock decently for a reliable and successful SLM process [41]. It is known that the features of material powders, such as the grain size and shape, have a significant effect on the final parts' densification and mechanical properties [54]. Particle size distribution (PSD) has an important effect on many SLM aspects [41], where smaller particles promote the deposition of a thin layer and enhance the mechanical properties and surface roughness, while the distribution of particles directly affects the packing density of the building plate and the density of the final parts [55,56]. Attar *et al.* [57] reported that the density of the fabricated samples with irregular particles was 95%, while the density of fabrication with spherical particles was 99.5%.

2.2 AM and particularly SLM of Ti6Al4V materials

2.2.1 Brief Introduction to Ti6Al4V Materials

Titanium alloys became popular in the twentieth century, right after modern engineering practice supported their use [58]. These alloys have particularly found great applications in military applications, such as the SR-71 Blackbird [59] and B-1B bomber [60], as well as in commercial aerospace industrial applications such as the Boeing 777 [60].

Among different titanium alloys, Ti6Al4V has been found to be the most commonly used material in critical applications such as the aerospace and biomedical industries. Ti6Al4V has currently almost half of the market share of titanium products available all over the world [61,62]. This alloy is of particular interest, mainly due to its superior properties, including but not limited to exclusive strength [63–65], exceptional corrosion resistance [66], good fatigue performance [21,22,67,68], excellent crack initiation [69,70], and crack propagation resistance [71–73]. Table 1 summarized the chemical compositions of the

Ti6Al4V alloy, which is also referred to as Ti Grade 5.  Noteworthy is that there are different sub-gradings

available for Ti6Al4V, which is categorized based on its oxygen content.

*Table 2.1 Chemical Composition of Ti6Al4V Grade 5 (wt.%) [74]*

| Element (%) | Ti | Al | V | O | N | C | H | Fe | Y | Other elements (each) | Other elements (total) |
|---|---|---|---|---|---|---|---|---|---|---|---|
| Min. | | 5.5 | 3.5 | - | - | - | - | - | - | - | - |
| | Bal. | | | | | | | | | | |
| Max. | | 6.75 | 4.5 | 0.2 | 0.05 | 0.08 | 0.02 | 0.3 | 0.005 | 0.1 | 0.4 |

2.2.2. Microstructure of Ti6Al4V

2.2.2.1. Lattice Structure and Allotropic Transformation

Titanium is an allotropic element, which means it can exist in more than one physical form at one

physical state. In Ti6Al4V, this ability is associated with two different phases at solid-state, i.e., the alpha

phase, and the beta phase. The stability of these phases highly depends on the temperature conditions.

However, the beta phase is the only stable phase at elevated temperatures, both alpha and beta phases

become stable at room temperature (RT). The critical temperature that drives this transformation is called

beta-transus temperature, which is typically higher than $\geq 882.5$ °C [62].

The main difference between the two phases is that the α-Ti has a hexagonal closed pack (HCP)

lattice structure, on the other hand, the β-Ti has a body-centered cubic (BCC) lattice structure. The unit cell,

lattice parameters, and the densest packed planes are shown in Figure 2.4.
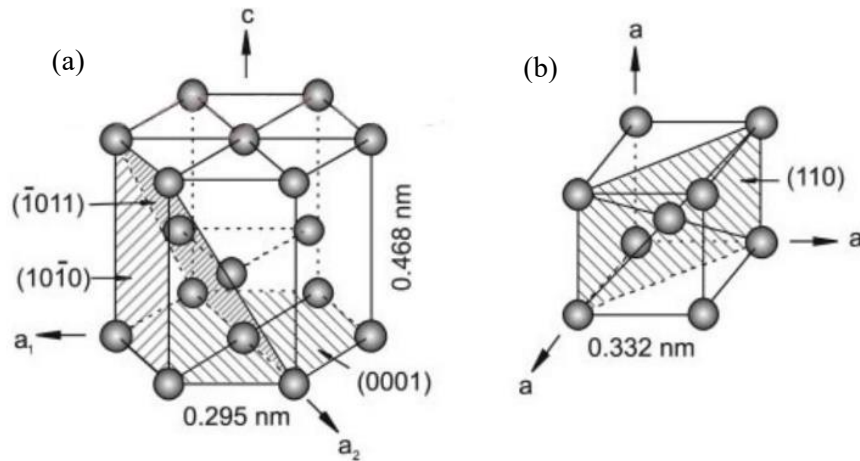
*Figure 2.4. The unit cells of (a) α phase Ti6Al4V and (b) β phase Ti6Al4V.*

The phases have different lattice structures due to their atomic arrangement. There is an orientation relationship with the phases during the allotropic transformation (Tiα ↔ Tiβ). The idealized orientation relation is shown in Figure 2.5 for the α phase (blue lines) and β phase (pink lines).
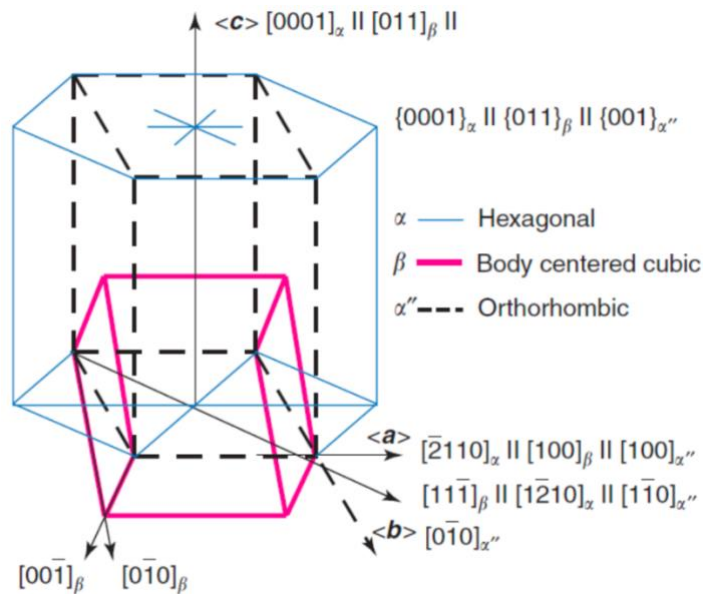


*Figure 0.5*

*Figure 2.5. Idealized orientation relation of the Tiα and Tiβ phases during the allotropic phase transformation of Ti6Al4V [75].*

It is known that the β phase is stable above the allotropic transformation temperature, and α → β transformation happens by heating the temperature above the β-transus temperature. During this phase transformation, the HCP lattice expands approximately 10% along $[2\bar{1}\bar{1}0]_\alpha$ to become a $[100]_\beta$ direction, approximately 10% contraction along the $[0110]_\alpha$ and approximately 1% contraction along the $[0001]_\alpha$ to become a $[01\bar{1}]_\beta$. Due to the mismatch relations, one of the two $<111>_\beta$ directions in the {110} plane is rotated ~5° to align the $<\bar{2}110>_\alpha$ directions [75].

The full transformation between the α phase (α→β→α) happens regardless of the production or thermal profile, since this is a thermo-kinetic driven behavior of the material [76]. The microstructure can be tailored by controlling the cooling rate of the β→α+β decomposition [77,78]. The α phase precipitates from the β matrix in the shapes of laths or plates, which is driven by the cooling rate. But, if the transformation happens as the decomposition of the β phase (β→α+β), this makes it possible to manipulate the microstructure by controlling the cooling rate. Burgers explained the precipitation of the α phase with Burgers orientation relations between the α and β phases [79]. But if the transformation happens as the decomposition of the β phase(β→α+β), this makes it possible to manipulate the microstructure by controlling the rate. Burgers explained precipitation of the α phase with Burgers orientation relations between α and β phase [79].

There are 6 distinct {110} planes in the BCC structure of the β phase, and according to the Burgers orientation, all of them can be the basal plane of the inherited α phase during the transformation [80]. Each of these planes ({110}) contains two <111> direction, which determines $<11\bar{2}0>$ directions of the inherited α phase. Thus, there are 12 unique α (HCP) variants that can be formed from a single β phase (BCC) [80].

2.2.2.2. Grain Structure of Ti6Al4V

The grain structure determines the mechanical response of the material under certain circumstances. Grain morphology is a result of both the composition and thermomechanical process. Grain size, shape, and orientation are the features that define grain morphology. Grain morphology need to be well-understood to enable material design and production steps, as well as the standardization of engineering applications.

The α phase is stable at the RT, and occupies the majority of the microstructure depending on the thermal history of the material. The amount of the α phase in the microstructure may exceeds 87% of the total microstructure volume [81]. The α phase consists of plates that nucleate and grow through the β phase. The diffusional nucleation and growth of the α phase are shown in Figure 2.6 [58].
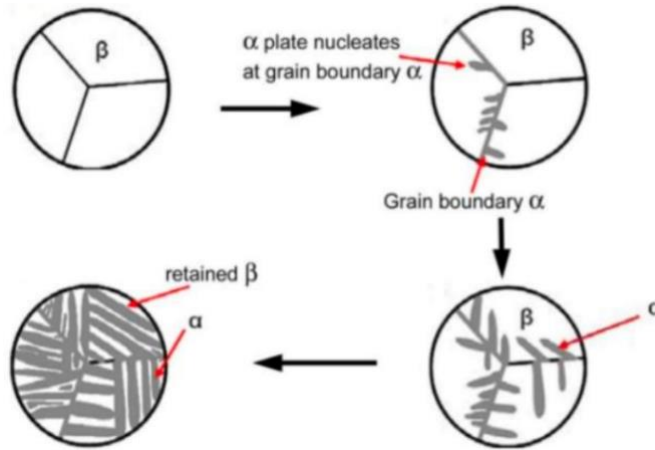


*Figure 2.6. Nucleation and growth of α precipitates initiates from the grain boundary into β grain [82,83].*

Due to the cooling rates α phase can decompose as thicker laths (it is known as the widmanstätten microstructure) [84] at slower cooling rates or thinner lamellae colonies at higher cooling rates as a martensitic microstructure [85].
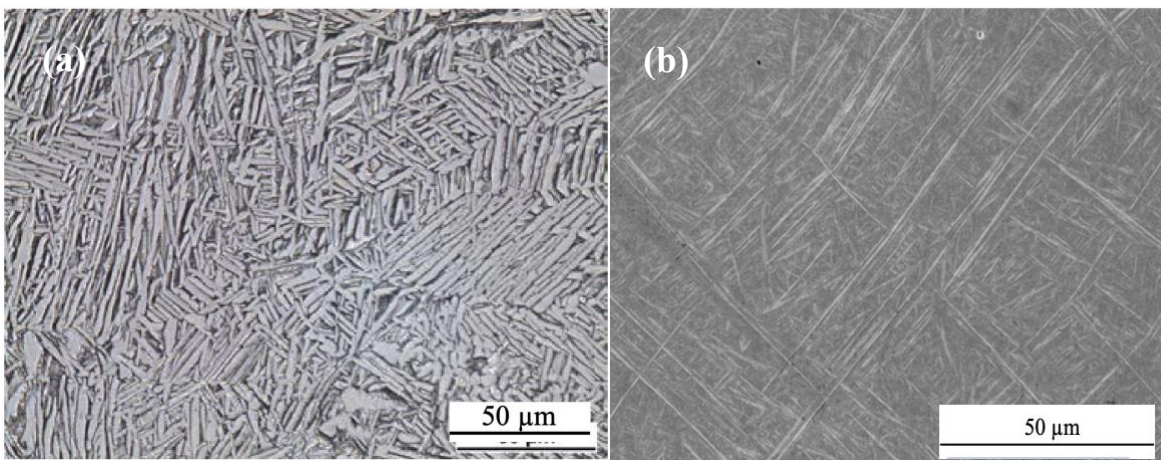


*Figure 2.7. Grain morphology of α phase (a) thicker laths (widmanstätten) [84] (b) martensite [86].*

2.2.3 SLM processing of Ti6Al4V

Compared to other AM techniques, SLM involves relatively lower thicknesses and hence provides parts with higher resolution [87]. This feature has enabled the fabrication of very complex parts using this technology [88]. Due to the inherent staircase effect, as discussed earlier, a relatively thinner layer thickness is favorable for creating fine features, and results in a better surface finish in terms of the final roughness. When it comes to SLMed Ti6Al4V, numerous applications have been explored, including but limited to the airframe parts in the aerospace industry (e.g., aircraft bracket [89]).

Even though SLMed Ti6Al4V materials provide lightweight properties and adequate strength, there are some challenges associated with the thermal analog of the process. Thermal history plays a significant role in the microstructure of Ti6Al4V due to the decomposition mechanisms and allotropic transformation abilities of the material (see section 2.2.2.1), and hence significantly influences the resultant mechanical response. In addition to the lattice transformation and deformations orientation of the grain formed during the directional solidification, cooling has also a significant effect on the mechanical properties of the final product and needs to be fully understood by AM engineers [90,91].

2.3. Microstructure Modification Strategies in SLM Processing of Ti6Al4V

Compared to conventionally fabricated Ti6Al4V components, those produced using SLM techniques contain very complicated microstructure with a high amount of residual stresses, process-induced defects, distortions, and preferred grain texture due to the involved thermal gradient, rapid solidification, and cooling rates. There are standardized complimentary post-processes for SLMed Ti6Al4V, e.g., heat treatment processes [92] to improve the microstructure stability. However, these processes increase the lead time and cost of the total fabrication, which in turn diminishes the competitiveness of SLM with conventional production. Titanium has an oxygen affinity, listed at the fourth place in the Ellingham diagram [93], hence it is required to consider a controlled atmosphere for the thermal processing of these alloys.

Due to the challenges with post-process heat treatment techniques, and to avoid the additional cost and time of post-processing, several research studies in the literature have focused on techniques to modify

the microstructure during the process. In SLM processes, it is possible to change the equivalent properties of a part in its different regions by considering functionally graded materials (FGM). Thanks to the controllable process of SLM, the modification of microstructure in these techniques has also been conducted by manipulating the process parameters. In the following, brief descriptions of techniques that have been employed in the literature regarding this topic are presented.

2.3.1. Structurally-driven Microstructure Tailoring

The development of Functionally Graded Materials (FGM) has been made possible with the advent of AM and more particularly SLM techniques. The production of structurally engineered FGMs (Figure 2.8) could be a substitute for other strategies that involve adding elements or compounds to engineer the microstructure of parts. In other words, since real-time composition control in powder-bed SLM processes is not achievable, the production of compositionally engineered FGMs cannot be achieved using this technique [94]. The production of structurally engineered FGMs in SLM is through introducing porosities into the CAD file and accordingly engineering them (Figure 2.9). An example could be the FGM structures that deliver different functionalities for biomedical scaffolds [95,96].
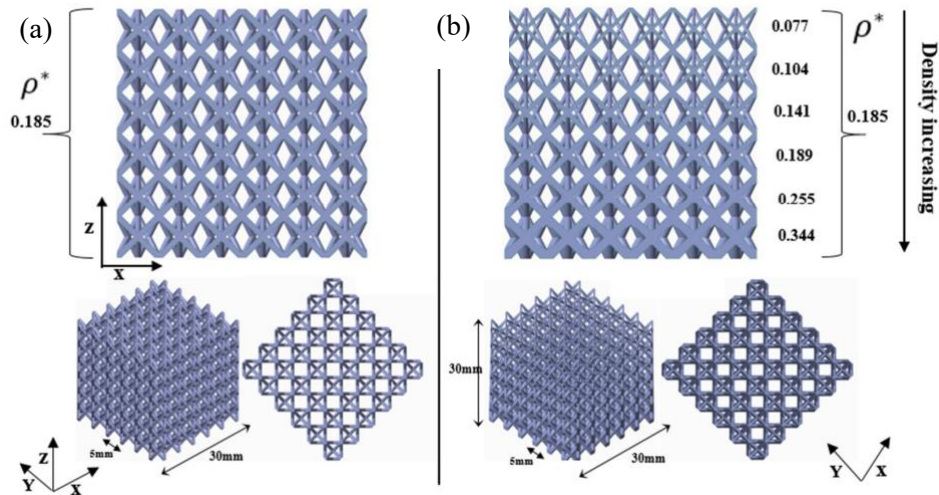


*Figure 2.8. Structurally-engineered structures: (a) uniform lattice structures, and (b) functionally graded FGM structures [97].*
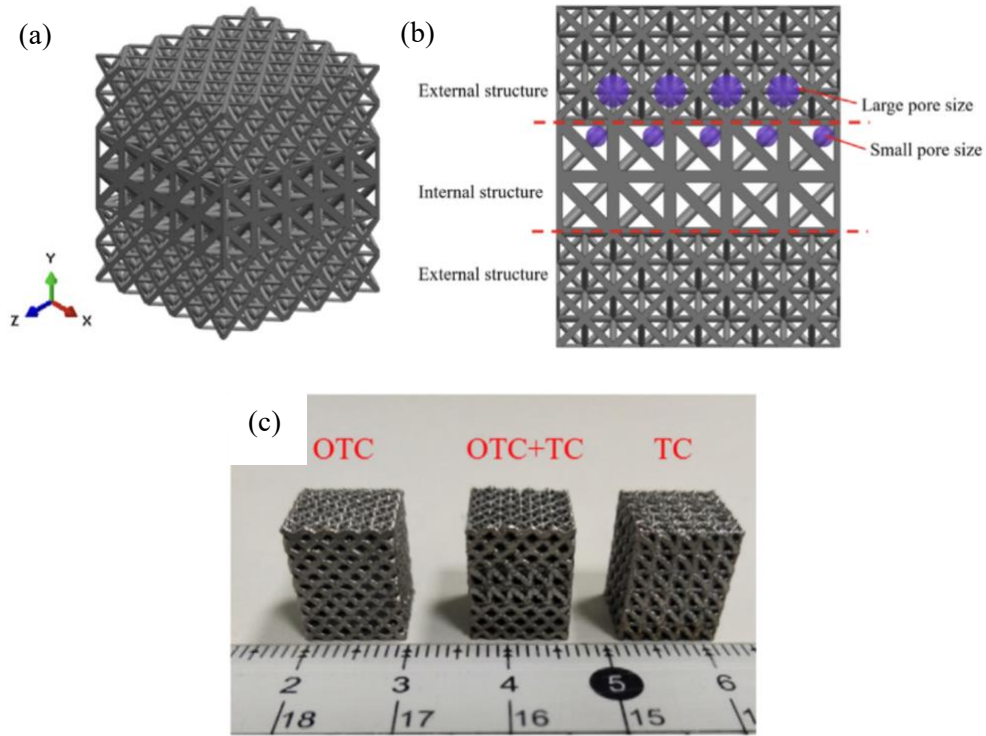
*Figure 2.9. Structurally-driven FGM structures: (a) CAD Model of Tetrahedron cell (TC) + Octet truss cell (OTC), (b) the X-Y plane view of the transition between different lattice structures, and (c) AM-built FGM structures with different types, i.e., OTC, OTC + TC and TC [98].*

2.3.2. Remelting-Driven Microstructure Tailoring

It has been reported in the literature that it is possible to perform remelting on each fabricated layer during the SLM process to improve the microstructure and mechanical properties, e.g., surface finish [99], higher ultimate tensile strength (UTS) [100], and porosity level [101]. Yasa *et al.* [99] has reported that layerwise remelting could enhance the surface quality by 90%, and drastically decrease the porosity level from the range of 1-2% to almost 0%. Bedmar *et al.* [101] have reported that remelting could improve the relative density of Ti6Al4V from 89.7% to 95.3%. Karimi *et al.* [100] have found that remelting could result in a 10% improvement in the UTS value.
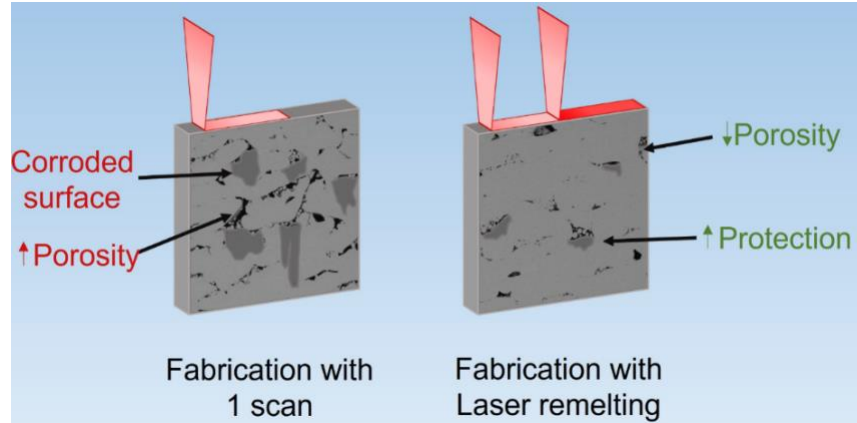
*Figure 2.10. Schematic view of how the remelting concept could be implemented [101].*

2.3.3. Computational Modeling of the LPBF-fabricated Ti-6Al-4V

Due to the complexity of LPBF technology, which involves multi-physics dynamics, process modeling remains a challenging task. Some studies reported the single-track melt pool model or a limited number of multi-track applications which delivers some predictions regarding the final microstructure [102–105]. Kang *et al.* [103] reported that additional scan has a noteworthy effect on grain structure. It was reported that the additional laser scan refines the grains in the microstructure. Additionally, it was reported that selected process parameters are highly sensitive to the thermal conductivity of the material [105]. In the shed of these numeric models experimental studies were conducted.

2.3.4 Knowledge gap Related to Microstructure Tailoring of Ti6Al4V

It is known from the literature that the microstructure of Ti6Al4V can be manipulated during the $\beta \rightarrow \alpha + \beta$ decomposition [77,78] by controlling the precipitation and growth rates. Even though several studies have been conducted in the literature to regulate the microstructure during AM processes and particularly SLM, such as engineering the structure and creating FGM structures, or performing remelting on each layer to improve the microstructure, no research study has been conducted to perform in-situ layer-by-layer heat treatment with different sequences and laser parameters. The knowledge gaps in the literature are identified as follows: (i) no research has been conducted to perform in-situ layerwise microstructure modifications, such as by manipulating the solubility of the HCP lattice during the decomposition from

20

BCC to HCP and revealing its impact on the anisotropic mechanical behavior of SLM-built Ti6Al4V material.

## 2.4. References

1.  *Additive Manufacturing-General Principles-Fundamentals and Vocabulary 1,2*;
2.  Thomas, D.S.; Gilbert, S.W. *Costs and Cost Effectiveness of Additive Manufacturing*; Gaithersburg, MD, 2014;
3.  Shah, P.; Racasan, R.; Bills, P. Comparison of Different Additive Manufacturing Methods Using Computed Tomography. *Case Studies in Nondestructive Testing and Evaluation* **2016**, *6*, 69–78, doi:https://doi.org/10.1016/j.csndt.2016.05.008.
4.  *ASME Historic Mechanical Engineering Landmark Stereolithography The First 3D Printing Technology*;
5.  Hull, C.W.; Arcadia, C. *United States Patent (19) Hull (54) (75) (73) 21) 22 (51) 52) (58) (56) APPARATUS FOR PRODUCTION OF THREE-DMENSONAL OBJECTS BY STEREO THOGRAPHY*;
6.  Bandyopadhyay, A.; Vahabzadeh, S.; Shivaram, A.; Bose, S. Three-Dimensional Printing of Biomaterials and Soft Materials. *MRS Bull* **2015**, *40*, 1162–1169, doi:10.1557/mrs.2015.274.
7.  Thakare, S.H. *EXPERIMENTAL INVESTIGATION OF EFFECT OF SUPPORT STRUCTURE GEOMETRY ON THE MICROSTRUCTURE AND METALLURGICAL PROPERTIES OF IN718 PARTS FABRICATED BY SELECTIVE LASER MELTING*; 2020;
8.  US4863538.
9.  Kabir, S.M.F.; Mathur, K.; Seyam, A.-F.M. A Critical Review on 3D Printed Continuous Fiber-Reinforced Composites: History, Mechanism, Materials and Properties. *Compos Struct* **2020**, *232*, 111476, doi:https://doi.org/10.1016/j.compstruct.2019.111476.
10. EOS GmbH – Taking the Laser Lead. *Metal Powder Report* **2014**, *69*, 24–27, doi:https://doi.org/10.1016/S0026-0657(14)70132-8.
11. Yap, C.Y.; Chua, C.K.; Dong, Z.L.; Liu, Z.H.; Zhang, D.Q.; Loh, L.E.; Sing, S.L. Review of Selective Laser Melting: Materials and Applications. *Appl Phys Rev* 2015, *2*.
12. Neikov, O.D. Chapter 13 - Powders for Additive Manufacturing Processing. In *Handbook of Non-Ferrous Metal Powders (Second Edition)*; Neikov, O.D., Naboychenko, S.S., Yefimov, N.A., Eds.; Elsevier: Oxford, 2019; pp. 373–399 ISBN 978-0-08-100543-9.
13. Harun, W.S.W.; Manam, N.S.; Kamariah, M.S.I.N.; Sharif, S.; Zulkifly, A.H.; Ahmad, I.; Miura, H. A Review of Powdered Additive Manufacturing Techniques for Ti-6al-4v Biomedical Applications. *Powder Technol* **2018**, *331*, 74–97, doi:https://doi.org/10.1016/j.powtec.2018.03.010.
14. *Patent Application Publication*; 2010;
15. He, Y.; Montgomery, C.; Beuth, J.; Webler, B. Melt Pool Geometry and Microstructure of Ti6Al4V with B Additions Processed by Selective Laser Melting Additive Manufacturing. *Mater Des* **2019**, *183*, 108126, doi:10.1016/j.matdes.2019.108126.
16. Salmi, M. Design and Applications of Additive Manufacturing and 3D Printing. *Designs (Basel)* **2022**, *6*, 4–7, doi:10.3390/designs6010006.
17. Zhu, L.; Li, N.; Childs, P.R.N. Light-Weighting in Aerospace Component and System Design. *Propulsion and Power Research* **2018**, *7*, 103–119, doi:https://doi.org/10.1016/j.jppr.2018.04.001.
18. Seabra, M.; Azevedo, J.; Araújo, A.; Reis, L.; Pinto, E.; Alves, N.; Santos, R.; Pedro Mortágua, J. Selective Laser Melting (SLM) and Topology Optimization for Lighter Aerospace Componentes. *Procedia Structural Integrity* **2016**, *1*, 289–296, doi:10.1016/j.prostr.2016.02.039.
19. Munsch, M. 15 - Laser Additive Manufacturing of Customized Prosthetics and Implants for Biomedical Applications. In *Laser Additive Manufacturing*; Brandt, M., Ed.; Woodhead Publishing, 2017; pp. 399–420 ISBN 978-0-08-100433-3.

20. Gong, H.; Rafi, K.; Gu, H.; Janaki Ram, G.D.; Starr, T.; Stucker, B. Influence of Defects on Mechanical Properties of Ti-6Al-4V Components Produced by Selective Laser Melting and Electron Beam Melting. *Mater Des* **2015**, *86*, 545–554, doi:10.1016/j.matdes.2015.07.147.

21. Leuders, S.; Thöne, M.; Riemer, A.; Niendorf, T.; Tröster, T.; Richard, H.A.; Maier, H.J. On the Mechanical Behaviour of Titanium Alloy TiAl6V4 Manufactured by Selective Laser Melting: Fatigue Resistance and Crack Growth Performance. *Int J Fatigue* **2013**, *48*, 300–307, doi:10.1016/j.ijfatigue.2012.11.011.

22. Agius, D.; Kourousis, K.I.; Wallbrink, C. A Review of the As-Built SLM Ti-6Al-4V Mechanical Properties towards Achieving Fatigue Resistant Designs. *Metals (Basel)* **2018**, *8*, doi:10.3390/met8010075.

23. Herranz, S.; Campa, F.J.; Lacalle, L.N.L. de; Rivero, A.; al, et The Milling of Airframe Components with Low Rigidity: A General Approach to Avoid Static and Dynamic Problems. *Proceedings of the Institution of Mechanical Engineers* **2005**, *219*, 789–801.

24. Gökdağ, İ.; İzgü, O.; Dağkolu, A.; Tanrıkulu, A.A.; Acar, E. Design Optimization and Validation for Additive Manufacturing: A Satellite Bracket Application. *Structural and Multidisciplinary Optimization* **2022**, *65*, 237, doi:10.1007/s00158-022-03345-3.

25. Orme, M.E.; Gschweitl, M.; Ferrari, M.; Madera, I.; Mouriaux, F. Designing for Additive Manufacturing: Lightweighting through Topology Optimization Enables Lunar Spacecraft. *Journal of Mechanical Design, Transactions of the ASME* **2017**, *139*, doi:10.1115/1.4037304.

26. Attaran, M. The Rise of 3-D Printing: The Advantages of Additive Manufacturing over Traditional Manufacturing. *Bus Horiz* **2017**, *60*, 677–688, doi:10.1016/j.bushor.2017.05.011.

27. Mordor Intelligence Additive Manufacturing & Materials Industry Overview.

28. Xiao, Z.; Chen, C.; Zhu, H.; Hu, Z.; Nagarajan, B.; Guo, L.; Zeng, X. Study of Residual Stress in Selective Laser Melting of Ti6Al4V. *Mater Des* **2020**, *193*, 108846, doi:https://doi.org/10.1016/j.matdes.2020.108846.

29. Ma, Q.P.; Mesicek, J.; Fojtik, F.; Hajnys, J.; Krpec, P.; Pagac, M.; Petru, J. Residual Stress Build-Up in Aluminum Parts Fabricated with SLM Technology Using the Bridge Curvature Method. *Materials* **2022**, *15*, doi:10.3390/ma15176057.

30. Wang, Y.; Yu, C.; Xing, L.; Li, K.; Chen, J.; Liu, W.; Ma, J.; Shen, Z. Grain Structure and Texture of the SLM Single Track. *J Mater Process Technol* **2020**, *281*, 116591, doi:https://doi.org/10.1016/j.jmatprotec.2020.116591.

31. Deev, A.A.; Kuznetcov, P.A.; Petrov, S.N. Anisotropy of Mechanical Properties and Its Correlation with the Structure of the Stainless Steel 316L Produced by the SLM Method. *Phys Procedia* **2016**, *83*, 789–796, doi:https://doi.org/10.1016/j.phpro.2016.08.081.

32. Charles, A.; Elkaseer, A.; Müller, T.; Thijs, L.; Torge, M.; Hagenmeyer, V.; Scholz, S. A Study of the Factors Influencing Generated Surface Roughness of Downfacing Surfaces in Selective Laser Melting.; Research Publishing Services, October 5 2018; pp. 327–330.

33. Rick Kennedy Outside the Box: How GE Aviation Entered the Brave New World of Additive Manufacturing.

34. LESLIE LANGNAU For Metal Additive Manufacturing, Medical Drives Demand.

35. Prashanth, K.G. Selective Laser Melting: Materials and Applications. *Journal of Manufacturing and Materials Processing* **2020**, *4*, 15–17, doi:10.3390/jmmp4010013.

36. Schmidt, M.; Merklein, M.; Bourell, D.; Dimitrov, D.; Hausotte, T.; Wegener, K.; Overmeyer, L.; Vollertsen, F.; Levy, G.N. Laser Based Additive Manufacturing in Industry and Academia. *CIRP Annals* **2017**, *66*, 561–583, doi:https://doi.org/10.1016/j.cirp.2017.05.011.

37. Park, H.-S.; Nguyen, D.-S. Study on Flaking Behavior in Selective Laser Melting Process. *Procedia CIRP* **2017**, *63*, 569–572, doi:https://doi.org/10.1016/j.procir.2017.03.146.

38. Frazier, W.E. Metal Additive Manufacturing: A Review. *J Mater Eng Perform* **2014**, *23*, 1917–1928, doi:10.1007/s11665-014-0958-z.

39. Spierings, A.B.; Wegener, K.; Levy, G. *Designing Material Properties Locally with Additive Manufacturing Technology SLM*;

40. Thijs, L.; Verhaeghe, F.; Craeghs, T.; Humbeeck, J. Van; Kruth, J.-P. A Study of the Microstructural Evolution during Selective Laser Melting of Ti–6Al–4V. *Acta Mater* **2010**, *58*, 3303–3312, doi:https://doi.org/10.1016/j.actamat.2010.02.004.

41. Pleass, C.; Jothi, S. Influence of Powder Characteristics and Additive Manufacturing Process Parameters on the Microstructure and Mechanical Behaviour of Inconel 625 Fabricated by Selective Laser Melting. *Addit Manuf* **2018**, *24*, 419–431, doi:https://doi.org/10.1016/j.addma.2018.09.023.

42. Greco, S.; Gutzeit, K.; Hotz, H.; Kirsch, B.; Aurich, J.C. Selective Laser Melting (SLM) of AISI 316L—Impact of Laser Power, Layer Thickness, and Hatch Spacing on Roughness, Density, and Microhardness at Constant Input Energy Density. *International Journal of Advanced Manufacturing Technology* **2020**, *108*, 1551–1562, doi:10.1007/s00170-020-05510-8.

43. Shen, Y.F.; Gu, D.D.; Pan, Y.F. Balling Process in Selective Laser Sintering 316 Stainless Steel Powder. *Key Eng Mater* **2006**, *315–316*, 357–360, doi:10.4028/www.scientific.net/KEM.315-316.357.

44. Rai, R.; Elmer, J.W.; Palmer, T.A.; DebRoy, T. Heat Transfer and Fluid Flow during Keyhole Mode Laser Welding of Tantalum, Ti–6Al–4V, 304L Stainless Steel and Vanadium. *J Phys D Appl Phys* **2007**, *40*, 5753–5766, doi:10.1088/0022-3727/40/18/037.

45. Metel, A.; Stebulyanin, M.; Fedorov, S.; Okunkova, A. Power Density Distribution for Laser Additive Manufacturing (SLM): Potential, Fundamentals and Advanced Applications. *Technologies (Basel)* **2018**, *7*, 5, doi:10.3390/technologies7010005.

46. Zhang, B.; Li, Y.; Bai, Q. Defect Formation Mechanisms in Selective Laser Melting: A Review. *Chinese Journal of Mechanical Engineering (English Edition)* 2017, *30*, 515–527.

47. Liu, J.M. Simple Technique for Measurements of Pulsed Gaussian-Beam Spot Sizes. *Opt Lett* **1982**, *7*, 196–198, doi:10.1364/OL.7.000196.

48. Cao, B.; Bae, M.; Sohn, H.; Choi, J.; Kim, Y.; Kim, J.; Noh, J. Design and Performance of a Focus-Detection System for Use in Laser Micromachining. *Micromachines (Basel)* **2016**, *7*, 2, doi:10.3390/mi7010002.

49. Robinson, J.H.; Ashton, I.R.T.; Jones, E.; Fox, P.; Sutcliffe, C. The Effect of Hatch Angle Rotation on Parts Manufactured Using Selective Laser Melting. *Rapid Prototyp J* **2019**, *25*, 289–298, doi:10.1108/RPJ-06-2017-0111.

50. Sufiiarov, V.Sh.; Popovich, A.A.; Borisov, E. V; Polozov, I.A.; Masaylo, D. V; Orlov, A. V The Effect of Layer Thickness at Selective Laser Melting. *Procedia Eng* **2017**, *174*, 126–134, doi:https://doi.org/10.1016/j.proeng.2017.01.179.

51. Coeck, S.; Bisht, M.; Plas, J.; Verbist, F. Prediction of Lack of Fusion Porosity in Selective Laser Melting Based on Melt Pool Monitoring Data. *Addit Manuf* **2019**, *25*, 347–356, doi:https://doi.org/10.1016/j.addma.2018.11.015.

52. Li, R.; Liu, J.; Shi, Y.; Wang, L.; Jiang, W. Balling Behavior of Stainless Steel and Nickel Powder during Selective Laser Melting Process. *The International Journal of Advanced Manufacturing Technology* **2012**, *59*, 1025–1035, doi:10.1007/s00170-011-3566-1.

53. Jia, H.; Sun, H.; Wang, H.; Wu, Y.; Wang, H. Scanning Strategy in Selective Laser Melting (SLM): A Review., doi:10.1007/s00170-021-06810-3/Published.

54. Irrinki, H.; Dexter, M.; Barmore, B.; Enneti, R.; Pasebani, S.; Badwe, S.; Stitzel, J.; Malhotra, R.; Atre, S. Effects of Powder Attributes and Laser Powder Bed Fusion (L-PBF) Process Conditions on the Densification and Mechanical Properties of 17-4 PH Stainless Steel. *JOM* **2016**, *68*, 860–868, doi:https://doi.org/10.1007/s11837-015-1770-4.

55. Spierings, A.B.; Herres, N.; Levy, G. Influence of the Particle Size Distribution on Surface Quality and Mechanical Properties in AM Steel Parts. *Rapid Prototyp J* **2011**, *17*, 195–202, doi:10.1108/13552541111124770.

56. Nguyen, Q.B.; Nai, M.L.S.; Zhu, Z.; Sun, C.-N.; Wei, J.; Zhou, W. Characteristics of Inconel Powders for Powder-Bed Additive Manufacturing. *Engineering* **2017**, *3*, 695–700, doi:https://doi.org/10.1016/J.ENG.2017.05.012.

57.  Attar, H.; Prashanth, K.G.; Zhang, L.-C.; Calin, M.; Okulov, I. V; Scudino, S.; Yang, C.; Eckert, J. Effect of Powder Particle Shape on the Properties of In Situ Ti–TiB Composite Materials Produced by Selective Laser Melting. *J Mater Sci Technol* **2015**, *31*, 1001–1005, doi:https://doi.org/10.1016/j.jmst.2015.08.007.

58.  Tanrikulu, A. Microstructure and Mechanical Properties of Additive Manufacturing Titanium Alloys After Thermal Processing, Portland State University: Portland, OR, 2017.

59.  Donachie Jr., M.J.; Donachie, M.J. *Titanium : A Technical Guide*; A S M International: Materials Park, UNITED STATES, 2000; ISBN 9781615030620.

60.  Boyer, R.R.; Briggs, R.D. The Use of β Titanium Alloys in the Aerospace Industry. *J Mater Eng Perform* **2005**, *14*, 681–685, doi:10.1361/105994905X75448.

61.  Liu, S.; Shin, Y.C. Additive Manufacturing of Ti6Al4V Alloy: A Review. *Mater Des* **2019**, *164*, 107552, doi:10.1016/j.matdes.2018.107552.

62.  Gerd Lütjering, J.C.W. *Titanium*; Engineering Materials, Processes; Springer Berlin Heidelberg: Berlin, Heidelberg, 2007; ISBN 978-3-540-71397-5.

63.  Liu, J.; Sun, Q.; Zhou, C.; Wang, X.; Li, H.; Guo, K.; Sun, J. Achieving Ti6Al4V Alloys with Both High Strength and Ductility via Selective Laser Melting. *Materials Science and Engineering A* **2019**, *766*, doi:10.1016/j.msea.2019.138319.

64.  Xu, Y.; Zhang, D.; Guo, Y.; Hu, S.; Wu, X.; Jiang, Y. Microstructural Tailoring of As-Selective Laser Melted Ti6Al4V Alloy for High Mechanical Properties. *J Alloys Compd* **2020**, *816*, 152536, doi:10.1016/j.jallcom.2019.152536.

65.  Yan, X.; Yin, S.; Chen, C.; Huang, C.; Bolot, R.; Lupoi, R.; Kuang, M.; Ma, W.; Coddet, C.; Liao, H.; et al. Effect of Heat Treatment on the Phase Transformation and Mechanical Properties of Ti6Al4V Fabricated by Selective Laser Melting. *J Alloys Compd* **2018**, *764*, 1056–1071, doi:10.1016/j.jallcom.2018.06.076.

66.  Dai, N.; Zhang, L.C.; Zhang, J.; Zhang, X.; Ni, Q.; Chen, Y.; Wu, M.; Yang, C. Distinction in Corrosion Resistance of Selective Laser Melted Ti-6Al-4V Alloy on Different Planes. *Corros Sci* **2016**, *111*, 703–710, doi:10.1016/j.corsci.2016.06.009.

67.  Cao, F.; Zhang, T.; Ryder, M.A.; Lados, D.A. A Review of the Fatigue Properties of Additively Manufactured Ti-6Al-4V. *Jom* **2018**, *70*, 349–357, doi:10.1007/s11837-017-2728-5.

68.  Xu, W.; Sun, S.; Elambasseril, J.; Liu, Q.; Brandt, M.; Qian, M. Ti-6Al-4V Additively Manufactured by Selective Laser Melting with Superior Mechanical Properties. *Jom* **2015**, *67*, 668–673, doi:10.1007/s11837-015-1297-8.

69.  Sun, C.; Chi, W.; Wang, W.; Duan, Y. Characteristic and Mechanism of Crack Initiation and Early Growth of an Additively Manufactured Ti-6Al-4V in Very High Cycle Fatigue Regime. *Int J Mech Sci* **2021**, *205*, doi:10.1016/j.ijmecsci.2021.106591.

70.  Du, L.; Pan, X.; Qian, G.; Zheng, L.; Hong, Y. Crack Initiation Mechanisms under Two Stress Ratios up to Very-High-Cycle Fatigue Regime for a Selective Laser Melted Ti-6Al-4V. *Int J Fatigue* **2021**, *149*, 106294, doi:10.1016/j.ijfatigue.2021.106294.

71.  Walker, K.F.; Liu, Q.; Brandt, M. Evaluation of Fatigue Crack Propagation Behaviour in Ti-6Al-4V Manufactured by Selective Laser Melting. *Int J Fatigue* **2017**, *104*, 302–308, doi:10.1016/j.ijfatigue.2017.07.014.

72.  Syed, A.K.; Ahmad, B.; Guo, H.; Machry, T.; Eatock, D.; Meyer, J.; Fitzpatrick, M.E.; Zhang, X. An Experimental Study of Residual Stress and Direction-Dependence of Fatigue Crack Growth Behaviour in as-Built and Stress-Relieved Selective-Laser-Melted Ti6Al4V. *Materials Science and Engineering A* **2019**, *755*, 246–257, doi:10.1016/j.msea.2019.04.023.

73.  Jesus, J.S.; Borrego, L.P.; Ferreira, J.A.M.; Costa, J.D.; Capela, C. Fatigue Crack Growth Behaviour in Ti6Al4V Alloy Specimens Produced by Selective Laser Melting. *Int J Fract* **2020**, *223*, 123–133, doi:10.1007/s10704-019-00417-2.

74.  *EOS Titanium Ti64 Grade 5 Material Data Sheet Metal Solutions*;

75.  Bieler, T.R.; Trevino, R.M.; Zeng, L. Alloys: Titanium. In *Encyclopedia of Condensed Matter Physics*; Elsevier, 2005; pp. 65–76.

76. Elmer, J.W.; Palmer, T.A.; Babu, S.S.; Specht, E.D. In Situ Observations of Lattice Expansion and Transformation Rates of α and β Phases in Ti–6Al–4V. *Materials Science and Engineering: A* **2005**, *391*, 104–113, doi:10.1016/j.msea.2004.08.084.

77. Motyka, M. Martensite Formation and Decomposition during Traditional and AM Processing of Two-Phase Titanium Alloys—An Overview. *Metals (Basel)* **2021**, *11*, 481, doi:10.3390/met11030481.

78. Barriobero-Vila, P.; Gussone, J.; Haubrich, J.; Sandlöbes, S.; Da Silva, J.; Cloetens, P.; Schell, N.; Requena, G. Inducing Stable α + β Microstructures during Selective Laser Melting of Ti-6Al-4V Using Intensified Intrinsic Heat Treatments. *Materials* **2017**, *10*, 268, doi:10.3390/ma10030268.

79. Burgers, W.G. On the Process of Transition of the Cubic-Body-Centered Modification into the Hexagonal-Close-Packed Modification of Zirconium. *Physica* **1934**, *1*, 561–586, doi:10.1016/S0031-8914(34)80244-3.

80. Karthikeyan, T.; Saroja, S.; Vijayalakshmi, M. Evaluation of Misorientation Angle-Axis Set between Variants during Transformation of Bcc to Hcp Phase Obeying Burgers Orientation Relation. *Scr Mater* **2006**, *55*, 771–774, doi:10.1016/j.scriptamat.2006.07.022.

81. Becker, T. Selective Laser Melting Produced Ti-6Al-4V: Post-Process Heat Treatments to Achieve Superior Tensile Properties. *Materials* **2018**, *11*, 146, doi:10.3390/ma11010146.

82. Yina Guo *Literature Review of Titanium Alloys and Linear Friction Welding*; 2016;

83. A. L. Pilchak *Materials Science and Engineering The Ohio State University* ; 2009;

84. Konečná, R.; Medvecká, D.; Nicoletto, G. Structure, Texture and Tensile Properties of Ti6Al4V Produced by Selective Laser Melting. *Production Engineering Archives* **2019**, *25*, 60–65, doi:10.30657/pea.2019.25.12.

85. Barriobero-Vila, P.; Artzt, K.; Stark, A.; Schell, N.; Siggel, M.; Gussone, J.; Kleinert, J.; Kitsche, W.; Requena, G.; Haubrich, J. Mapping the Geometry of Ti-6Al-4V: From Martensite Decomposition to Localized Spheroidization during Selective Laser Melting. *Scr Mater* **2020**, *182*, 48–52, doi:10.1016/j.scriptamat.2020.02.043.

86. Fan, Y.; Tian, W.; Guo, Y.; Sun, Z.; Xu, J. Relationships among the Microstructure, Mechanical Properties, and Fatigue Behavior in Thin Ti6Al4V. *Advances in Materials Science and Engineering* **2016**, *2016*, 7278267, doi:10.1155/2016/7278267.

87. Liu, S.; Shin, Y.C. Additive Manufacturing of Ti6Al4V Alloy: A Review. *Mater Des* **2019**, *164*, 107552, doi:https://doi.org/10.1016/j.matdes.2018.107552.

88. Tshephe, T.S.; Akinwamide, S.O.; Olevsky, E.; Olubambi, P.A. Additive Manufacturing of Titanium-Based Alloys- A Review of Methods, Properties, Challenges, and Prospects. *Heliyon* **2022**, *8*, e09041, doi:https://doi.org/10.1016/j.heliyon.2022.e09041.

89. Seabra, M.; Azevedo, J.; Araújo, A.; Reis, L.; Pinto, E.; Alves, N.; Santos, R.; Pedro Mortágua, J. Selective Laser Melting (SLM) and Topology Optimization for Lighter Aerospace Componentes. *Procedia Structural Integrity* **2016**, *1*, 289–296, doi:10.1016/j.prostr.2016.02.039.

90. Palmeri, D.; Buffa, G.; Pollara, G.; Fratini, L. The Effect of Building Direction on Microstructure and Microhardness during Selective Laser Melting of Ti6Al4V Titanium Alloy. *J Mater Eng Perform* **2021**, *30*, 8725–8734, doi:10.1007/s11665-021-06039-x.

91. Yadroitsev, I.; Krakhmalev, P.; Yadroitsava, I. Selective Laser Melting of Ti6Al4V Alloy for Biomedical Applications: Temperature Monitoring and Microstructural Evolution. *J Alloys Compd* **2014**, *583*, 404–409, doi:https://doi.org/10.1016/j.jallcom.2013.08.183.

92. Vrancken, B.; Thijs, L.; Kruth, J.-P.; Van Humbeeck, J. Heat Treatment of Ti6Al4V Produced by Selective Laser Melting: Microstructure and Mechanical Properties. *J Alloys Compd* **2012**, *541*, 177–185, doi:10.1016/j.jallcom.2012.07.022.

93. Itaka, K.; Ogasawara, T.; Boucetta, A.; Benioub, R.; Sumiya, M.; Hashimoto, T.; Koinuma, H.; Furuya, Y. Direct Carbothermic Silica Reduction from Purified Silica to Solar-Grade Silicon. *J Phys Conf Ser* **2015**, *596*, 012015, doi:10.1088/1742-6596/596/1/012015.

94. Chen, Y.; Liou, F.W.; Chen, Y.; Liou, F.W. *Additive Manufacturing of Metal Functionally Graded Materials: A Review*; 2018;

95.  Wang, S.; Liu, L.; Li, K.; Zhu, L.; Chen, J.; Hao, Y. Pore Functionally Graded Ti6Al4V Scaffolds for Bone Tissue Engineering Application. *Mater Des* **2019**, *168*, 107643, doi:https://doi.org/10.1016/j.matdes.2019.107643.

96.  Onal, E.; Frith, J.; Jurg, M.; Wu, X.; Molotnikov, A. Mechanical Properties and In Vitro Behavior of Additively Manufactured and Functionally Graded Ti6Al4V Porous Scaffolds. *Metals (Basel)* **2018**, *8*, 200, doi:10.3390/met8040200.

97.  Al-Saedi, D.S.J.; Masood, S.H.; Faizan-Ur-Rab, M.; Alomarah, A.; Ponnusamy, P. Mechanical Properties and Energy Absorption Capability of Functionally Graded F2BCC Lattice Fabricated by SLM. *Mater Des* **2018**, *144*, 32–44, doi:10.1016/j.matdes.2018.01.059.

98.  Wang, S.; Liu, L.; Li, K.; Zhu, L.; Chen, J.; Hao, Y. Pore Functionally Graded Ti6Al4V Scaffolds for Bone Tissue Engineering Application. *Mater Des* **2019**, *168*, 107643, doi:10.1016/j.matdes.2019.107643.

99.  Yasa, E.; Kruth, J.-P. Microstructural Investigation of Selective Laser Melting 316L Stainless Steel Parts Exposed to Laser Re-Melting. *Procedia Eng* **2011**, *19*, 389–395, doi:10.1016/j.proeng.2011.11.130.

100. Karimi, J.; Suryanarayana, C.; Okulov, I.; Prashanth, K.G. Selective Laser Melting of Ti6Al4V: Effect of Laser Re-Melting. *Materials Science and Engineering: A* **2021**, *805*, 140558, doi:10.1016/j.msea.2020.140558.

101. Bedmar, J.; de la Pezuela, J.; Riquelme, A.; Torres, B.; Rams, J. Impact of Remelting in the Microstructure and Corrosion Properties of the Ti6Al4V Fabricated by Selective Laser Melting. *Coatings* **2022**, *12*, 284, doi:10.3390/coatings12020284.

102. Shi, R.; Khairallah, S.; Heo, T.W.; Rolchigo, M.; McKeown, J.T.; Matthews, M.J. Integrated Simulation Framework for Additively Manufactured Ti-6Al-4V: Melt Pool Dynamics, Microstructure, Solid-State Phase Transformation, and Microelastic Response. *JOM* **2019**, *71*, 3640–3655, doi:10.1007/s11837-019-03618-1.

103. Kang, K.; Yuan, L.; Phillion, A.B. A 3D Simulation of Grain Structure Evolution during Laser Rescanning Process of Powder Bed Fusion Additive Manufacturing. *IOP Conf Ser Mater Sci Eng* **2023**, *1281*, 012009, doi:10.1088/1757-899X/1281/1/012009.

104. Coen, V.; Goossens, L.; Hooreweder, B. Van Methodology and Experimental Validation of Analytical Melt Pool Models for Laser Powder Bed Fusion. *J Mater Process Technol* **2022**, *304*, 117547, doi:10.1016/j.jmatprotec.2022.117547.

105. Karayagiz, K.; Elwany, A.; Tapia, G.; Franco, B.; Johnson, L.; Ma, J.; Karaman, I.; Arróyave, R. Numerical and Experimental Analysis of Heat Distribution in the Laser Powder Bed Fusion of Ti-6Al-4V. *IISE Trans* **2019**, *51*, 136–152, doi:10.1080/24725854.2018.1461964.

# 3. COMPREHENSIVE INSIGHT INTO MICROSTRUCTURE EVOLUTION DURING PREHEATING-ASSISTED LPBF AND ITS INFLUENCE ON MECHANICAL PROPERTIES OF Ti-6Al-4V

## 3.1. Introduction and Overview

LPBF has emerged as a promising alternative to conventional fabrication methods, which often result in significant material waste, increased costs, and environmental impacts [1]. Conventional methods encounter challenges with complex geometries, leading to the necessity of multiple production steps and increasing the defect risks, ultimately decreasing efficiency. On the contrary, LPBF offers near-net-shape fabrication that minimizes material usage, energy consumption, and the cost of assembly [2]. Furthermore, LPBF can handle a wide variety of materials for components with complex geometries, leading to an attractive alternative across various industries [3].

LPBF stands out among the various AM techniques due to its high resolution: processing ability of extremely thin layer heights, which makes this process ideal for lightweight studies in engineering applications. Ti-6Al-4V is one of the most popular materials used in LPBF for weight reduction which boasts exceptional mechanical properties and versatility [3,4]. The high strength-to-weight ratio of this material makes it an essential choice for manufacturing lightweight components that require robust strength, such as aircraft parts, automotive components, and internal body implants [5]. In addition, Ti-6Al4V alloy's exceptional corrosion resistance is invaluable for the components that operate in harsh environments such as marine applications, chemical processing, oil and gas industry [3]. The remarkable fracture toughness of the material makes it also ideal for applications demanding fatigue resistance and durability, including defense and aerospace components [3].

Besides its remarkable properties, LPBF-fabricated Ti-6Al-4V presents inherent challenges due to the thermal nature of the process. Ti-6Al-4V is a bimodal $\alpha+\beta$ alloy with superior strength compared to $\alpha$-Ti alloys and a wider processing window than both $\alpha$-Ti and $\beta$-Ti alloys [6]. Instant temperature changes and rapid cooling rates associated with LPBF, reaching $10^4$ to $10^6$

K/s [7], can cause an unstable solidification before achieving full homogenization, leading to anisotropic microstructures that may compromise the final part's mechanical properties [8]. During the LPBF of Ti-6Al-4V, the β phase decomposes to an acicular α′ martensite phase during phase transformation while cooling down from laser processing [9]. The α′ martensite phase exhibits a highly anisotropic microstructure and increased hardness, which potentially leads to reduced ductility and toughness [9]. However, transforming the martensite α' phase into a more favorable bimodal α+β microstructure can significantly improve material ductility while alleviating the impact of residual stresses [10]. It is worth mentioning that the martensitic decomposition temperature for Ti-6Al-4V typically occurs within the range of 600 to 650 °C [11,12].

Recent studies have revealed that employing complementary thermal treatments can effectively stabilize the microstructure of LPBF-fabricated Ti-6Al-4V, leading to enhanced phase management, reduced residual stress, and improved mechanical properties while minimizing anisotropy [13–18]. Ali *et al.* [13] demonstrated the effectiveness of the powder bed preheating at elevated temperatures in transforming the α′ martensite phase into a more ductile and uniform α + β microstructure. This resulted in superior plastic behavior and microstructure stability. Their findings also confirmed that preheating the substrate to 370°C and 570°C reduced the residual stress by 71% and nearly 100%, respectively, compared to a substrate heated to 100°C. The other studies presented by Vrancken *et al.* [14] and Kruth *et al.* [15], have supported the results of the effectiveness of substrate preheating, indicating the potential to improve the properties of Ti-6Al-4V fabricated by LPBF. Additionally, researchers have explored promoting the non-equilibrium α′ martensite decomposition in the as-built microstructure to an equilibrium α+β microstructure through post-process heat treatment. Studies have demonstrated that annealing within the range of 750-900°C can facilitate α′ martensite decomposition and enhance ductility [16–18]. A recent

study in the static coarsening behavior of lamellar structures in LPBF-fabricated Ti-6Al-4V revealed that annealing at 900°C or higher temperatures significantly accelerates coarsening kinetics of the lamellar structure [19]. Moreover, it has been found that a slower cooling rate after solution treatment results in an α+β microstructure, while rapid cooling yields α′ martensitic microstructures [20]. Post-process thermal treatments have also been employed to achieve a stabilized α+β microstructure in Ti-6Al-4V fabricated by other AM techniques, such as wire arc additive manufacturing (WAAM) [21]. Some studies have investigated the impact of Hot Isostatic Pressing (HIP) and reported enhanced mechanical properties and phase transformation. Su *et al.* [22] explored that the HIP process resulted in a microstructure consisting of lamellar α and β phases without any texture formation and responded to enhanced mechanical properties. Meanwhile, Cai *et al.* [23] observed a remarkable improvement in ductility, despite a slight reduction in the material's strength value.

The final microstructure of LPBF-fabricated components can be significantly influenced by process parameters as well as thermal treatments, and these parameters attain careful consideration to generate the desired microstructure [3,4]. Several investigations have unveiled the influence of various factors, such as laser power, layer thickness, and scan speed on microstructure. For instance, Xu *et al.* [24] determined that slowing down the cooling rate during fabrication of Ti-6Al-4V enhanced the elongation by transforming the α′ martensite into α+β phases. They also noted that layer thickness played a crucial role in microstructure due to its effect on cooling rate and thermal cycles. As a result, the final few layers of each sample exhibited an α′ martensitic structure, due to the absence of subsequent thermal cycles. In a more recent study, Xu *et al.* [25] discovered that inter-layer time is another effective parameter for promoting decomposition. They observed a lamellar (α+β) structure with a 1 s inter-layer time, while a mixed structure was

generated when the inter-layer time was increased to 10 s. Moreover, the study reported that modifying layer thickness could yield different microstructures. With a 30 μm increase in layer thickness from 60 to 90 μm, a coarser lamellar (α+β) microstructure was obtained.

Numerous studies have discovered modifying the Ti-6Al-4V alloy's microstructure either through post-process heat treatments or by adjusting the laser parameters. However, no study has yet investigated in-situ layer-by-layer laser heat treatment. In this chapter, we utilized a low-energy heat input by the laser source to preheat the powder on each layer before processing it with a higher-energy melting laser scan. This innovative method empowered us to modify the as-fabricated microstructure of the part through in-situ thermal process controlled solidification and cooling rates, thereby eliminating the need for additional post-heat treatments. We thoroughly evaluated the effect of various preheating laser parameters on the microstructure and mechanical response of the final part, while adhering to the manufacturer's suggested parameter set for the melting laser scan. Our findings demonstrate that a specific set of preheating parameters can notably improve the mechanical properties of the final product, fostering a more stable phase transformation response encompassing the combination of β, α′ martensite, and α phases.

The focus of this chapter is to study how the new concept of layerwise preheating could influence the evolution of microstructure and mechanical properties during the LPBF process (Figure 3.1). This process, namely the preheating-assisted LPBF process, could be a substitute solution for conventional LPBF processes.
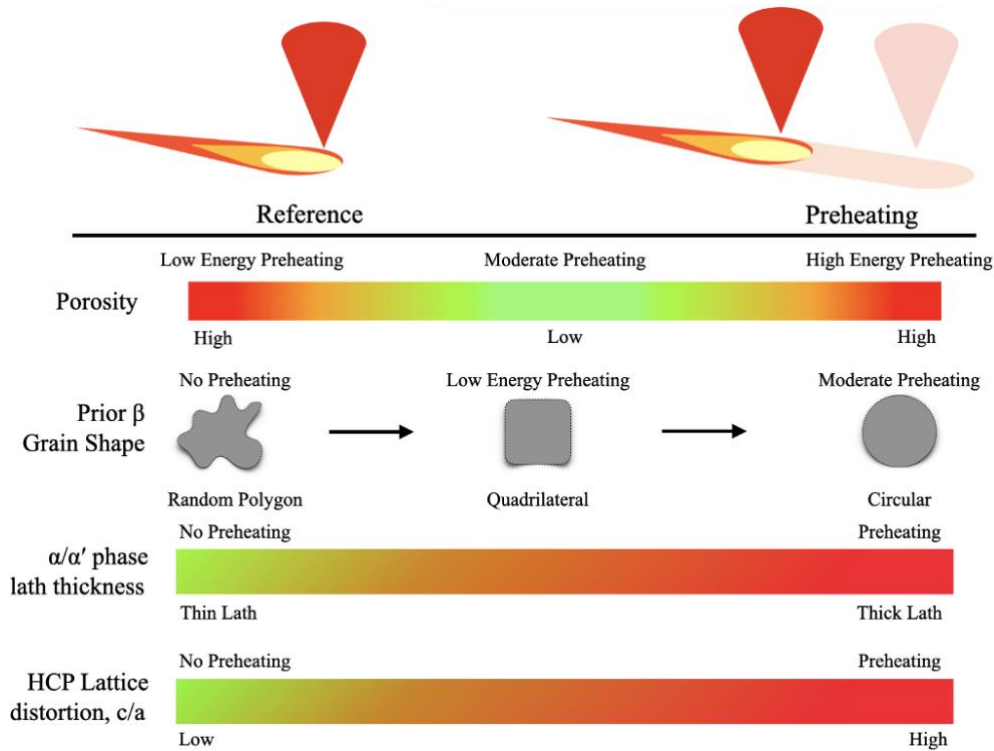
*Figure 3.1. A schematic representation of how the concept of preheating could tailor the microstructure of Ti6Al4V during an SLM process.*

3.2. Experimental Methods and Fabrication

3.2.1. Materials and Fabrication

Gas-atomized Ti-6Al-4V Grade 5 powder, supplied by EOS North America (Pflugerville, TX, USA), was used for the fabrication. The chemical composition of the powder (wt.%) consisted of 5.50 - 6.75 Al, 3.50 - 4.50 V, 0.20 O, 0.05 N, 0.08 C, 0.015 H, 0.30 Fe, and balance Ti, satisfying the specifications outlined in ISO 5832-3, ASTM F1472, ASTM F2924, and ASTM F3302 standards. The size distribution of the powder exhibited a range from 20 μm to 80 μm [26].

SolidWorks software (Dassault Systems, Vélizy-Villacoublay, France), utilized for designing the digital files for microstructure samples (20 mm × 6 mm × 6 mm) and dog-bone tensile test coupons.

The coupons were fabricated using LPBF technology with an EOS M290 SLM printer (EOS GmbH, Electro Optical Systems, Krailling, Germany) with a capacity of 400 W Ytterbium fiber laser. Before the building process, the building plate was preheated to 80 °C to prevent the delamination of the initial layers caused by high thermal gradients.

To quantize the heat input in the layerwise preheating scanning strategy and optimize the process parameters, preheating energy density was calculated using Eq. (1), where $E_v$ is the energy density, $P$ is the laser power (W), $v$ is the laser scanning speed (mm/s), $t$ is the layer thickness (mm), and $h$ is the hatch spacing (mm) [27].

$$E_v = \frac{P}{v.h.t} \qquad (1)$$

In this investigation, a novel approach using layerwise preheating and melting scans was implemented to explore the material properties of the fabricated samples. A reference sample (non-preheated) was fabricated only with the melting laser scan. The laser process parameters for the melting scan, as suggested by the manufacturer, had a laser power of 280 W, scan speed of 1300 mm/s, hatch spacing of 120 μm, and layer thickness of 40 μm, resulting in an energy density of 44.87 J/mm³. Other scanning parameters consisted of a Gaussian-distributed laser spot size of 100 μm, a stripe scanning strategy, and a hatch angle of 67°. For the preheating process, a layerwise preheating laser scan was conducted before the melting laser scan in each layer. The preheating scan encompassed a range of scanning speeds, varying from 650 mm/s to 1950 mm/s, and corresponding laser powers spanning from 140 W to 252 W, all while maintaining a consistent hatch spacing of 120 μm. The preheating scanning parameters investigated in this chapter for each sample are provided in Table 2. All specimens were carefully cut out from the building plate using a wire Electrical Discharge Machining (EDM) cutter (EDM Network, Inc., Sugar Grove, IL, USA).

*Table 3.1 Laser exposure process parameters of layerwise preheating scan.*

| Sample # | Laser Power ($P$, W) | Scan Speed ($v$, mm/s) | Energy Density ($E$, J/mm$^3$) |
|----------|----------------------|------------------------|--------------------------------|
| 1 | 140 | 1950 | 14.96 |
| 2 | 140 | 1625 | 17.95 |
| 3 | 140 | 1300 | 22.44 |
| 4 | 140 | 650 | 44.87 |
| 5 | 196 | 1950 | 20.94 |
| 6 | 196 | 1625 | 25.13 |
| 7 | 196 | 1300 | 31.41 |
| 8 | 196 | 650 | 62.82 |
| 9 | 252 | 1950 | 26.92 |
| 10 | 252 | 1625 | 32.31 |
| 11 | 252 | 1300 | 40.38 |
| 12 | 252 | 650 | 80.77 |
| Reference | 280 | 1300 | 44.87 |

3.2.2. Experimental Methods

3.2.2.1. Microstructure Characterization

A Hitachi S – 3000 N Variable Pressure Scanning Electron Microscopy (SEM) was used to examine the porosity, α-phase lath thickness, and grain morphology resulting from various preheating parameters applied during the fabrication process. Before surface preparation for microstructural characterization, samples were cut using a TECHCUT 5TM precision low-speed cutter (Allied High-Tech Products, Inc., Rancho Dominguez, CA, USA). The metallography process began with cold-mounting and samples were prepared by grinding through a range of grit sizes from 320 to 1200. A DiaMat polishing cloth was utilized for the initial polishing with a 1 μm diamond suspension, followed by a final polish with a 0.04 μm colloidal silica suspension on a Red Final C polishing pad to ensure scratch-free, mirror-like sample surfaces. Subsequently, samples were rinsed with micro-organic soap and cleaned using isopropyl alcohol. Surface

preparation followed by etching with Kroll's reagent (1–3 mL HF, 2–6 mL $HNO_3$, 100 mL water) to reveal grain boundaries and phases.

A Bruker D8 Advance X-ray diffractometer (Bruker Corporation, Madison, WI, USA) was used for the compositional analysis of the fabricated samples, employing a Cu K-alpha wavelength of 1.5406 Å, a current of 40 mA, and a voltage of 40 kV at room temperature. Measurements were conducted at step intervals of 0.03° and a scan speed of 1/step, with 2θ ranging from 20° to 80°. X-ray diffraction (XRD) analyses were carried out to identify the existing phases and the grain texture of each sample's microstructure. Furthermore, the XRD data underwent additional examination using the Williamson-Hall method to estimate the microstrain value of the resulting structure [28].

Microscopy images were processed by using ImageJ [29], an image analysis software to assess the porosity level of each microstructure. The porosity percentage was evaluated by examining at least three different regions at two magnification levels (500x and 800x). ImageJ software was also employed to measure the lath thickness of the α-phase. Microstructure images were first converted to RGB stack-type grayscale images before adjusting the image to the auto contrast level. Next thresholding was then applied to achieve a sharp contrast between alpha laths. Particles with the size of 0.2 μm to 2.0 μm were detected, and the total particle counts for each size were calculated to determine the mean value. This process was carried out on a minimum of six different images to derive the average value for each microstructure image.

3.2.2.2. Mechanical Testing

Mechanical tests were carried out using a Shimadzu EHF E-Series (100 kN) testing machine equipped with a 4830 Servo Controller (Shimadzu Scientific Instruments, Inc., Missouri City, TX, USA). For precise strain measurements in the gauge section a digital image correlation

(DIC) system (Correlated Solutions, Inc., Irmo, SC, USA) was employed. Surface displacements and strain were analyzed by tracking light intensity patterns of high-contrast speckles on the coupon surface. Local strains were measured at the fracture site, as well as the global strain of the coupon. A CCD camera featuring 2.3 Mega Pixels each, Grasshopper GS3-U3-23S6M (FLIR Systems, Inc., Santa Barbra, CA, USA) with a pixel array of 1920 x 1200, was employed for image capturing. Image processing and correlation were performed using VIC-3D® software (Correlated Solutions, Inc., Irmo, SC, USA). All samples were tested at a constant loading rate of 1.2 mm/min, adhering to the recommended testing standard for LPBF-fabricated Ti-6Al-4V tensile samples found in the literature [30].

3.3. Results

3.3.1. Microstructure Defects and Grain Structure

Porosity levels in each specimen were assessed through the examination of SEM micrographs, which were captured from at least three distinct regions with magnifications set at 500x and 800x. The SEM analysis highlighted a notable reduction in both the size of imperfections and the extent of porosity in samples exhibiting energy density values within the range of 25.12 J/mm³ to 40.38 J/mm³. Figure 3.2a presents the microstructure image of the reference sample, while Figure 3.2b displays the microstructure image of a representative sample. The images demonstrate a significant reduction in porosity defects for this particular representative sample, highlighting the effectiveness of layerwise preheating in enhancing material properties.
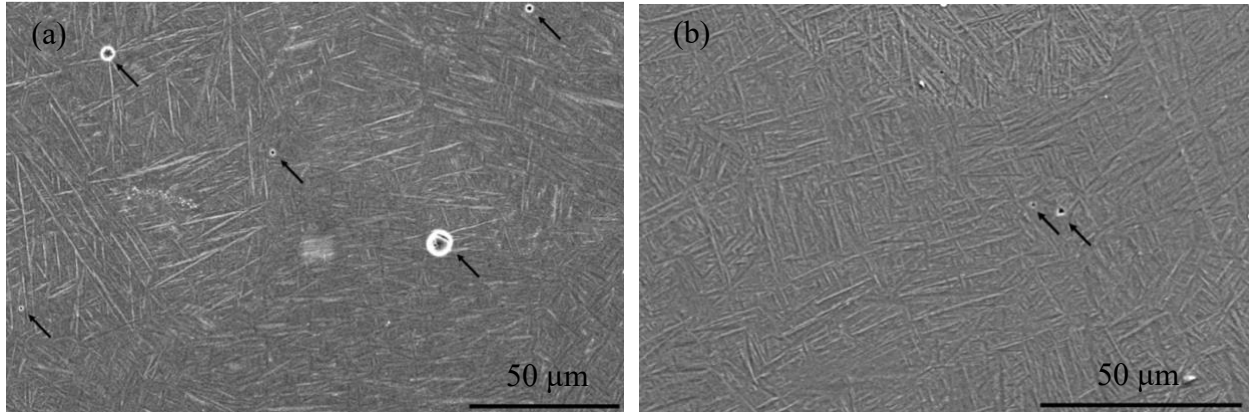
*Figure 3.2. SEM images comparing porosity defects in (a) the reference sample (no preheating) and (b) a representative sample, which underwent layerwise preheating with an energy density level of 40.38 J/mm³ E = 40.38 J/mm³ (252 W, 1300 mm/s).*

Figure 3.3 demonstrates the impact of layerwise preheating and scanning speed on the porosity of Ti-6Al-4V microstructures fabricated via LPBF. Within this range of energy density, there is a noticeable reduction in porosity, highlighting the effectiveness of layerwise preheating in improving sample quality. The reference sample, which did not undergo preheating, had an average porosity of $0.47\% \pm 0.015$. The introduction of additional preheating scans notably affected porosity levels in certain instances, particularly when energy density values ranged from 25.12 J/mm³ to 40.38 J/mm³. Samples processed with a laser power of 252 relatively showed improved surface quality and lower porosity, thus warranting further attention. In these samples, as the energy density increased from 975 mm/s to 1950 mm/s, the porosity level decreased significantly from 1.53% to 0.01%. In summary, higher preheating scan speeds contributed to a notable decrease in porosity and enhancement in density. These representative samples were subsequently chosen for more comprehensive examination within this study.
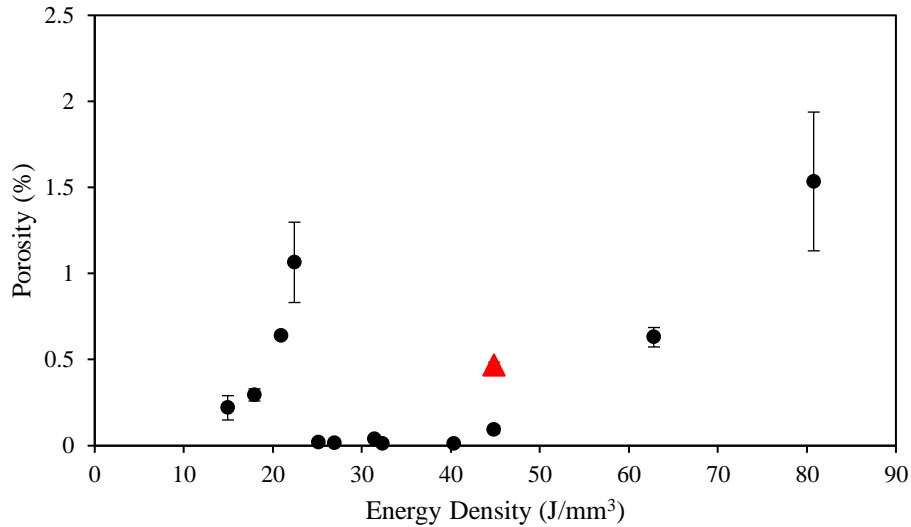
*Figure 0.3*

*Figure 3.3. The impact of layerwise preheating on porosity levels in samples using varying energy density values (25.12 to 40.38 J/mm³). The reference sample (no preheating) is denoted in red, providing a baseline for comparison.*

Moreover, Figure 3.4 presents a three-dimensional optical microscopy perspective of the prior β grains in the representative samples. These images highlight the impact of layerwise preheating and energy density on grain morphology in Ti-6Al-4V samples. Different prior β grain shapes were observed which were influenced by preheating scans and thermal processing conditions. In the reference sample with no preheating, prior β grain boundaries on the XY plane demonstrated a random polygonal geometry (Figure 3.4a). It was observed that with the addition of the layerwise preheating scan with the lowest energy density, the shape of the prior β grains transformed to a square shape on the XY plane (Figure 3.4b). When higher preheating energy was applied (32.31 J/mm³ with a preheating scan speed of 1625 mm/s) circular prior β grain regions formed on the XY plane (Figure 3.4c). across all samples, the specific orientation of laths at an angle of approximately 45° with respect to the Z-axis was observed.
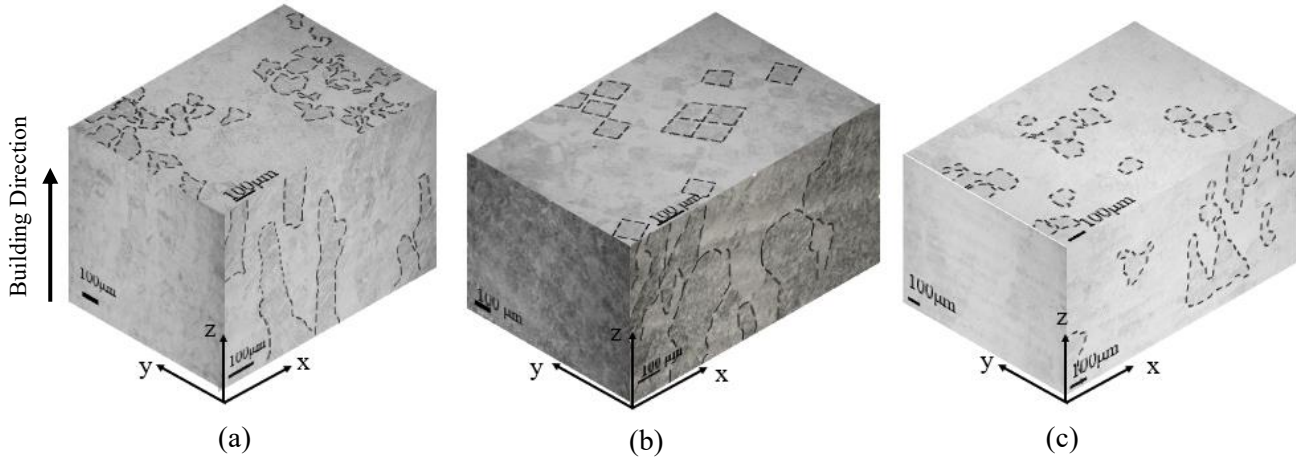
*Figure 3.4. Optical microscopy images showcasing the differences in prior β-grain boundary and grain morphology among distinct LPBF-produced Ti-6Al-4V samples: (a) reference sample (no preheating) featuring irregular polygonal grain boundaries; (b) layerwise preheated sample with an energy density of 26.92 J/mm³ (P=252 W, v=1950 mm/s), exhibiting square-like grain boundaries; (c) layerwise preheated sample with an energy density of 32.31 J/mm³ (P=252 W, v=1625 mm/s), characterized by irregular polygonal grain boundaries.*

The evaluation of α/α' phase lath thickness in both XY and ZX planes was conducted for the reference sample (non-preheated) and layerwise preheated samples. The analysis was performed using image processing techniques in SEM images via ImageJ, as shown in Figure 3.5. In the reference (non-preheated) sample, the thickness of α/α' laths on the XY plane was measured to be $0.797 \pm 0.005$, while on the ZX plane, it was $0.876 \pm 0.013$, as illustrated in Figure 3.5 using a red marker. This 10% difference in α lath thickness suggests an inconsistency in the microstructure between the XY and ZX planes, a finding that has been reported in the literature for the as-built condition of LPBF-fabricated Ti-6Al-4V.

In contrast, layerwise preheated samples had a more uniform distribution of α lath thickness between the XY and ZX planes. Additionally, the layerwise preheating process led to an increased in the average lath thickness in both XY and ZX planes. Specifically, the sample with a preheating energy density of 26.92 J/mm$^3$ (P=252 W, v=1950 mm/s) demonstrated a minimal difference of 0.04 μm between the α/α' lath thickness in the XY and ZX planes, equivalent to a 4.7% difference. The thickness variation for the sample with an energy density of 40.38 J/mm$^3$ (P=252 W, v=1300 mm/s) was 5.1%. However, in the application of the sample with an energy density of 32.31 J/mm$^3$ (P=252 W, v=1625 mm/s), a slight increase in thickness variation was noted at 10.5%. These findings highlight the notable impact of scanning speed

38

on the thickness of α/α′ phase laths. These results emphasize the influence of layerwise preheating on the microstructure and the distribution of α/ α′ phases lath thickness in LBPF fabricated Ti-6Al-4V microstructure.
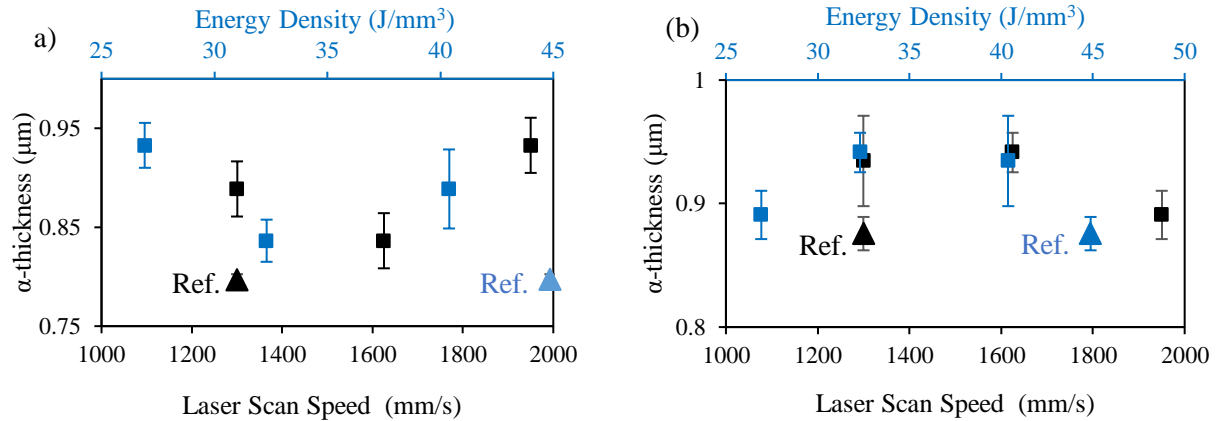


*Figure 3.5. The effect of layerwise preheating with varying energy density levels, ranging from 26.92 J/mm³ to 40.38 J/mm³, achieved by changing the scanning speed while keeping the laser power constant, on the α/α′ phases lath thickness in (a) XY Plane and (b) ZX Plane. The reference sample (no preheating) is represented by the triangle mark. Blue and black triangle markers represent the energy density and laser scan speed of the default laser parameters, respectively.*

Additional investigation into the probability distribution of α/α′ phases lath thickness for the four selected specimens with minimal porosity levels (<0.015%) is presented in  Figure 3.6. In contrast to the reference sample, all preheated samples demonstrated a coarser lath distribution. While the reference sample displayed the highest α/α′ phases lath thickness probability at 0.5 μm, the preheated specimens exhibited their highest probability at around 0.6 μm lath thickness.
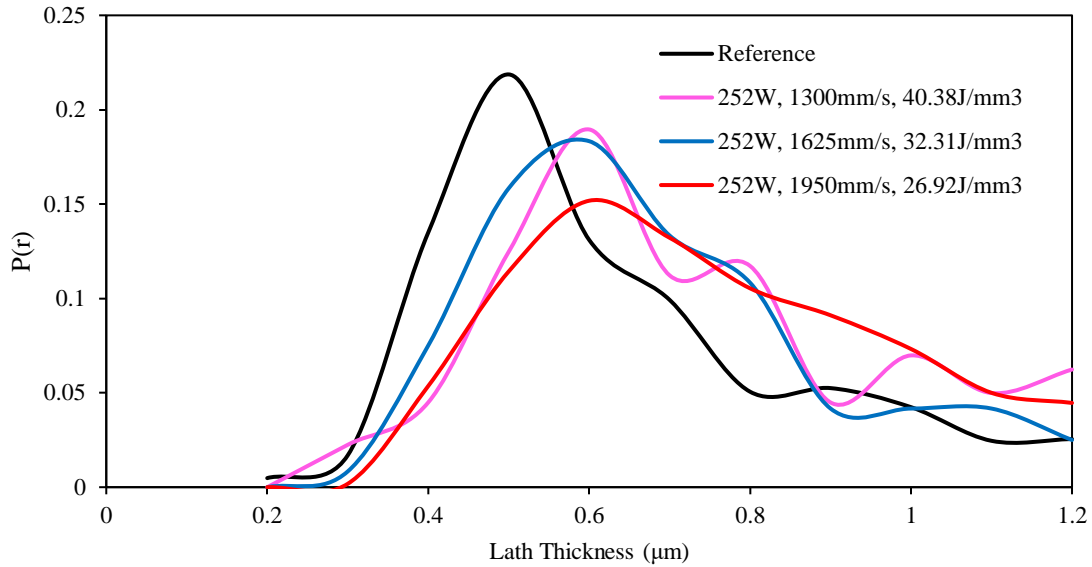
*Figure 3.6. The effect of layerwise preheating with different energy levels on the distribution of α/α' phases lath thickness. While the reference sample displayed the highest α/α' phases lath thickness probability at 0.5 μm, the preheated specimens exhibited their highest probability around 0.6 μm lath thickness.*

3.3.2. Lattice Transformation, and Phase Decomposition in Preheated LPBF Ti-6Al-4V

3.3.2.1. Crystallography through XRD Analysis

Figure 3.7 displays the XRD profiles of the reference and representative preheated specimens, organized in increasing order of applied preheating energy density levels. The most intense Bragg's peak for the reference sample was observed at the (101) plane on the XY surface (Figure 3.7). Conversely, the preheated samples demonstrated their strongest peak intensity at the (002) plane, indicating that a predominant orientation of the grains along this direction in the XY plane, which aligns with prior research [31]. Despite the preheated samples showing similar peak patterns, it's noteworthy that the reference sample exhibited its strongest peak intensity at the (101) plane on the XY surface. Additionally, an assessment was conducted on the peak intensity and broadening at the (002) plane for each of the preheated application. It's important to emphasize that peak broadening serves as an indicator of lattice strain development [32].
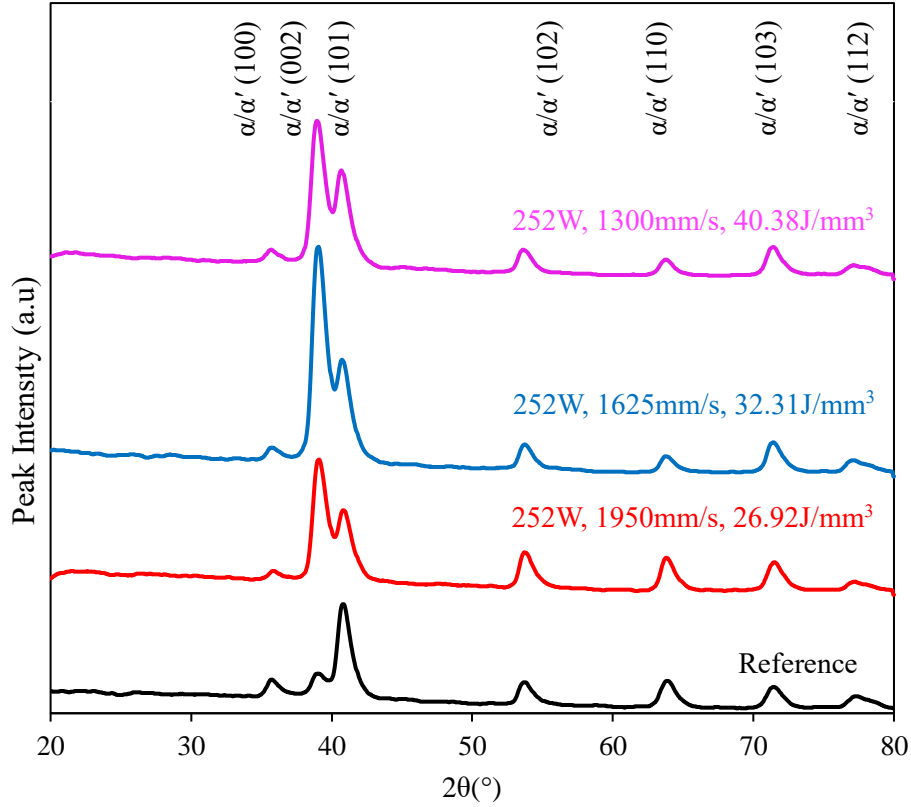
*Figure 3.7.  XRD patterns of the reference and preheated specimens as a function of preheating energy density in the XY Plane, illustrating the effect of preheating scan on changing the orientation of lath from (101) in the reference sample to (002) direction.*

The microstrain values of the microstructures were determiner using the Williamson-Hall (W-H) model, as illustrated in Figure 3.8. When the W-H Equation ($\beta \cos\theta = \frac{\lambda K}{D} + 4\varepsilon \sin\theta$) is considered as a linear equation in the form of y = mx + c, the slope of the equation corresponds to the strain value. A positive slope was observed for the reference sample. However, the addition of preheating scans to the powder resulted in the slope transitioning to a negative value, indicating a shift in the microstrain mode from tensile to compression. This transformation was more prominent at higher preheating scan speeds (1950 and 1625 mm/s), as depicted in Figure 3.8 (a) and (b). Conversely, at a lower preheating scan speed (1300 mm/s), the slope transformation was relatively minor, as shown in Figure 3.8 (d). This suggests that the introduction of preheating scans led to a transformation in the microstrain mode from tensile to compressive.
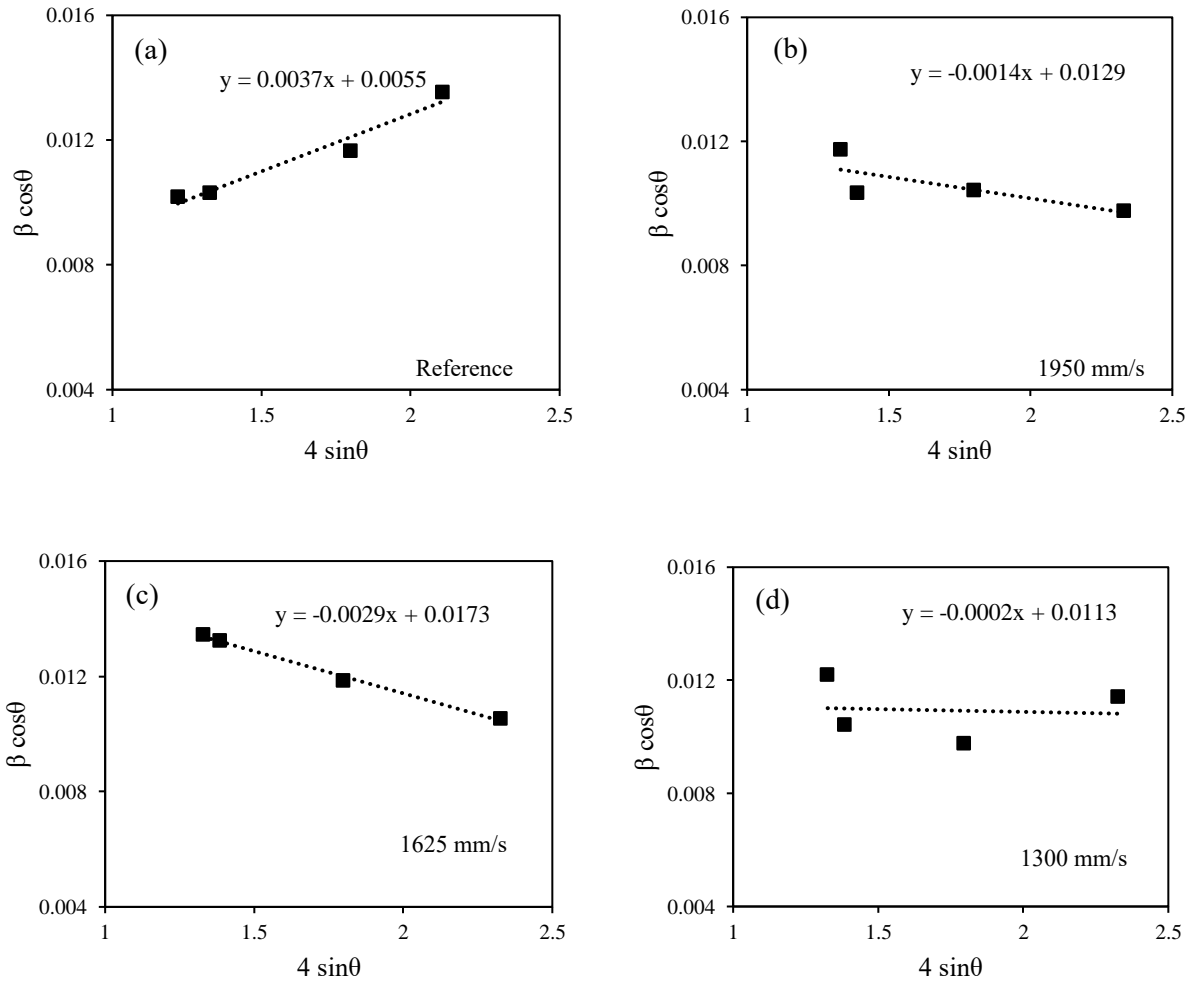
*Figure 3.8. Representation of microstrain values, derived from the slope of the fitted linear trendline in the W-H analysis, under varying preheating conditions. (a) The default Ti-6Al-4V sample without any preheating laser scan. Preheated samples at different energy densities include (b) E = 26.92 J/mm³ (P = 252 W, v = 1950 mm/s), (c) E = 32.31 J/mm³ (P = 252 W, v = 1625 mm/s), and (d) E = 40.38 J/mm³ (P = 252 W, v = 1300 mm/s).*

3.3.2.2. HCP Lattice Modification

The XRD analysis showed that the dominant phase of the primary microstructure is the hexagonal close pack (HCP) phase. This could correspond to either the α or α′ phase. The lattice parameters (a and c) were calculated using the method proposed by Klug *et al.* [33]. For the reference sample, these parameters were calculated as, a = 2.93 Å and c = 4.66 Å, consistent with previous studies [31,34]. The impact of layerwise preheating laser scans on the lattice parameter ratio (c/a) is illustrated in Figure 3.9a. The data reveal that the samples subjected to layerwise preheating exhibit a higher c/a ratio compared to the reference

sample. This signifies a greater degree of lattice distortion along the c-axis compared to the a-axis. Figure 3.9b demonstrates the reduction in the volume of the HCP lattice with the decrease in preheating energy density, by the increase of preheating laser scan speed. Figure 3.10 provides visual representations of HCP lattice distortion, displaying discrete α' decomposition for both the reference sample (with lower substitutional atoms) and the preheated sample (higher substitutional and interstitial atoms).
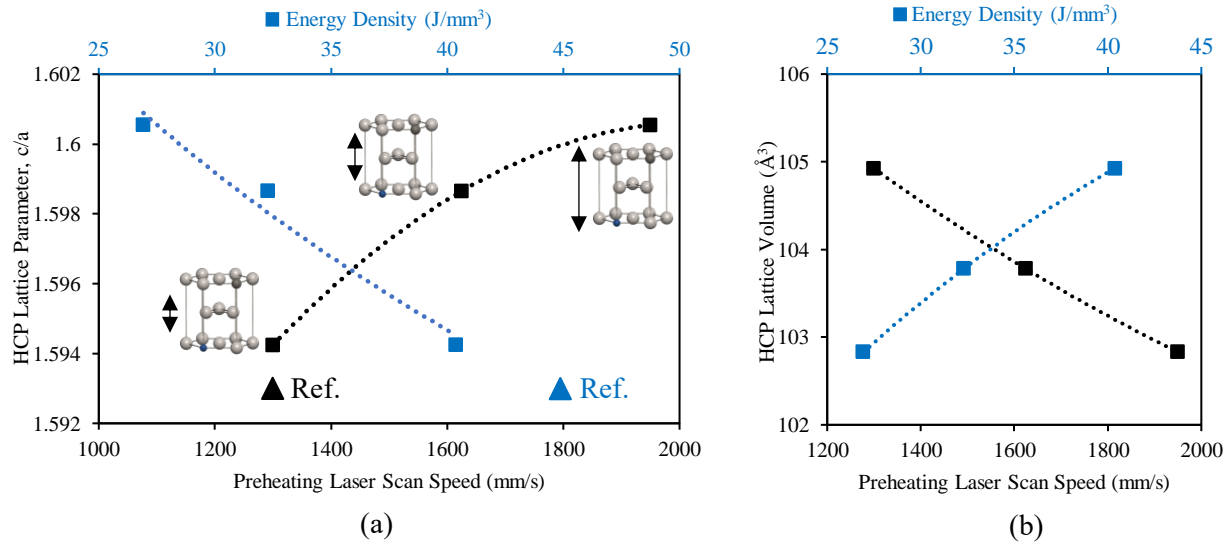


*Figure 3.9. (a) Deformation of the HCP lattice under varying preheating laser scan speeds, illustrating the impact on the lattice structure. (b) Variations in the volume of the HCP lattice at different preheating laser scan speeds, demonstrating the effects of solute atom diffusion on the lattice's dimensional properties. Blue and black triangle markers represent the energy density and laser scan speed of the default laser parameters respectively.*

Lower Preheating Laser Scan Speed: Large HCP

lattice with low solute amount of atom

Increasing Preheating Laser

Scan Speed

Super saturated with

substitutional V & Al and
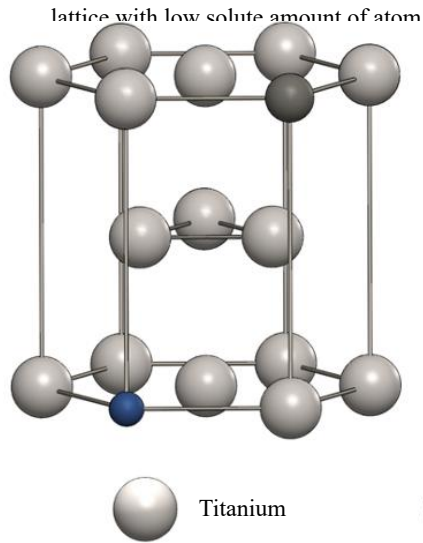
Higher Preheating Laser Scan Speed: Small HCP

lattice with high solute amount of atom

| Titanium | Vanadium | Aluminum | Oxygen |
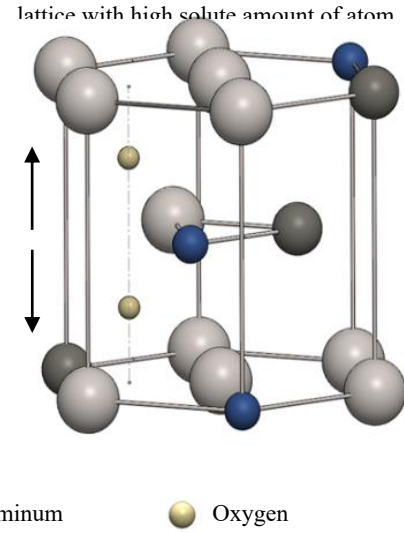
*Figure 3.10. Variation of solute atom concentration within the Ti-6Al-4V HCP lattice structure as a function of decreasing preheating energy density (increasing the preheating laser scan speed).*

3.3.2.3. Phase Transformation and Stable Phases at Room Temperature

The influence of preheating on the α′ phase decomposition was assessed by quantifying the β-phase content within the microstructure at each preheating energy density. A significant finding from this analysis is that all preheated samples, chosen for mechanical testing, exhibited a reduced proportion of the β-phase compared to that in the reference microstructure, as shown in Figure 3.11. The β phase in the preheated sample' microstructures dropped to a level of 0.01%. It is evident that all preheated samples, chosen for mechanical testing, demonstrated a lower percentage of the β-phase compared to the reference microstructure.
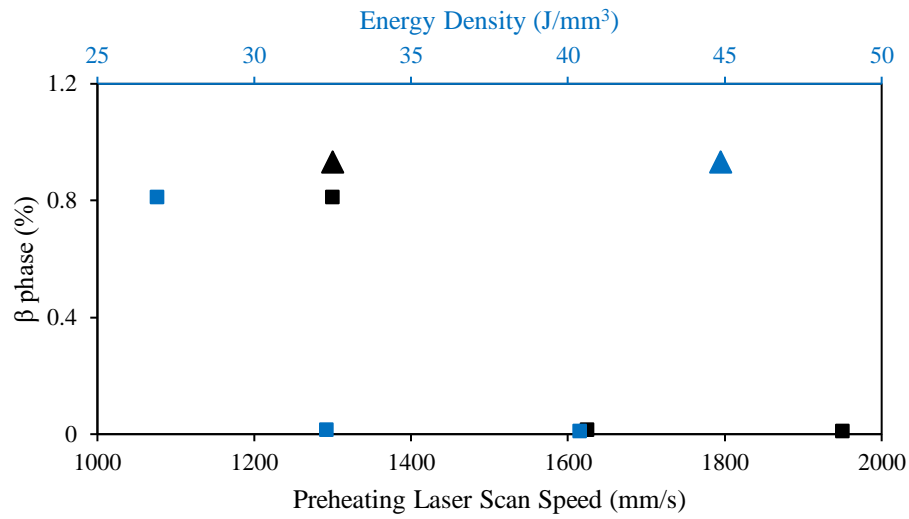
*Figure 3.11. Percentage of β-phase content in the microstructure as a function of different preheating laser scan speeds. Blue and black triangle markers represent the energy density and laser scan speed of the default laser parameters respectively.*

Figure 3.12 shows the decomposition of α′ into α + β phases in the reference sample (no preheating). Very fine β phase particles can be observed as bright speckles within the α-laths. They appear as broader Widmanstätten laths and the growth of α′ martensitic plates is noticeable between these wider laths, as evident from the microstructural image.



(a)

(b)
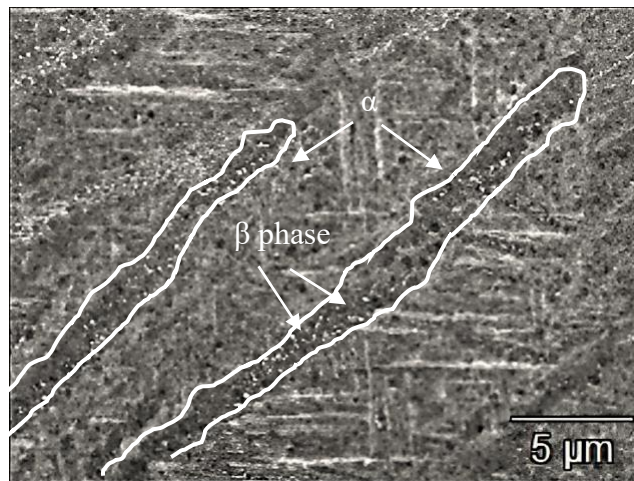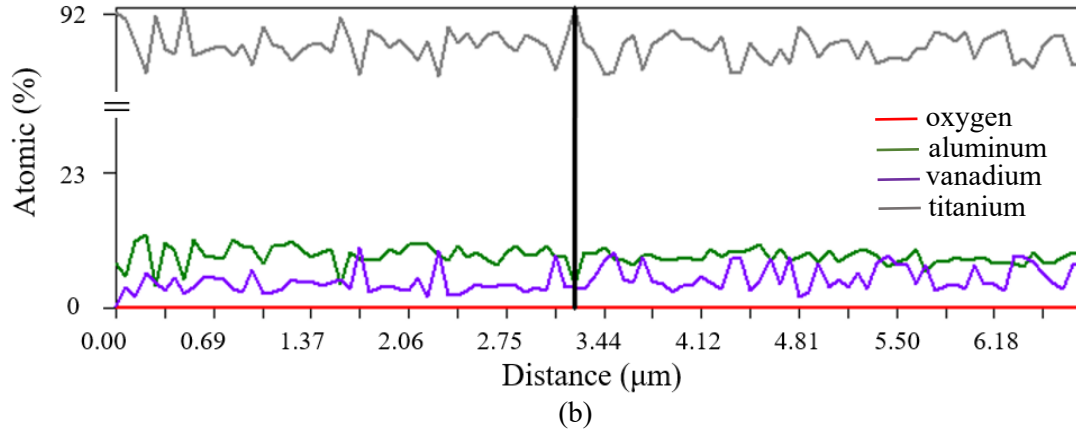
*Figure 3.12. (a) Microstructural image illustrating the decomposition of α' phase into α and β phases in the reference (no preheating) sample. (b) EDS line scan of the reference sample no oxygen peak was observed.*

On the other hand, the microstructure of the preheated samples did not exhibit any detectable β phase, aligning with the findings of the XRD analysis (Figure 3.13). An EDS line scan was performed on the martensitic α plate to determine its chemical composition, as indicated by the red arrow. Two distinctive peaks associated with oxygen were identified, with atomic percentages of 1.98% and 2.22%, respectively (Figure 3.13 (b)).
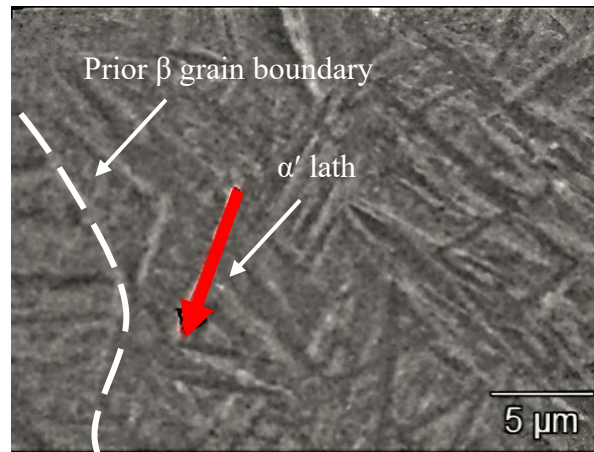


(a)
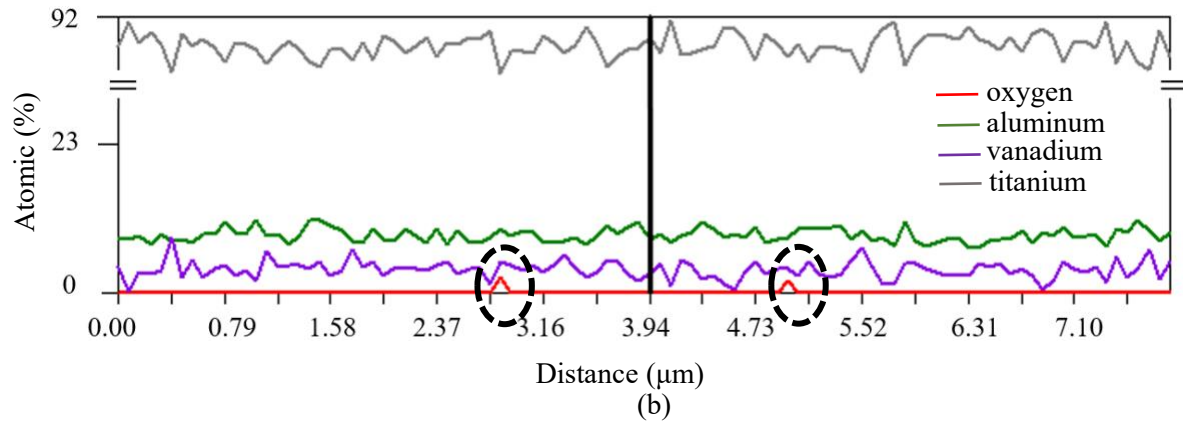
*Figure 3.13. Microstructural examination and EDS analysis of preheated sample (252 W, 1950mm/s, 26.92 j/mm³). (a) Microstructural image revealing the absence of detectable β phase particles in preheated samples. (b) Energy-Dispersive X-ray Spectroscopy (EDS) line scan performed on a single martensitic α plate, illustrating the distribution and concentration levels of interstitial oxygen atoms.*

3.3.3. Mechanical Properties

Figure 3.14 depicts the stress-strain relationship obtained from quasi-static tensile tests performed on three distinct preheated samples and a reference sample, which underwent no preheating. The reference sample demonstrated a strength of 1180 MPa and an elongation of 6.1% before failure, consistent with previous studies on LPBF-fabricated Ti-6Al-4V fabricated. Interestingly, the comparative analysis showed that all selected layerwise preheated samples exhibited higher Ultimate Tensile Strength (UTS) values and elastic modulus than the reference sample. Among the preheated samples, the highest UTS value recorded was 1235 MPa, and the maximum elongation observed was 5.31%. Notably, this UTS value stands as the highest reported for thermally processed LPBF-fabricated Ti-6Al-4V to date [35,36]. However, it's important to note that the elongation of all preheated samples was lower than the reference sample, with the lowest elongation recorded at 4.6% (achieved with a preheating laser scan speed of 1625 mm/s). The preheated samples exhibited higher UTS values, reaching a record high of 1235 MPa. However, their elongation was lower compared to the reference sample. When observing the elastic region of the stress-strain curves, a similar trend is noticeable among all preheated samples up until the yield point. Remarkably, the application of preheating led to a significant improvement in elastic modulus when compared to the reference sample. Specifically, the rigidity of the preheated sample, subjected to a preheating scan speed of 1625 mm/s, was found to be 8% superior to that of the reference.

Figure 3.14 (a)
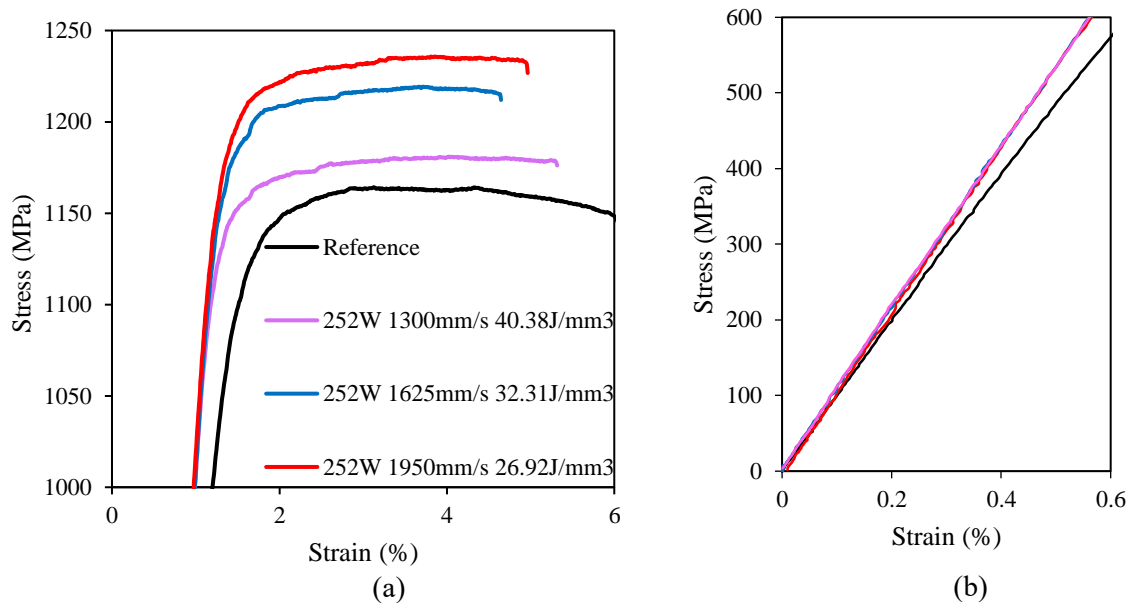
Figure 3.14 (b)

| Preheating Energy Density (mm/s) | Reference | 1950 | 1625 | 1300 |
|---|---|---|---|---|
| Elastic Modulus (GPa) | 101.2± 0.3 | 106.5± 1.1 | 109.1± 2.2 | 109.0± 5.7 |

*Figure 3.14. (a) Stress-Strain Curve for both the reference and the preheated samples, highlighting the differences in material behavior under applied load. (b) Detailed view of the elastic region of the tensile test, including the calculated elastic modulus for the samples.*

The introduction of additional heat input with the application of layerwise preheating was observed to have a remarkable influence on the orientation of localized strains before failure during tensile testing. Figure 3.15 demonstrates the DIC image of the localized strains. The color gradient serves to quantify the strain at local regions and the color map illustrates the distribution of the local strains along the gauge length of the specimen. The DIC image reveals that the high-strain regions (red color) are concentrated at a lower angle with the XY plane (normal to the loading axis) in the reference sample with a degree of 15.76°. The introduction of the preheating laser scan increased the orientation angle up to 43.69°.

| Sample Pre-Speed (mm/s) | 0 (Ref) | 1950 | 1625 | 1300 |
|---|---|---|---|---|
| Strain Angle (°) | 15.76 | 41.98 | 40.35 | 43.69 |
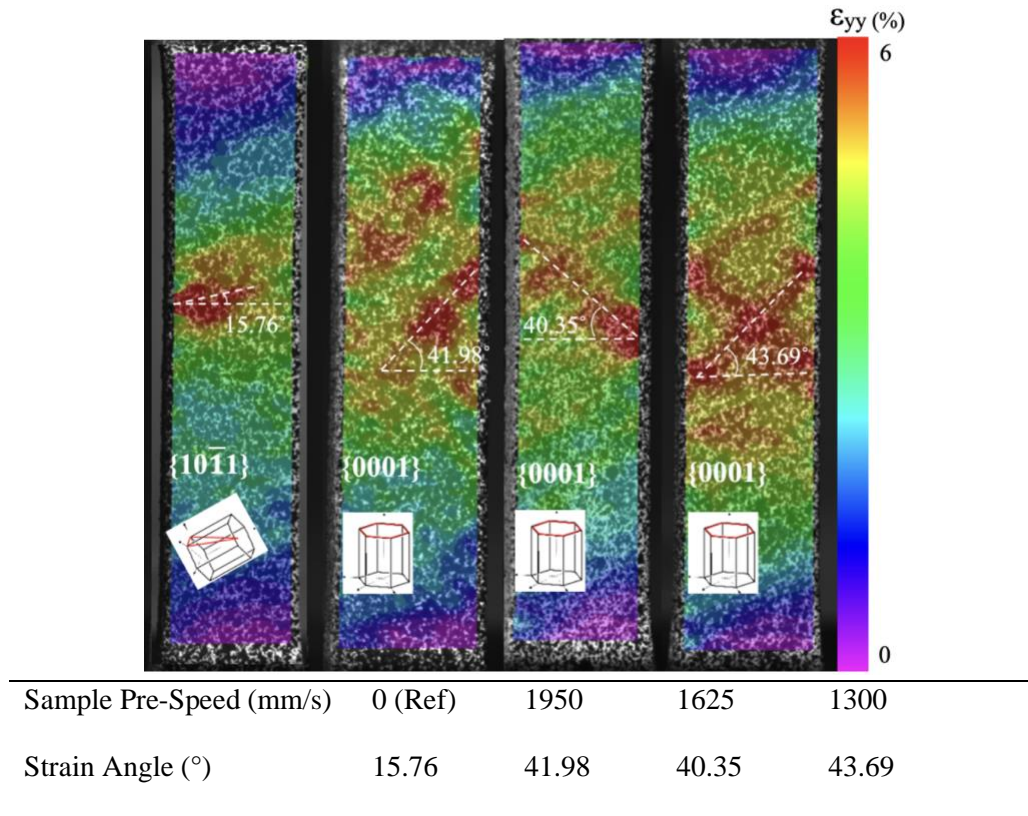
*Figure 3.15. Illustration of global strain evolution resulting from the accumulation of local strains along the axis of applied stress observed just prior to material failure.*

3.4. Discussions

In this chapter, a two-step laser scanning strategy was employed to modify the as-build microstructure of LPBF fabricated Ti-6Al4V. The low-energy preheating laser was utilized to preheat the powder on each layer, followed by a higher-energy melting laser scan for processing. This innovative approach offered precise control over the solidification and cooling rates, thereby eliminating the need for additional post-processing steps. The study extensively investigated the impact of various preheating laser parameters on the microstructure, phase transformation, and mechanical properties of the final part. This discussion presents a comprehensive analysis of the findings and their implications in the realm of additive manufacturing.

3.4.1. Reduction In The Amount of The Defects

Figure 3.2 and Figure 3.3 provide a deeper understanding of how preheating scans influence porosity levels in the microstructure. These figures provide valuable insights into the observed reduction and shed light on the potential role of preheating scans in achieving this effect. By applying preheating scans, additional energy is introduced before the melting of the powder material, causing partial melting between the powder particles. This process restricted the scattering of the larger particles by the incident laser beam, leading to a relatively higher amount of material available for melting in the preheated samples compared to the reference sample [37]. Consequently, the preheated samples exhibited a higher relative density of the material. This finding is in line with previous literature, which has indicated that fine-tuning process parameters, such as laser power and scanning speed, can notably decrease porosity levels in LPBF fabricated parts [38–40]. Another contributing factor to the reduced porosity in the samples could be the increased total heat input associated with the preheating application, coupled with a constant powder bed mass. This combination results in slower heat energy transfer, leading to lower cooling rates and a longer cooling time for the molten metal.

The deformation capacities, both elastic and plastic, of LPBF-fabricated Ti-6Al-4V material are limited due to the grain structure and inherent porosity level, in contrast to conventionally processed Ti-6Al-4V [20,41,42]. The mechanism of pore growth plays a crucial role in plastic deformation during tensile loading, consequently limiting the ability to withstand strain before failure. [43]. Additionally, the porosity level has a severe effect under cyclic loading where the fatigue behavior of the materials becomes critical [44,45]. Previous studies have proven that optimizing process parameters can help alleviate process-related defects, resulting in a relative density of up to 99.98% [20,46,47]. However, the elongation was found to be less than 5% [46]. Figures 2 and 3 demonstrate that utilization of the layerwise preheating laser scan within the energy

density range of 25 J/mm$^3$ to 45 J/mm$^3$ leads to a significant reduction in the porosity of the as-built microstructure. In this chapter, a remarkable improvement in relative density, from 99.53% to 99.99%, was presented. This was coupled with a 20% higher elongation compared to the laser energy optimization study by Han *et al.* [46], without the need for any additional post-processing.

3.4.2. Prior β-Grain Morphology

The prior β grains' structure was influenced by preheating scans and thermal processing conditions, as shown in Figure 3.4. The reference sample exhibited an irregular polygonal shape, while a low-energy preheating scan resulted in a square shape, and higher energy inputs led to circular regions. These findings are in accordance with previous studies, such as the work of Kumar *et al.* [48], who reported a transformation of prior β grain regions from irregular polygonal shapes in as-fabricated samples to square-like shapes after post-processing heat treatment below the β-transus temperature. However, above this temperature, the transformation was disrupted, resulting in irregular shapes. Additionally, Kumar *et al.* [49] noted equiaxed prior β grain morphology in LPBF-fabricated Ti-6Al-4V as a result of a 30µm layer thickness and 67˚ rotation angle combination, compared to the 90° rotation at the same layer thickness. The change in morphology was ascribed to the mismatch between the laser tracks in both the building direction and the XY plane. Finally, in line existing with the literature, all samples in the present study exhibited laths oriented at around 45° with respect to the Z-axis. This orientation is consequence of the relationship between the prior β and the hexagonal α′ lattice relation through Burger's orientation relationships [49,50]. The most favorable relationships are $\{110\}\beta$ // $\{1120\}\alpha'$ and $\{110\}\beta$ // $\langle1120\rangle\alpha$, resulting in the growth of the laths along ~45˚ [49,51].

The presence of the β phase decreases the strength of the LPBF-fabricated Ti-6Al-4V material [36]. The quantity of the beta phase was determined from XRD data [52] and is plotted

for different preheating laser scan speeds and reference samples in Figure 3.11. The data demonstrates that the application of layerwise preheating reduces the amount of the β phase at room temperature. In Figure 3.12, both the β phase and the EDS line scan of the reference sample are depicted. In comparison to the reference sample, the layerwise preheating sample contains substantially less β phase and also exhibits oxygen in the microstructure (Figure 3.13). The increased content of α-Ti phase and additional interstitial oxygen atoms enhance the strength of the material when layerwise preheating is applied, compared to the reference sample.

3.4.3. α/α' Phase Lath Structure

The results, shown in Figure 3.5, demonstrate that layerwise preheating in LBPF-fabricated Ti-6Al-4V microstructure has a significant impact on enhancing the α/α' phases lath thickness uniformity between the XY and ZX planes, reducing the discrepancy to a mere 4.7%. This progress stands in sharp contrast to the non-preheated reference sample, which exhibits a 10% difference. These variations in lath thickness can be attributed to the different heating rates experienced in different planes, which are influenced by the layerwise preheating process. Layerwise preheating process impacts heat transfer in two ways: first, by elevating the temperature of the layer before melting, it reduces the heat rate along the build direction (ZX plane); secondly, preheating can partially melt the layer, leading to a higher heating rate distribution in the XY plane compared to the melting of the XY pure powder layer. As reported by Li *et al.* [53], the diffusion of alloying elements during the stress-relieving heating process in AMed Ti-6Al-4V affects the coarsening of lath thickness in the alloy. At higher heating rates, the coarsening of lath thickness is more pronounced during heating compared to slower heating rates.

Furthermore, as depicted in Figures 3.5 and 3.6, preheating leads to an increase in the average lath thickness across both planes, with the degree of change contingent on the level of

applied energy density. Specifically, preheated samples exhibit a higher probability distribution for α/α' laths at a thickness of 0.6 μm, in contrast to the probability peak at 0.5 μm for the reference sample. This increase in the lath thickness is likely attributed to the increased heat input and reduced cooling rates during the LPBF fabrication process when preheating is employed. It is reported in the literature that as the cooling rates slow down during the solidification, relatively thicker α-Ti phases are observed in the preheated microstructure [31, 32]. These observations align with the findings of Lui *et al.* [56], who noted a similar increase in lath thickness for LPBF-fabricated Ti-6Al-4V samples when exposed to an additional heat input, such as during heat treatment. Therefore, the findings presented in Figures 5 and 6 underscore the substantial impact of layerwise preheating on the evolution of microstructural and distribution of α/α' phases lath thickness in LPBF-fabricated Ti-6Al-4V.

3.4.4. The Effect of Preheating on Crystallography

Figure 3.7 illustrates the XRD profiles of the reference and preheated samples, where noticeable distinctions in peak intensity and orientation emerge. The preheated samples exhibited their highest peak intensity at the (002) plane, while the reference sample displayed the most intense peak at the (101) plane on the XY surface. This difference is attributed to the slower cooling rate associated with preheating. The change in peak intensities indicates an improvement in the isotropy of grain orientation within the L-PBF-fabricated Ti-6Al-4V microstructure. This observation is in line with previous studies comparing XRD diffraction patterns of conventionally processed Ti-6Al-4V, which also exhibit a slower cooling rate, with those of LPBF-fabricated Ti-6Al-4V [31,57].

Additionally, Figure 3.8 demonstrates that the introduction of preheating scans resulted in a transition of the microstrain from tensile to compressive. Although the exact mechanism behind

this shift remains unclear, it could potentially linked to the contraction of the HCP lattice during preheating. An analysis comparing preheated samples disclosed that those exposed to faster scan speeds (correlating with higher cooling rates) demonstrated a higher shift in microstrain mode. This phenomenon could be attributed to the allotropic transformation, particularly the decomposition of $\beta$ into $\beta + \alpha$ phases, leading to a higher presence of vanadium in the HCP lattice, as confirmed in Figure 3.9. This is because the vanadium atoms contributing to the formation of the $\beta$ phase are unable to vacate their positions during the transformation process. Consequently, the increased incorporation of induces a more considerable contraction of the lattice structure, thereby triggering a more noticeable effect relative to that identified at lower cooling rates during the preheating process.

Furthermore, Figure 3.9 reveals that the preheated samples exhibited a higher c/a ratio compared to the reference sample, indicating a more pronounced lattice distortion along the c-axis. This suggests that the preheating process induced structural changes in the material, resulting in a modified lattice arrangement in the HCP phase. This increased c/a ratio is likely a consequence of the reduced heating rate caused by preheating before the melting process on each layer. This is supported by Oh *et al.*'s [58] findings, in which they observed a higher c/a ratio when laser scanning a Ti-6Al-4V plate faster. Also, Figure 3.9 demonstrates a notable decrease in the volume of the HCP lattice as the preheating energy density decreases with an increase in preheating laser scan speed. This reduction can be attributed to the differing diffusivity of solute atoms under varying cooling rates. As preheating scan speeds increase, while laser power remains constant, a consequential decrease in energy density is observed, potentially leading to accelerated cooling rates. During these periods of rapid cooling, the diffusion of solute vanadium atoms into the body-centered cubic (BCC or $\beta$ phase) structure is hindered. This leads to a supersaturated HCP structure

(α/α′ phases), characterized by a higher concentration of vanadium atoms compared to a slower-cooled microstructure (the equilibrium α phase) [51,59,60]. Notably, with smaller vanadium atoms occupying lattice positions typically filled by larger titanium atoms, an overall decrease in the total lattice volume of the HCP structure is observed when compared to the reference microstructure. These findings underscore the need for further investigations to understand the implications of these phenomena on the mechanical properties and performance of Ti-6Al-4V under different conditions, thereby optimizing LPBF processes for this material.

The results of this chapter also demonstrated a substantial reduction in the β-phase content in all preheated samples compared to the reference sample (Figure 3.11). The discovery suggests that preheating plays a significant role in modifying the material's microstructure, particularly the distribution of the β-phase. In the reference sample, the decomposition of the α′ phase into α + β phases mirrors the microstructural transformations described by Tan *et al.* [12]. The presence of fine β phase particles within α-laths and the emergence of thicker Widmanstätten laths, which accommodate the growth of α′ martensitic plates, reflect the transformation sequence Tan *et al.* outlined—initially in the Melt state, transitioning to β prior, then to a mixture of α′, α primary, and β retained, ultimately leading to αsecondary and β (Figure 3.12). In contrast, the preheated samples, in agreement with the XRD results, did not exhibit detectable β phase particles (Figure 23 (a)). This absence of β phase particles aligns with the known effects of preheating on the phase transformation, leading to a more uniform and stable α-phase structure. Furthermore, an EDS line scan on the martensitic α plate identified two distinct oxygen peaks (Figure 2.13b). This observation supports previous research [16, 19] suggesting that oxygen atoms can occupy various interstitial sites within the HCP lattice, depending on the energy state of the system. The presence

55

of oxygen and its percentage within the lattice, influenced by preheating, suggest a potential mechanism for modifying mechanical properties [16,19].

Figure 3.7 illustrates a shift in the XRD peak pattern due to the application of layerwise preheating, indicating a change in grain orientation. In the original state, the strongest Bragg peak was observed at the (101) plane, whereas the application of layerwise preheating shifted the peak to the (002) plane. The change in grain orientation impacts the active slip systems of the microstructure [63]. These active slip systems in the HCP lattice can be categorized as prismatic, basal, and pyramidal, with CRSS values of 181MPa, 209MPa, and 474MPa, respectively [63]. It has been reported that a change in the deformation mechanism or slip system to a stronger one, as well as the activation of multiple slip systems due to grain orientation, can enhance the mechanical strength of LPBF-fabricated Ti-6Al-4V [32,63]. The observed increase in UTS in this chapter could be attributed to the change to a stronger slip system.

3.4.5. HCP Lattice Transformation and Microstrain Mode

The presence of residual stress in L-PBF Ti-6Al-4V is a well-documented limitation that hinders the strength and plasticity of the material [64]. The magnitude of micro stress serves as an indicator of residual stress at the macroscopic level [65]. Higher residual micro stress directly corresponds to higher residual macro stress [65]. In this chapter, the microstrain was assessed by utilizing the Williamson-Hall (W-H) method, providing a direct means to examine the impact of residual stress levels (which are directly proportional to the microstrain) on the mechanical response of the components [66]. Previous studies reported that decreasing residual stress can enhance the mechanical properties of LPBF-fabricated Ti-6Al-4V material [67]. It was noted that microstrain decreased with the implementation of layerwise preheating. The initial state of the LPBF-fabricated Ti-6Al-4V material was under tension mode and exhibited a positive microstrain

value (Figure 3.8). The application of layerwise preheating modified the microstrain mode from tension to compression (Figure 3.8). This change was considered to be one of the contributing factors that improved the mechanical strength of the material after layerwise preheating.

Figure 3.9a depicts the lattice distortion of the HCP $\alpha/\alpha'$ phases, revealing an inverse relationship between energy input and lattice distortion. Higher energy input during layerwise preheating results in reduced lattice distortion, attributed to slower cooling rates [68]. In Figure 3.9b there is an increase in HCP lattice volume corresponding to increasing energy input. Figures 9a and b imply that lower energy input during layerwise preheating pronounces in more lattice distortion and, consequently, a relatively smaller lattice volume. This is due to the restricted diffusion of vanadium atoms from the HCP lattice at a faster cooling rate. The lattice deformation caused by layerwise preheating is rationalized by the entrapment of interstitial oxygen atoms in the octahedral positions, which distort the lattice along the c edge [69] (Figure 3.10). This lattice distortion of the HCP lattice due to interstitial oxygen and substitutional vanadium atoms contributes to the strengthening of the layerwise preheated Ti-6Al-4V [70].

3.4.6. The Impact of Preheating On The Mechanical Properties

The complex microstructure of $\alpha$ and $\beta$ phases of the as-built grain structure induces micro-plasticity at stress levels considerably below its macroscopic yield strength [43]. Thus, it controls the ductility of the LPBF-fabricated Ti-6Al-4V. The orientation of the prior $\beta$ grain boundaries affects the growth of the $\alpha/\alpha'$ phases during the $\beta \rightarrow \beta + \alpha$ decomposition [49,50]. Previous studies have reported that a microstructure with rectangular-shaped prior $\beta$ grain boundaries exhibits lower elongation (%) [48]. Zou *et al.* [70]reported that refined quasi-equiaxed prior $\beta$ grain boundaries enhance the strength of the LPBF-fabricated Ti-6Al-4V material. As shown in Figure 3.4, the layerwise preheating modifies the morphology of the prior $\beta$ grain boundaries, leading to an

increase in the strength while decreasing the elongation of the material, supporting the aforementioned studies above.

The influence of α/α′ phases lath thickness on mechanical behavior of LPBF-fabricated Ti-6Al-4Vis a well-known phenomenon, as described by the Hall-Petch relation [71]. Generally, thinner laths provide relatively higher strength [72,73]. However, when examining the relationship between elongation and lath thickness, it becomes more complex due to variations in slip length along grain boundaries [71,74]. With the application of layerwise preheating laser scan the α-Ti phases lath thickness increased by up to 17% (at the energy density of 44.87 J/mm3), compared to the reference condition (Figure 3.5). The probability distribution of the thicker laths in the modified microstructure is depicted in Figure 3.6. On the contrary to the existing literature [72,73], it was observed that layerwise preheated Ti-6Al-4V, with a thicker lath distribution, demonstrated a 6% higher UTS compared to the as-built condition.

Layerwise preheating had an effect on both the mechanical strength of the material and deformation behavior of LPBF-fabricated Ti-6Al-4V (see Figure 3.14). In Figure 3.15 it is shown that the angle of orientation for localized strains was observed to rise in the direction of the applied stress with the application preheating. The deformation behavior in LPBF-fabricated Ti-6Al-4V under monotonic tension is primarily governed by the activated slip systems [74]. The α-Ti phase HCP lattice possesses five potential active slip systems, namely $\{0001\}$ $<11\bar{2}0>$(basal), $\{10\bar{1}0\}$ $<11\bar{2}0>$ (prismatic), $\{10\bar{1}1\}$ $<11\bar{2}0>$ (pyramidal), $\{10\bar{1}1\}$ $<11\bar{2}\bar{3}>$ (pyramidal), and $\{11\bar{2}2\}$ $<11\bar{2}\bar{3}>$ (pyramidal) [75]. Each slip system has a distinct gliding angle. The notable increase in strain orientation can be attributed to the altered gliding angle of the slip system resulting from the modified microstructure induced by layerwise preheating.

## 3.5. References

[1]     S. Herranz, F.J. Campa, L.N.L. de Lacalle, A. Rivero, et al, The milling of airframe components with low rigidity: a general approach to avoid static and dynamic problems, Proceedings of the Institution of Mechanical Engineers. 219 (2005) 789–801.

[2]     D. Palmeri, G. Buffa, G. Pollara, L. Fratini, The Effect of Building Direction on Microstructure and Microhardness during Selective Laser Melting of Ti6Al4V Titanium Alloy, J Mater Eng Perform. 30 (2021) 8725–8734. https://doi.org/10.1007/s11665-021-06039-x.

[3]     S. Liu, Y.C. Shin, Additive manufacturing of Ti6Al4V alloy: A review, Mater Des. 164 (2019) 107552. https://doi.org/https://doi.org/10.1016/j.matdes.2018.107552.

[4]     T.S. Tshephe, S.O. Akinwamide, E. Olevsky, P.A. Olubambi, Additive manufacturing of titanium-based alloys- A review of methods, properties, challenges, and prospects, Heliyon. 8 (2022) e09041. https://doi.org/https://doi.org/10.1016/j.heliyon.2022.e09041.

[5]     A. Gomez-Gallegos, P. Mandal, D. Gonzalez, N. Zuelli, P. Blackwell, Studies on Titanium Alloys for Aerospace Application, Defect and Diffusion Forum. 385 (2018) 419–423. https://doi.org/https://doi.org/10.4028/www.scientific.net/DDF.385.419.

[6]     Robert I. Jaffee, Harris M. Burte, Titanium Science and Technology, Springer, 1973.

[7]     P.K. Gokuldoss, S. Kolla, J. Eckert, Additive Manufacturing Processes: Selective Laser Melting, Electron Beam Melting and Binder Jetting—Selection Guidelines, Materials. 10 (2017). https://doi.org/10.3390/ma10060672.

[8]     I. Yadroitsev, P. Krakhmalev, I. Yadroitsava, Selective laser melting of Ti6Al4V alloy for biomedical applications: Temperature monitoring and microstructural evolution, J Alloys Compd. 583 (2014) 404–409. https://doi.org/https://doi.org/10.1016/j.jallcom.2013.08.183.

[9]     S. Ren, Y. Chen, T. Liu, X. Qu, Effect of Build Orientation on Mechanical Properties and Microstructure of Ti-6Al-4V Manufactured by Selective Laser Melting: Physical Metallurgical and Materials Science, Metallurgical and Materials Transactions. 50 (2019) 4388–4409. https://doi.org/https://doi.org/10.1007/s11661-019-05322-w.

[10]    B. Zhou, J. Zhou, H. Li, F. Lin, A study of the microstructures and mechanical properties of Ti6Al4V fabricated by SLM under vacuum, Materials Science and Engineering: A. 724 (2018) 1–10. https://doi.org/10.1016/j.msea.2018.03.021.

[11]    W. Xu, S. Sun, J. Elambasseril, Q. Liu, M. Brandt, M. Qian, Ti-6Al-4V Additively Manufactured by Selective Laser Melting with Superior Mechanical Properties, JOM. 67 (2015) 668–673. https://doi.org/10.1007/s11837-015-1297-8.

[12]    X. Tan, Y. Kok, W.Q. Toh, Y.J. Tan, M. Descoins, D. Mangelinck, S.B. Tor, K.F. Leong, C.K. Chua, Revealing martensitic transformation and α/β interface evolution in electron beam melting three-dimensional-printed Ti-6Al-4V, Sci Rep. 6 (2016) 26039. https://doi.org/10.1038/srep26039.

[13]    H. Ali, L. Ma, H. Ghadbeigi, K. Mumtaz, In-situ residual stress reduction, martensitic decomposition and mechanical properties enhancement through high temperature powder bed pre-heating of Selective Laser Melted Ti6Al4V, Materials Science and Engineering: A. 695 (2017) 211–220. https://doi.org/https://doi.org/10.1016/j.msea.2017.04.033.

[14]    B. Vrancken, S. Buls, J.-P. Kruth, J. Van Humbeeck, Influence of preheating and oxygen content on Selective Laser Melting of Ti6Al4V, in: Proceedings of the 16th RAPDASA Conference, 2015.

[15]    J.-P. Kruth, J. Deckers, E. Yasa, R. Wauthlé, Assessing and comparing influencing factors of residual stresses in selective laser melting using a novel analysis method, Proc Inst Mech Eng B J Eng Manuf. 226 (2012) 980–991. https://doi.org/10.1177/0954405412437085.

[16]    M. Motyka, A. Baran-Sadleja, J. Sieniawski, M. Wierzbinska, K. Gancarczyk, Decomposition of deformed $\alpha'$($\alpha''$) martensitic phase in Ti–6Al–4V alloy, Materials Science and Technology. 35 (2019) 260–272. https://doi.org/10.1080/02670836.2018.1466418.

[17]    S.Q. Wu, Y.J. Lu, Y.L. Gan, T.T. Huang, C.Q. Zhao, J.J. Lin, S. Guo, J.X. Lin, Microstructural evolution and microhardness of a selective-laser-melted Ti–6Al–4V alloy after post heat treatments, J Alloys Compd. 672 (2016) 643–652. https://doi.org/10.1016/j.jallcom.2016.02.183.

[18]   S. Cao, R. Chu, X. Zhou, K. Yang, Q. Jia, C.V.S. Lim, A. Huang, X. Wu, Role of martensite decomposition in tensile properties of selective laser melted Ti-6Al-4V, J Alloys Compd. 744 (2018) 357–363. https://doi.org/10.1016/j.jallcom.2018.02.111.

[19]   S. Cao, Q. Hu, A. Huang, Z. Chen, M. Sun, J. Zhang, C. Fu, Q. Jia, C.V.S. Lim, R.R. Boyer, Y. Yang, X. Wu, Static coarsening behaviour of lamellar microstructure in selective laser melted Ti–6Al–4V, J Mater Sci Technol. 35 (2019) 1578–1586. https://doi.org/10.1016/j.jmst.2019.04.008.

[20]   G. Kasperovich, J. Hausmann, Improvement of fatigue resistance and ductility of TiAl6V4 processed by selective laser melting, J Mater Process Technol. 220 (2015) 202–214. https://doi.org/10.1016/j.jmatprotec.2015.01.025.

[21]   N. Saiz, J. Pegues, S. Whetten, A. Kustas, T. Chilson, HEAT TREATMENT EFFECTS ON MECHANICAL PROPERTIES OF WIRE ARC ADDITIVE MANUFACTURED Ti-6Al-4V, n.d.

[22]   C. Su, H. Yu, Z. Wang, J. Yang, X. Zeng, Controlling the tensile and fatigue properties of selective laser melted Ti–6Al–4V alloy by post treatment, J Alloys Compd. 857 (2021) 157552. https://doi.org/https://doi.org/10.1016/j.jallcom.2020.157552.

[23]   C. Cai, X. Gao, Q. Teng, M. Li, K. Pan, B. Song, C. Yan, Q. Wei, Y. Shi, A novel hybrid selective laser melting/hot isostatic pressing of near-net shaped Ti-6Al-4V alloy using an in-situ tooling: Interfacial microstructure evolution and enhanced mechanical properties, Materials Science and Engineering: A. 717 (2018) 95–104. https://doi.org/https://doi.org/10.1016/j.msea.2018.01.079.

[24]   W. Xu, M. Brandt, S. Sun, J. Elambasseril, Q. Liu, K. Latham, K. Xia, M. Qian, Additive manufacturing of strong and ductile Ti–6Al–4V by selective laser melting via in situ martensite decomposition, Acta Mater. 85 (2015) 74–84. https://doi.org/10.1016/j.actamat.2014.11.028.

[25]   W. Xu, E.W. Lui, A. Pateras, M. Qian, M. Brandt, In situ tailoring microstructure in additively manufactured Ti-6Al-4V for superior mechanical performance, Acta Mater. 125 (2017) 390–400. https://doi.org/10.1016/j.actamat.2016.12.027.

[26]   EOS GmbH, EOS Titanium Ti64 - Material data sheet, (2017).

[27]   L. Thijs, F. Verhaeghe, T. Craeghs, J. Van Humbeeck, J.-P. Kruth, A study of the microstructural evolution during selective laser melting of Ti–6Al–4V, Acta Mater. 58 (2010) 3303–3312. https://doi.org/https://doi.org/10.1016/j.actamat.2010.02.004.

[28]   A. Khorsand Zak, W.H. Abd. Majid, M.E. Abrishami, R. Yousefi, X-ray analysis of ZnO nanoparticles by Williamson-Hall and size-strain plot methods, Solid State Sci. 13 (2011) 251–256. https://doi.org/10.1016/j.solidstatesciences.2010.11.024.

[29]   C.A. Schneider, W.S. Rasband, K.W. Eliceiri, NIH Image to ImageJ: 25 years of image analysis, Nat Methods. 9 (2012) 671–675. https://doi.org/10.1038/nmeth.2089.

[30]   T. Pasang, B. Tavlovich, O. Yannay, B. Jakson, M. Fry, Y. Tao, C. Turangi, J.C. Wang, C.P. Jiang, Y. Sato, M. Tsukamoto, W. Misiolek, Directionally-dependent mechanical properties of Ti6Al4V manufactured by electron beam melting (EBM) and selective laser melting (SLM), Materials. 14 (2021). https://doi.org/10.3390/ma14133603.

[31]   M. V. Pantawane, Y.H. Ho, S.S. Joshi, N.B. Dahotre, Computational Assessment of Thermokinetics and Associated Microstructural Evolution in Laser Powder Bed Fusion Manufacturing of Ti6Al4V Alloy, Sci Rep. 10 (2020) 1–14. https://doi.org/10.1038/s41598-020-63281-4.

[32]   D. Zhang, L. Wang, H. Zhang, A. Maldar, G. Zhu, W. Chen, J.-S. Park, J. Wang, X. Zeng, Effect of heat treatment on the tensile behavior of selective laser melted Ti-6Al-4V by in situ X-ray characterization, Acta Mater. 189 (2020) 93–104. https://doi.org/https://doi.org/10.1016/j.actamat.2020.03.003.

[33]   H.P. Klug, L.E. (Leroy E. Alexander, X-ray diffraction procedures for polycrystalline and amorphous materials, 2d ed., Wiley, New York, 1974.

[34]   J. Yang, H. Yu, J. Yin, M. Gao, Z. Wang, X. Zeng, Formation and control of martensite in Ti-6Al-4V alloy produced by selective laser melting, Mater Des. 108 (2016) 308–318. https://doi.org/10.1016/j.matdes.2016.06.117.

[35]   X. Yan, S. Yin, C. Chen, C. Huang, R. Bolot, R. Lupoi, M. Kuang, W. Ma, C. Coddet, H. Liao, M. Liu, Effect of heat treatment on the phase transformation and mechanical properties of Ti6Al4V fabricated by

selective laser melting, J Alloys Compd. 764 (2018) 1056–1071. https://doi.org/https://doi.org/10.1016/j.jallcom.2018.06.076.

[36] S. Cao, Y. Zou, C.V.S. Lim, X. Wu, Review of laser powder bed fusion (LPBF) fabricated Ti-6Al-4V: process, post-process treatment, microstructure, and property, Light: Advanced Manufacturing. 2 (2021) 1. https://doi.org/10.37188/lam.2021.020.

[37] H. Gong, J.J.S. Dilip, L. Yang, C. Teng, B. Stucker, Influence of small particles inclusion on selective laser melting of Ti-6Al-4V powder, IOP Conf Ser Mater Sci Eng. 272 (2017) 12024. https://doi.org/10.1088/1757-899X/272/1/012024.

[38] B. Fotovvati, M. Balasubramanian, E. Asadi, Modeling and Optimization Approaches of Laser-Based Powder-Bed Fusion Process for Ti-6Al-4V Alloy, Coatings. 10 (2020) 1104. https://doi.org/10.3390/coatings10111104.

[39] P. Promoppatum, R. Onler, S.-C. Yao, Numerical and experimental investigations of micro and macro characteristics of direct metal laser sintered Ti-6Al-4V products, J Mater Process Technol. 240 (2017) 262–273. https://doi.org/10.1016/j.jmatprotec.2016.10.005.

[40] G. Kasperovich, J. Haubrich, J. Gussone, G. Requena, Correlation between porosity and processing parameters in TiAl6V4 produced by selective laser melting, Mater Des. 105 (2016) 160–170. https://doi.org/10.1016/j.matdes.2016.05.070.

[41] Q. Huang, X. Liu, X. Yang, R. Zhang, Z. Shen, Q. Feng, Specific heat treatment of selective laser melted Ti–6Al–4V for biomedical applications, Front Mater Sci. 9 (2015) 373–381. https://doi.org/10.1007/s11706-015-0315-7.

[42] F. Bartolomeu, M. Gasik, F.S. Silva, G. Miranda, Mechanical Properties of Ti6Al4V Fabricated by Laser Powder Bed Fusion: A Review Focused on the Processing and Microstructural Parameters Influence on the Final Properties, Metals (Basel). 12 (2022) 986. https://doi.org/10.3390/met12060986.

[43] T. Voisin, N.P. Calta, S.A. Khairallah, J.-B. Forien, L. Balogh, R.W. Cunningham, A.D. Rollett, Y.M. Wang, Defects-dictated tensile properties of selective laser melted Ti-6Al-4V, Mater Des. 158 (2018) 113–126. https://doi.org/10.1016/j.matdes.2018.08.004.

[44] S.P. Narra, A.D. Rollett, A. Ngo, D. Scannapieco, M. Shahabi, T. Reddy, J. Pauza, H. Taylor, C. Gobert, E. Diewald, F.X. Dugast, A. To, R. Wicker, J. Beuth, J.J. Lewandowski, Process qualification of laser powder bed fusion based on processing-defect structure-fatigue properties in Ti-6Al-4V, J Mater Process Technol. 311 (2023) 117775. https://doi.org/10.1016/j.jmatprotec.2022.117775.

[45] X. Gao, C. Tao, S. Wu, B. Chen, S. Wu, X-ray imaging of defect population and the effect on high cycle fatigue life of laser additive manufactured Ti6Al4V alloys, Int J Fatigue. 162 (2022) 106979. https://doi.org/10.1016/j.ijfatigue.2022.106979.

[46] J. Han, J. Yang, H. Yu, J. Yin, M. Gao, Z. Wang, X. Zeng, Microstructure and mechanical property of selective laser melted Ti6Al4V dependence on laser energy density, Rapid Prototyp J. 23 (2017) 217–226. https://doi.org/10.1108/RPJ-12-2015-0193.

[47] M.A. Buhairi, F.M. Foudzi, F.I. Jamhari, A.B. Sulong, N.A.M. Radzuan, N. Muhamad, I.F. Mohamed, A.H. Azman, W.S.W. Harun, M.S.H. Al-Furjan, Review on volumetric energy density: influence on morphology and mechanical properties of Ti6Al4V manufactured via laser powder bed fusion, Progress in Additive Manufacturing. 8 (2023) 265–283. https://doi.org/10.1007/s40964-022-00328-0.

[48] P. Kumar, U. Ramamurty, Microstructural optimization through heat treatment for enhancing the fracture toughness and fatigue crack growth resistance of selective laser melted Ti6Al4V alloy, Acta Mater. 169 (2019) 45–59. https://doi.org/https://doi.org/10.1016/j.actamat.2019.03.003.

[49] P. Kumar, O. Prakash, U. Ramamurty, Micro-and meso-structures and their influence on mechanical properties of selectively laser melted Ti-6Al-4V, Acta Mater. 154 (2018) 246–260. https://doi.org/10.1016/j.actamat.2018.05.044.

[50] E. Lee, R. Banerjee, S. Kar, D. Bhattacharyya, H.L. Fraser, Selection of α variants during microstructural evolution in *α/β* titanium alloys, Philosophical Magazine. 87 (2007) 3615–3627. https://doi.org/10.1080/14786430701373672.

[51]  A.A. Antonysamy, J. Meyer, P.B. Prangnell, Effect of build geometry on the β-grain structure and texture in additive manufacture of Ti6Al4V by selective electron beam melting, Mater Charact. 84 (2013) 153–168. https://doi.org/10.1016/j.matchar.2013.07.012.

[52]  X. Zhao, S. Li, M. Zhang, Y. Liu, T.B. Sercombe, S. Wang, Y. Hao, R. Yang, L.E. Murr, Comparison of the microstructures and mechanical properties of Ti–6Al–4V fabricated by selective laser melting and electron beam melting, Mater Des. 95 (2016) 21–31. https://doi.org/10.1016/j.matdes.2015.12.135.

[53]  J. Li, X. Lin, J. Wang, M. Zheng, P. Guo, Y. Zhang, Y. Ren, J. Liu, W. Huang, Effect of stress-relief annealing on anodic dissolution behaviour of additive manufactured Ti-6Al-4V via laser solid forming, Corros Sci. 153 (2019) 314–326. https://doi.org/10.1016/j.corsci.2019.04.002.

[54]  H.K. Rafi, N. V Karthik, H. Gong, T.L. Starr, B.E. Stucker, Microstructures and Mechanical Properties of Ti6Al4V Parts Fabricated by Selective Laser Melting and Electron Beam Melting, J Mater Eng Perform. 22 (2013) 3872–3883. https://doi.org/10.1007/s11665-013-0658-0.

[55]  M. Neikter, P. Åkerfeldt, R. Pederson, M.L. Antti, Microstructure characterisation of Ti-6Al-4V from different additive manufacturing processes, IOP Conf Ser Mater Sci Eng. 258 (2017). https://doi.org/10.1088/1757-899X/258/1/012007.

[56]  E.W. Lui, A.E. Medvedev, D. Edwards, M. Qian, M. Leary, M. Brandt, Microstructure modification of additive manufactured Ti-6Al-4V plates for improved ballistic performance properties, J Mater Process Technol. 301 (2022) 117436. https://doi.org/10.1016/j.jmatprotec.2021.117436.

[57]  J.-Y. Huang, C.-H. Chang, W.-C. Wang, M.-J. Chou, C.-C. Tseng, P.-W. Tu, Systematic evaluation of selective fusion additive manufacturing based on thermal energy source applied in processing of titanium alloy specimens for medical applications, The International Journal of Advanced Manufacturing Technology. 109 (2020) 2421–2429. https://doi.org/10.1007/s00170-020-05797-7.

[58]  S.A. Oh, R.E. Lim, J.W. Aroh, A.C. Chuang, B.J. Gould, B. Amin-Ahmadi, J. V. Bernier, T. Sun, P.C. Pistorius, R.M. Suter, A.D. Rollett, High speed synchrotron X-ray diffraction experiments resolve microstructure and phase transformation in laser processed Ti-6Al-4V, Mater Res Lett. 9 (2021) 429–436. https://doi.org/10.1080/21663831.2021.1966537.

[59]  E. Sallica-Leva, R. Caram, A.L. Jardini, J.B. Fogagnolo, Ductility improvement due to martensite α′ decomposition in porous Ti–6Al–4V parts produced by selective laser melting for orthopedic implants, J Mech Behav Biomed Mater. 54 (2016) 149–158. https://doi.org/10.1016/j.jmbbm.2015.09.020.

[60]  F.R. Kaschel, R.K. Vijayaraghavan, A. Shmeliov, E.K. McCarthy, M. Canavan, P.J. McNally, D.P. Dowling, V. Nicolosi, M. Celikin, Mechanism of stress relaxation and phase transformation in additively manufactured Ti-6Al-4V via in situ high temperature XRD and TEM analyses, Acta Mater. 188 (2020) 720–732. https://doi.org/10.1016/j.actamat.2020.02.056.

[61]  S.K. Nayak, C.J. Hung, V. Sharma, S.P. Alpay, A.M. Dongare, W.J. Brindley, R.J. Hebert, Insight into point defects and impurities in titanium from first principles, NPJ Comput Mater. 4 (2018). https://doi.org/10.1038/s41524-018-0068-9.

[62]  H. Wu, OXYGEN DIFFUSION THROUGH TITANIUM AND OTHER HCP METALS BY, (2013).

[63]  J. Gong, A.J. Wilkinson, Anisotropy in the plastic flow properties of single-crystal α titanium determined from micro-cantilever beams, Acta Mater. 57 (2009) 5693–5705. https://doi.org/10.1016/j.actamat.2009.07.064.

[64]  H. Ali, H. Ghadbeigi, K. Mumtaz, Effect of scanning strategies on residual stress and mechanical properties of Selective Laser Melted Ti6Al4V, Materials Science and Engineering: A. 712 (2018) 175–187. https://doi.org/10.1016/j.msea.2017.11.103.

[65]  X.P. Ren, H.Q. Li, H. Guo, F.L. Shen, C.X. Qin, E.T. Zhao, X.Y. Fang, A comparative study on mechanical properties of Ti–6Al–4V alloy processed by additive manufacturing vs. traditional processing, Materials Science and Engineering: A. 817 (2021) 141384. https://doi.org/10.1016/j.msea.2021.141384.

[66]  F.R. Kaschel, S. Keaveney, D.P. Dowling, Comparison between continuous and modulated wave laser emission modes for the selective laser melting of Ti-6Al-4V: Dimensional accuracy, microstructure and mechanical behaviour, Addit Manuf. 55 (2022) 102825. https://doi.org/10.1016/j.addma.2022.102825.

[67]  F.R. Kaschel, R.K. Vijayaraghavan, P.J. McNally, D.P. Dowling, M. Celikin, In-situ XRD study on the effects of stress relaxation and phase transformation heat treatments on mechanical and microstructural

behaviour of additively manufactured Ti-6Al-4V, Materials Science and Engineering: A. 819 (2021) 141534. https://doi.org/10.1016/j.msea.2021.141534.

[68]     A. Panin, S. Martynov, M. Kazachenok, L. Kazantseva, A. Bakulin, S. Kulkova, O. Perevalova, E. Sklyarova, Effects of Water Cooling on the Microstructure of Electron Beam Additive-Manufactured Ti-6Al-4V, Metals (Basel). 11 (2021) 1742. https://doi.org/10.3390/met11111742.

[69]     D.W. Wang, Y.H. Zhou, J. Shen, Y. Liu, D.F. Li, Q. Zhou, G. Sha, P. Xu, T. Ebel, M. Yan, Selective laser melting under the reactive atmosphere: A convenient and efficient approach to fabricate ultrahigh strength commercially pure titanium without sacrificing ductility, Materials Science and Engineering: A. 762 (2019) 138078. https://doi.org/10.1016/j.msea.2019.138078.

[70]     Z. Zou, M. Simonelli, J. Katrib, G. Dimitrakis, R. Hague, Microstructure and tensile properties of additive manufactured Ti-6Al-4V with refined prior-β grain structure obtained by rapid heat treatment, Materials Science and Engineering: A. 814 (2021) 141271. https://doi.org/10.1016/j.msea.2021.141271.

[71]     P. Wanjara, D. Backman, F. Sikan, J. Gholipour, R. Amos, P. Patnaik, M. Brochu, Microstructure and Mechanical Properties of Ti-6Al-4V Additively Manufactured by Electron Beam Melting with 3D Part Nesting and Powder Reuse Influences, Journal of Manufacturing and Materials Processing. 6 (2022) 21. https://doi.org/10.3390/jmmp6010021.

[72]     N. Hrabe, T. Quinn, Effects of processing on microstructure and mechanical properties of a titanium alloy (Ti–6Al–4V) fabricated using electron beam melting (EBM), Part 2: Energy input, orientation, and location, Materials Science and Engineering: A. 573 (2013) 271–277. https://doi.org/10.1016/j.msea.2013.02.065.

[73]     Q. Zhang, J. Xie, T. London, D. Griffiths, I. Bhamji, V. Oancea, Estimates of the mechanical properties of laser powder bed fusion Ti-6Al-4V parts using finite element models, Mater Des. 169 (2019) 107678. https://doi.org/10.1016/j.matdes.2019.107678.

[74]     F. Bridier, P. Villechaise, J. Mendez, Analysis of the different slip systems activated by tension in a α/β titanium alloy in relation with local crystallographic orientation, Acta Mater. 53 (2005) 555–567. https://doi.org/10.1016/j.actamat.2004.09.040.

[75]     O. Diard, S. Leclercq, G. Rousselier, G. Cailletaud, Evaluation of finite element based analysis of 3D multicrystalline aggregates plasticity: Application to crystal plasticity model identification and the study of stress and strain fields near grain boundaries, Int J Plast. 21 (2005) 691–722. https://doi.org/https://doi.org/10.1016/j.ijplas.2004.05.017.

# 4. AN INNOVATIVE BREAKTHROUGH IN IN-SITU THERMAL PROCESSING FOR LPBF: COMBINING PREHEATING AND POST-HEATING LASER SCAN FOR Ti-6Al-4V

## 4.1 Introduction and Overview

Ti-6Al-4V alloy stands out as the most preferred titanium alloy renowned for its exceptional mechanical properties [1]. Its impressive strength-to-weight ratio, extraordinary fracture toughness, resistance at corrosive environments, and biocompatibility have made it the top choice for manufacturing durable lightweight components needed for the automotive, aerospace, and biomedical industries [2]. These exceptional attributes have propelled ~~Ti-6Al-4V~~ to significant prominence for additive manufacturing (AM) applications [2].

AM technology emerged in the 1980s and has seen a surge in interest over the last two decades, especially among researchers, due to its capability for fabricating complex geometry [3,4]. Metal AM in aerospace applications offers significant advantages substantial cost and lead-time reduction, mass reduction through highly efficient and lightweight designs, consolidation of multiple components for performance enhancement, and the utilization of novel materials [5]. In addition to these benefits, AM technology enhanced the sustainability of the fabrication by reducing material waste and minimizing energy consumption. the required energy needs [6].

Advanced aerospace components like impellers, turbine blades, and airfoils are fabricated using novel materials such as Ti-6Al-4V, leveraging the advantages offered by AM technology [5,7]. Laser powder bed fusion (LPBF) technology is the most adequate fabrication technique among the other metal additive manufacturing techniques due to its capability to fabricate very fine features which is also termed as the resolution [8]. Utilizing the LPBF techniques on Titanium material enables the production of complex-shaped lightweight engineering components with outstanding mechanical characteristics [9–13].

A high-power laser beam is exposed to micron-level regions interacting with loose powder at very high scanning speeds. This heat source and powder material interaction led to rapid solidification and cooling rates which delivered highly stressed parts due to the accelerated shrinkage and contraction [14–

64

16]. Additionally, heat dissipation through the build material underneath the melt pool promotes directional solidification which turns out as a grain texture in the final microstructure [17–19]. The microstructure of the LPBF-fabricated Ti-6al-4V exhibits an anisotropic mechanical response [20–24].

Despite its capability for complex lightweight geometry fabrication and superior mechanical properties, LPBF-fabricated Ti-6Al-4V has a challenging microstructure that limits the engineering application of this technology and still needs to be fully addressed. There are studies seeking solutions to address these issues through optimization of the process parameters [25,26]. In addition to these, there were a great number of reported studies investigating the impact of the post heat treatment (HT) [27–32]. Due to the requirement for the advanced equipment HT increases the production cost as well as the lead time. To avoid the expense and extra effort to optimize complementary processes for modifying the complex microstructure of LPBF-fabricated Ti-6Al-4V, an innovative in-situ thermal process was proposed in this chapter.

A combination of a preheating laser scan and a post-heating laser scan was performed alongside the melting laser scan to regulate the rapid cooling during the fabrication. The effect of the laser parameters during preheating and post-heating was evaluated. The impact of the preheating and post-heating laser scans on the porosity level was evaluated and a noteworthy enhancement was noticed compared to the reference sample condition which was built with a single laser scan (only melting laser scan). The effect of the preheating and post-heating laser scan on the microstructure was evaluated independently and the findings indicated that the microstructure exhibits the lowest porosity level when the additional energy was limited within the range of 25 $J/mm^3$ to 45 $J/mm^3$, regardless of the sequence of the additional scan applied before or after the melting laser scan.

The results of this chapter indicate that the investigated innovative in-situ thermal process modifies the LPBF-fabricated Ti-6Al-4V microstructure and delivers very high mechanical strength with up to 85% yield strength (YS) compared to the reference condition without any additional laser scans. Furthermore, a slight decrease in elongation was observed, which is limited to 17% of the elongation at the reference condition. This limited reduction in elongation is uncommon compared to the existing strengthening

methods. The reported findings in material properties were achieved during the 3D fabrication process, and no additional post-processing is needed for the presented remarkable properties.

4.2 Experimental Methods and Fabrication

4.2.1 Materials and Fabrication

The metal powder used in this chapter was provided by EOS North America (Pflugerville, TX, USA). The powder material is fabricated by gas atomization to achieve the highest spheroidization quality. The composition of the materials has (%wt.) 5.50 - 6.75 Al, 3.50 - 4.50 V, 0.20 O, 0.05 N, 0.08 C, 0.015 H, 0.30 Fe, and the balance was Ti [33] and standardized as Ti-6Al-4V Grade 5.

A selective laser melting (SLM) 3D printer, EOS M290 (EOS GmbH, Electro Optical Systems, Krailling, Germany) equipped with Ytterbium fiber laser power of 400 W utilized for the fabrication of the samples. Suggested fabrication parameters by the manufacturer are 280 W laser power, 1300 mm/s scan speed, 120 μm hatch spacing, 100 μm laser spot size with a Gaussian distribution of energy, and 40 μm of layer thickness with 67° angle stripes scanning strategy (reference sample process parameters). Specimens were exposed to an initial preheating laser scan with varying laser power and laser scan speed. This was followed by the melting laser scan which was conducted under the manufacturer's recommended parameters. Finally, a post-heating laser scan was applied once more, with a variety of laser power and laser scan speeds. The illustrated laser scanning strategy sequence is presented in Figure 4.1. To quantize the effect of the applied preheating and post-heating scan along the melting laser scan, energy density was calculated from the equation reported by Thijs *et al.* (Eq 4.1) [34].

$$E_v = \frac{P}{v.h.t} \tag{4.1}$$
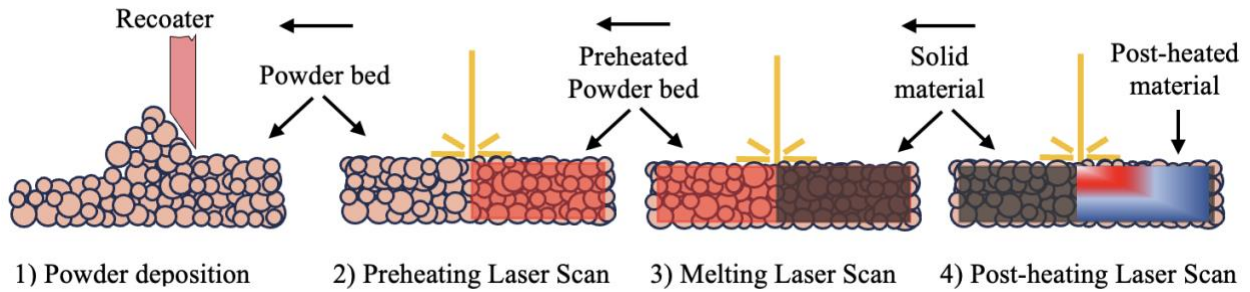
*Figure 4.1. Laser scanning strategy sequence: 1) Powder spreading from the dispenser onto the building plate, 2) Preheating the selective powder regions corresponding to the scanning pattern of the fabrication geometry, 3) Melting laser scan of the fabrication geometry, 4) Final, post-heating scan of the melted regions.*

4.2.2 Experimental Methods

Microstructure samples fabricated with the dimensions of 20 mm × 6 mm × 6 mm and test coupons for tensile testing fabricated in dog-bone geometry with the dimensions shown in Figure 4.2.
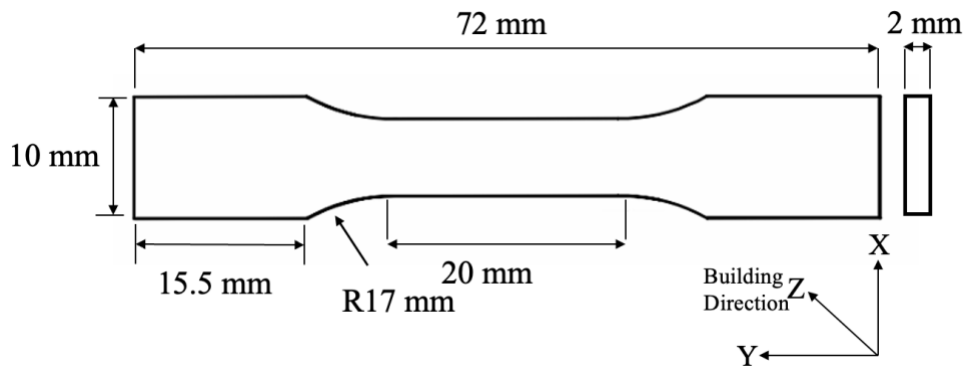


*Figure 4.2. Tensile testing sample*

Box – Behnken design of experiment (DOE) approach [35] performed with 4 factors and 3 levels for the possible process parameters for the fabrication. The findings of the previous study revealed that the best porosity values were obtained when the additional energy input was kept in the range of 25 J/mm$^3$ to 45 J/mm$^3$. The results of the Box–Behnken DOE show the fabrication scenarios including those with a higher total energy of 45 J/mm$^3$ which was set as the limit for the additional energy input. Table 4.1 provides a compilation of potential combinations of preheating and post-heating energy derived from the Box-Behnken design, with the total energy level within the range of 25 J/mm$^3$ to 45 J/mm$^3$.

67

Table 4.1 *various combinations of the process parameters for preheating and post-heating laser exposure delivered by DOE with energy input constraint (25 J/mm³ – 45 J/mm³)*

| # | Preheating Laser Speed (mm/s) | Preheating Laser Speed (mm/s) | E_preheating (J/mm3) | Post Heating Laser Power (W) | Post Heating Laser Speed (mm/s) | E_postheating (J/mm3) | E_total (J/mm3) |
|---|---|---|---|---|---|---|---|
| 1 | 196 | 1300 | 31.41 | 56 | 975 | 11.97 | 43.38 |
| 2 | 196 | 1300 | 31.41 | 56 | 1300 | 8.97 | 40.38 |
| 3 | 252 | 1625 | 32.31 | 56 | 975 | 11.97 | 44.27 |
| 4 | 252 | 1625 | 32.31 | 56 | 1300 | 8.97 | 41.28 |
| 5 | 196 | 1625 | 25.13 | 56 | 975 | 11.97 | 37.09 |
| 6 | 196 | 1625 | 25.13 | 98 | 1300 | 15.71 | 40.83 |
| 7 | 196 | 1625 | 25.13 | 56 | 650 | 17.95 | 43.08 |
| 8 | 224 | 1950 | 23.93 | 56 | 975 | 11.97 | 35.90 |
| 9 | 224 | 1950 | 23.93 | 98 | 975 | 20.94 | 44.87 |
| 10 | 224 | 1950 | 23.93 | 98 | 1300 | 15.71 | 39.64 |
| 11 | 224 | 1950 | 23.93 | 56 | 1300 | 8.97 | 32.91 |
| 12 | 224 | 1950 | 23.93 | 56 | 650 | 17.95 | 41.88 |
| 13 | 224 | 1625 | 28.72 | 56 | 975 | 11.97 | 40.68 |
| 14 | 224 | 1625 | 28.72 | 98 | 1300 | 15.71 | 44.42 |
| 15 | 224 | 1625 | 28.72 | 56 | 1300 | 8.97 | 37.69 |
| 16 | 224 | 1300 | 35.90 | 56 | 1300 | 8.97 | 44.87 |
| 17 | 252 | 1950 | 26.92 | 56 | 975 | 11.97 | 38.89 |
| 18 | 252 | 1950 | 26.92 | 98 | 1300 | 15.71 | 42.63 |
| 19 | 252 | 1950 | 26.92 | 56 | 650 | 17.95 | 44.87 |
| 20 | 252 | 1950 | 26.92 | 56 | 1300 | 8.97 | 35.90 |
| 21 | 224 | 1300 | 35.90 | 56 | 1300 | 8.97 | 44.87 |
| 22 | 196 | 1950 | 20.94 | 98 | 1300 | 15.71 | 36.65 |
| 23 | 196 | 1950 | 20.94 | 56 | 1300 | 8.97 | 29.91 |
| 24 | 196 | 1950 | 20.94 | 56 | 650 | 17.95 | 38.89 |
| 25 | 196 | 1950 | 20.94 | 56 | 975 | 11.97 | 32.91 |
| 26 | 224 | 1950 | 23.93 | 56 | 975 | 11.97 | 35.90 |
| 27 | 196 | 1950 | 20.94 | 98 | 975 | 20.94 | 41.88 |

## 4.2.3 Microstructure Characterization

Scanning Electron Microscopy (SEM) was performed for porosity, α-phase lath width, and grain morphology caused by various energy inputs during the in-situ thermal process. Microstructure imaging samples were cut out by a TECHCUT 5™ precision cutter (Allied High-Tech Products, Inc., Rancho

Dominguez, CA, USA) from the center of the fabricated specimen along the building plane. Samples were cold mounted for the sample holder of the automated polishing equipment (E-PREP Grinding / Polishing System, Allied High-Tech Products, Inc., Rancho Dominguez, CA, USA) Sample preparation for the metallography started with the grinding from 320 to 1200 grit size of SiC sandpaper. It was followed by, the first step of polishing was performed on a DiaMat ® polishing cloth with 1 μm diamond suspension. The final step of the polishing was performed with 0.04 μm colloidal silica suspension on Red Final C ® polishing pad used to obtain scratch-free, mirror-like finish sample surfaces. Polished samples were rinsed in micro-organic soap and cleaned with isopropyl alcohol. Samples were etched with Kroll's reagent (1–3 mL HF, 2–6 mL $HNO_3$, 100 mL water) to identify the grain boundaries and phases of the microstructure.

The porosity level of each microstructure sample was assessed by utilizing the image processing software. Image J [36], was used to calculate the porosity level. The porosity distribution was determined from at least three different regions at 2 magnification levels (500x and 1000x). Image J was also used for the lath width calculation of the α-phase. For lath thickness measurement, microstructure images were first converted to RGB stack-type grayscale images before setting the auto contrast level. Thresholding was applied to improve the contrast of α/α′ phase laths borders. Particle sizes within the range of 0.2 μm to 2.0 μm were analyzed, and the total counts for each size were computed to obtain the average value. This was performed on a minimum of 6 different images to obtain statistically reliable data for each sample.

X-ray diffraction (XRD) analyses were conducted for further microstructural characterization, to calculate lattice parameters, and to determine microstructure orientations for each sample. A Bruker D8 Advance X-ray diffractometer (Bruker Corporation, Madison, WI, USA) was utilized for the X-ray diffraction with a Cu k-alpha wavelength of 1.5406 Å, operating at 40 mA current and 40 kV voltage at room temperature. Measurements were taken with step intervals of 0.05° and a scan speed of 1 sec/step, while 2θ ranged from 20° to 80°.

Lattice parameters were computed following Bragg's law (Eq (2)), where d represents inter-planar spacing, and a and c denote the lattice parameters. The variables h, k, and l refer to the Miller indices.

$$\frac{1}{d^2} = \frac{4}{3}\left(\frac{h^2 + hk + k^2}{a^2}\right) + \frac{l^2}{c^2}$$  (4.2)

$$\lambda = 2d \sin\theta$$

XRD data was analyzed with the Williamson-Hall (W-H) model [37] to obtain the microstrain value of the reference and the in-situ thermal processed samples. The W-H model. The XRD data was utilized in the following equations (Eq (3) (4) (5)). The XRD pattern's peak broadening results from crystal imperfections and distortion, as expressed by $\varepsilon \approx \beta_s / \tan\theta$. The plot of the W–H model was used for the calculation of the microstrain value. Si standard reflection (0.0013 rad) [38] was subtracted before strain analysis using W–H method. The Scherrer's equation expressed as Eq. (4.3) and further derived to Eq. (4.5) where $\beta$ is peak broadening, $\lambda$ is the wavelength (Å). K is the Cu $K_s$ (0.94), D is the crystallite size (nm) and $\theta$ is the peak position.

$$D = \frac{\lambda K}{\beta \cos\theta}$$  (4.3)

$$\beta = \sqrt{\beta_T{}^2 - \beta_i{}^2}$$  (4.4)

$$\beta \cos\theta = \frac{\lambda K}{D} + 4\varepsilon \sin\theta$$  (4.5)

4.2.4 Mechanical Testing

Mechanical testing was performed using a Shimadzu EHF E-Series (100 kN) testing machine equipped with a 4830 Servo Controller (Shimadzu Scientific Instruments, Inc., Missouri City, TX, USA). For accurate strain measurements in the gauge section, a digital image correlation (DIC) system (Correlated Solutions, Inc., Irmo, SC, USA) was employed. The system tracked light-intensity patterns of high-contrast speckles on the coupon surface to measure the surface displacements and strain. Image capturing utilized a CCD camera with 2.3 Mega Pixels each, specifically a Grasshopper GS3-U3-23S6M (FLIR Systems, Inc., Santa Barbara, CA, USA), featuring a pixel array of 1920 x 1200. Image and data processing were carried out using VIC-3D® software (Correlated Solutions, Inc., Irmo, SC, USA). All samples underwent testing at a constant loading rate of 1.2 mm/min, following the recommended testing standard for LPBF-fabricated Ti-6Al-4V tensile samples as outlined in the literature [39].

4.3 Results

4.3.1 Microstructure Defects and Grain Structure

SEM microstructure images of the reference sample and one of the in-situ thermally processed samples (196W preheating laser scan power, 1950 mm/s preheating laser scan speed + 56W post-heating laser scan power, 1300 mm/s post-heating laser scan speed) depicted in Figure 4.2. In Figure 4.2 (a) the internal defects of the reference sample were marked with black arrows. Figure 4.2 (b) shows the obvious effect of the in-situ thermal processing on the inherent process-induced defects of the LPBF-fabricated Ti-6Al-V. Nevertheless, while defects are easily discernible in the reference sample micrograph, no distinct defects were observed in the in-situ thermally processed sample. To avoid any potential confusion in the further sections of this paper, it is better to clarify that all volumetric defects identified through the SEM micrography are counted and termed as porosity and are included during the defect calculations regardless of the shape and size of the discontinuity.
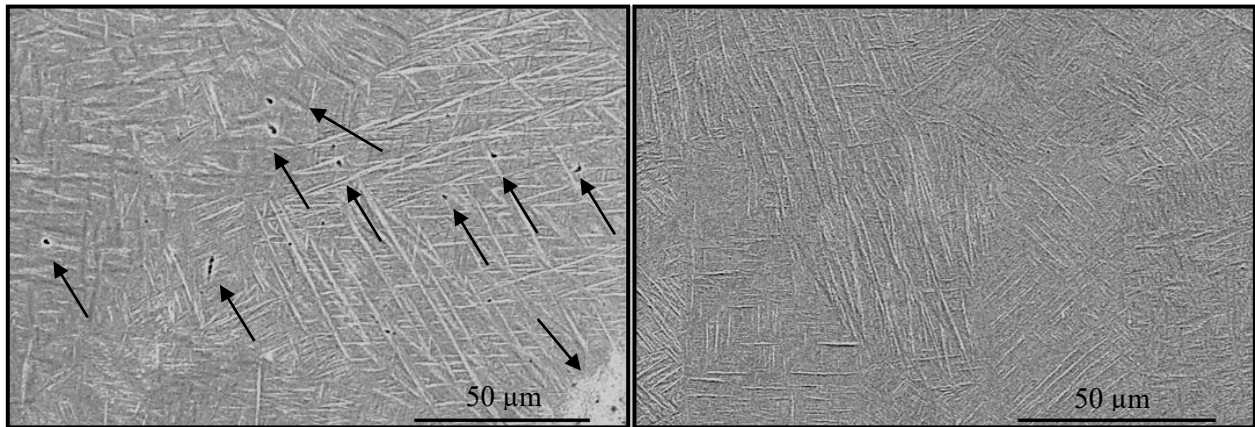


*Figure 4.3. SEM images of (a) the reference sample without any additional laser scan and (b) the in-situ thermal process sample (196W preheating laser scan power, 1950 mm/s preheating laser scan speed + 56W post-heating laser scan power, 1300 mm/s post-heating laser scan speed)*

Porosity levels for the preheating laser scan and post-heating laser scan applications were assessed by SEM micrographs. Figure 4.4. (a) and (b) show the porosity level of the preheating and post-heating

applications respectively. It was observed that in both applications the lowest porosity level was achieved in the energy density range of 25 J/mm$^3$ to 45 J/mm$^3$.
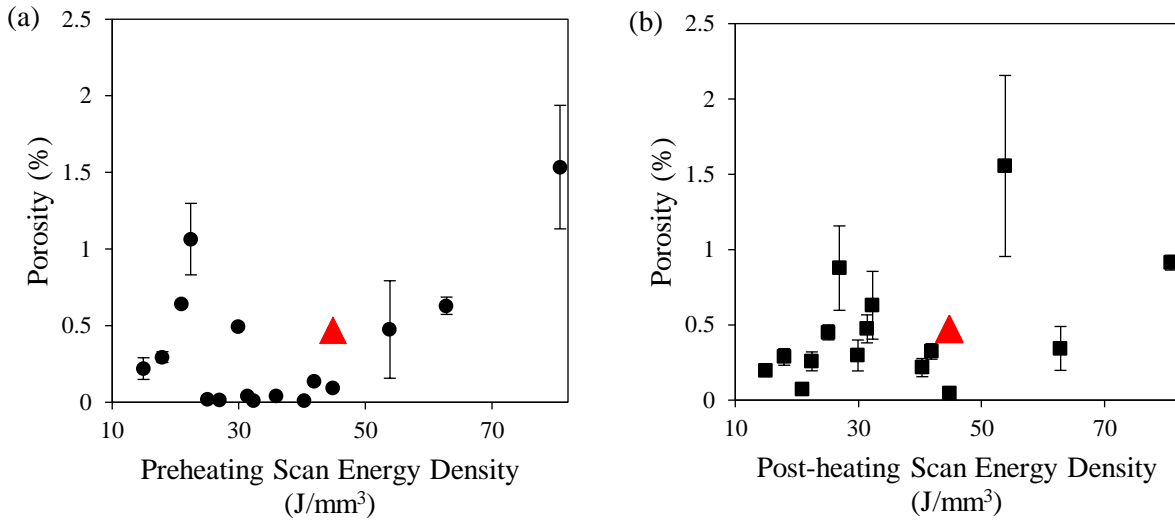


*Figure 4.4. (a) Influence of the applied single preheating laser scan energy density on porosity. (b) Impact of the applied single post-heating laser scan energy density on porosity. The porosity level of the reference sample without any additional laser scan is depicted with a red triangle marker in both figures.*

The SEM images of both applications reveal a significant reduction in the porosity amount when the introduced energy amount was kept between 25 J/mm$^3$ to 45 J/mm$^3$. In the presented in-situ thermal process, which involves the combination of preheating and post-heating laser scans, the total energy level was maintained within this range. The Box – Behnken DOE parameters are listed in Table 4.2 for the selected preheating and post-heating laser scan parameters. The potential combinations of process parameters were analyzed, and parameter sets falling outside of this energy range were eliminated. All process parameters set combinations with a total energy input between 25 J/mm$^3$ to 45 J/mm$^3$ were derived from the remaining dataset for the fabrication process and are listed in Table 4.1.

Microstructure coupons were fabricated for each parameter set listed in Table 4.1 and the porosity levels of the microstructure for each case are listed in Table 4.2.

*Table 4.2 Porosity in As-Fabricated Parts by Laser Parameters. Compares porosity levels for each combination of preheating and post-heating laser settings.*

| # | Preheating Laser Power (W) | Preheating Laser Speed (mm/s) | Post-heating Laser Power (W) | Post-heating Laser Speed (mm/s) | AVE (%) | STD (%) |
|---|---|---|---|---|---|---|
| 1 | 196 | 1300 | 56 | 975 | 0.06 | 0.04 |
| 2 | 196 | 1300 | 56 | 1300 | 0.07 | 0.07 |
| 3 | 252 | 1625 | 56 | 975 | 0.02 | 0.01 |
| 4 | 252 | 1625 | 56 | 1300 | 0.52 | 0.84 |
| 5 | 196 | 1625 | 56 | 975 | 0.10 | 0.07 |
| 6 | 196 | 1625 | 98 | 1300 | 0.14 | 0.12 |
| 7 | 196 | 1625 | 56 | 650 | 0.19 | 0.15 |
| 8 | 224 | 1950 | 56 | 975 | 0.38 | 0.27 |
| 9 | 224 | 1950 | 98 | 975 | 0.06 | 0.03 |
| 10 | 224 | 1950 | 98 | 1300 | 0.02 | 0.01 |
| 11 | 224 | 1950 | 56 | 1300 | 0.38 | 0.71 |
| 12 | 224 | 1950 | 56 | 650 | 0.10 | 0.07 |
| 13 | 224 | 1625 | 56 | 975 | 0.04 | 0.02 |
| 14 | 224 | 1625 | 98 | 1300 | 0.12 | 0.12 |
| 15 | 224 | 1625 | 56 | 1300 | 0.10 | 0.08 |
| 16 | 224 | 1300 | 56 | 1300 | 0.07 | 0.06 |
| 17 | 252 | 1950 | 56 | 975 | 0.06 | 0.02 |
| 18 | 252 | 1950 | 98 | 1300 | 0.14 | 0.25 |
| 19 | 252 | 1950 | 56 | 650 | 0.01 | 0.01 |
| 20 | 252 | 1950 | 56 | 1300 | 0.11 | 0.10 |
| 21 | 224 | 1300 | 56 | 1300 | 0.08 | 0.06 |
| 22 | 196 | 1950 | 98 | 1300 | 0.14 | 0.24 |
| 23 | 196 | 1950 | 56 | 1300 | 0.01 | 0.01 |
| 24 | 196 | 1950 | 56 | 650 | 0.07 | 0.05 |
| 25 | 196 | 1950 | 56 | 975 | 0.06 | 0.04 |
| 26 | 224 | 1950 | 56 | 975 | 0.03 | 0.03 |
| 27 | 196 | 1950 | 98 | 975 | 0.04 | 0.02 |

Figure 4.5 illustrates how the porosity value responds to variations in the applied preheating laser scan parameters during the in-situ thermal processing of the LPBF-fabricated Ti-6Al4V. A notable decrease in porosity was observed at lower energy levels of the preheating laser scan when combined with each post-heating laser scan. Specifically, preheating laser scan speeds below 1000 mm/s and laser power less than 180 W led to higher porosity levels when they were coupled with the post-heating laser scan. It was noted that samples incorporating post-heating at a laser power of 56 W and 1300 mm/s exhibited increased sensitivity to porosity formation. The samples subjected to post-heating with a laser scan power of 56 W

and a scan speed of 650 mm/s exhibit the least variation in porosity depending on the preheating process parameters.

The reference coupon did not undergo any preheating or post-heating and exhibited an average porosity of 0.47% ± 0.015%. It is noteworthy that the porosity level was reduced to 0.01% ± 0.01% with the applied in-situ thermal process presented in this chapter. The combination of preheating and post-heating laser scans achieved the four lowest porosity levels were selected for further microstructural characterization and mechanical testing for the following sections of this chapter. These parameter combinations are listed in Table 4.2, under row numbers 3, 10, 19, and 23.
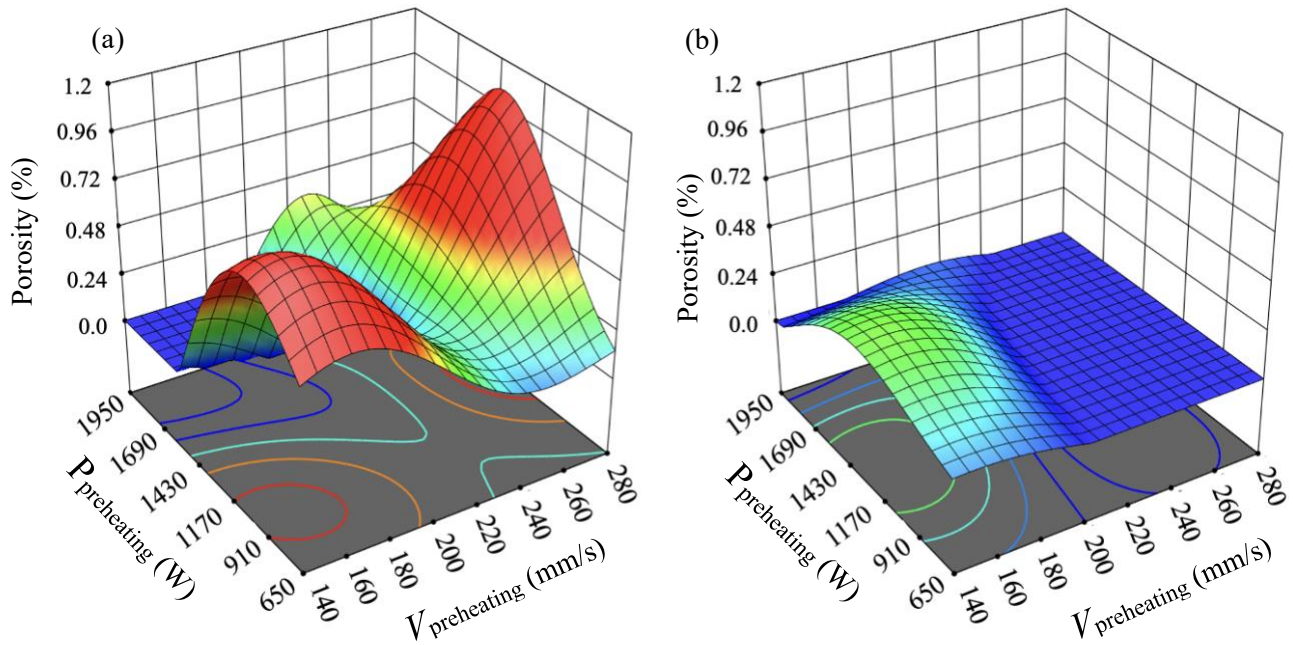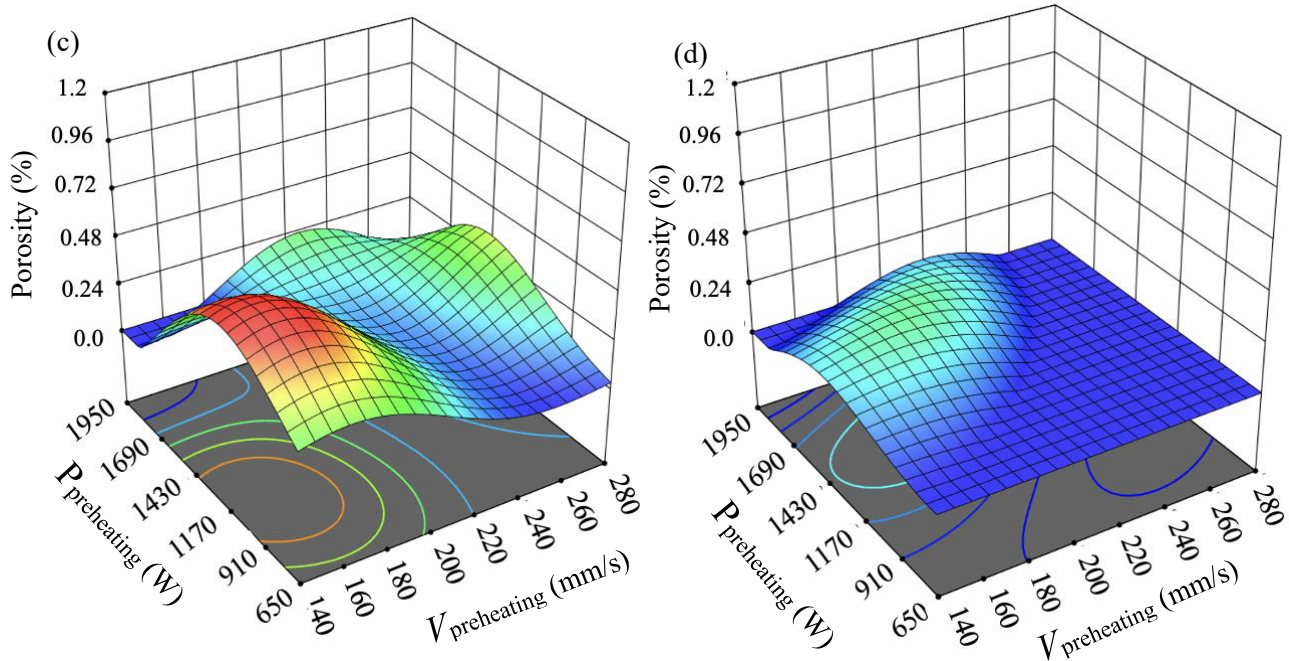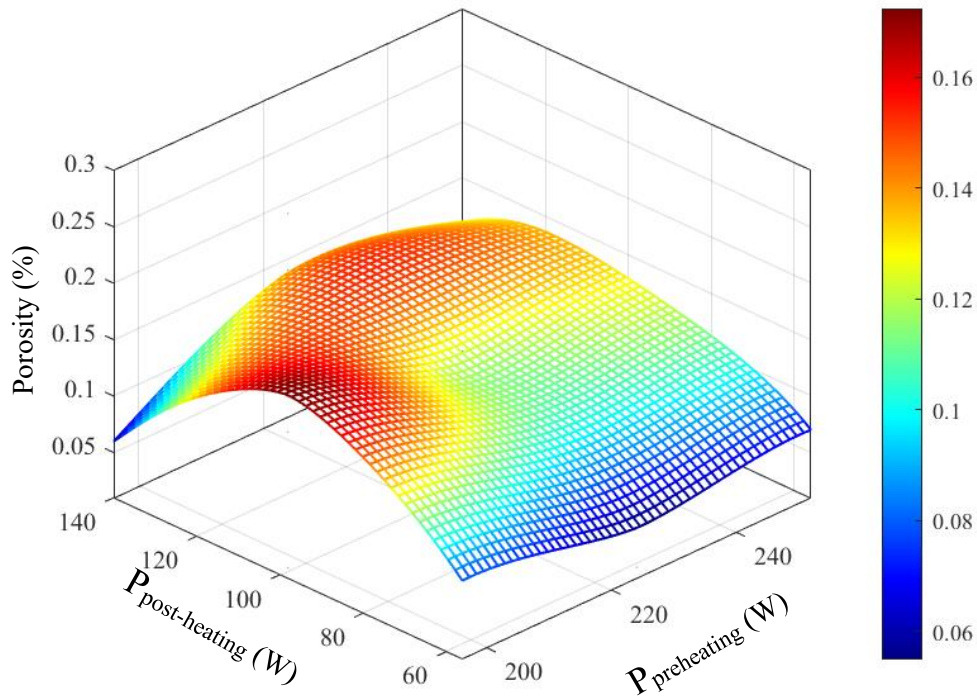
*Figure 4.5. Response surface plots of the impact of the in-situ thermal processing through the combination of preheating and post-heating laser scan, on porosity. (a) Effect of the preheating laser scan parameters at constant post-heating laser parameters of 56 W laser power and 1300 mm/s laser scan speed which include case 23. (b) Preheating laser scan parameters impact at constant post-heating laser parameters of 56 W laser power and 975 mm/s laser scan speed which include case 3. (c) Preheating laser scan parameters impact constant post-heating laser parameters of 98 W laser power and 1300 mm/s*

Examination of the microstructure through SEM micrography revealed that LPBF-fabricated Ti-6Al-4V possessed lamellar microstructure that lath colonies correspond to either the α or α′ phase [40]. The lath thickness (in some studies it is referred to as lath width) of the basketweave-like structure determines the mechanical response of the material [41]. The lath thickness of the samples that were exposed to the in-situ thermal process and the reference sample (no thermal processing) is presented in Figure 4.6 using image processing techniques on SEM micrographs via ImageJ software.

In the reference sample with the energy input of 44.87 J/mm$^3$, the α/α' laths thickness was measured to be 0.797 ± 0.005 μm. It is illustrated in Figure 4.6 using a red marker. Similar to the reference sample the in-situ thermally processed samples exhibited α/α' laths thickness ranging from 0.792 μm to 0.812 μm at the total energy inputs between 74.79 J/mm$^3$ to 89.74 J/mm$^3$.
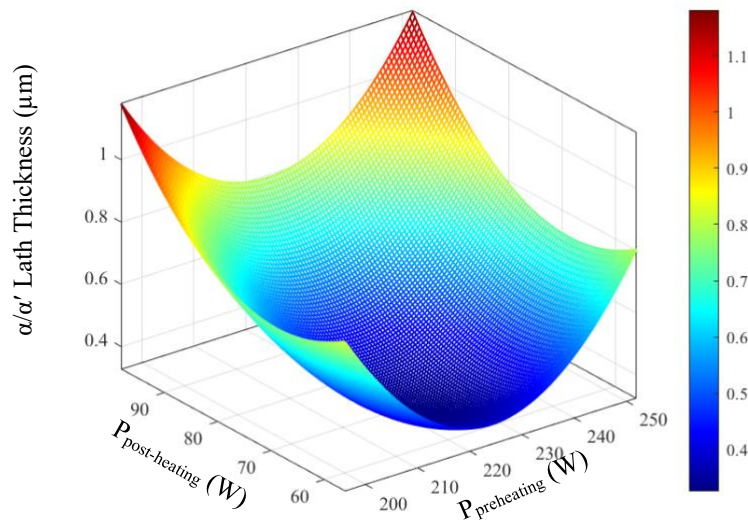


*Figure 4.6. Response surface plots of the impact of the in-situ thermal processing through the combination of preheating and post-heating laser scan, on α/α' phase lath thickness. Lower post-heating laser power combined with moderate preheating laser scan powers delivered lower lath thickness.*

4.3.2 Lattice Transformation, and Phase Decomposition in Preheated LPBF Ti-6Al-4V

4.3.2.1 Crystallography through XRD Analysis

Figure 4.7 shows the XRD profiles of the reference and in-situ thermally processed samples, arranged in ascending order of total energy inputs. The highest intensity of Bragg's peak was observed at the (101) plane for the reference sample. In parallel, in-situ thermally processed samples have similar peak patterns, it is noteworthy that the strongest peak intensity was observed at the (101) plane. The XRD diffraction pattern data quantized by utilizing the Bragg's and the W-H model for further evaluation in the following sections.
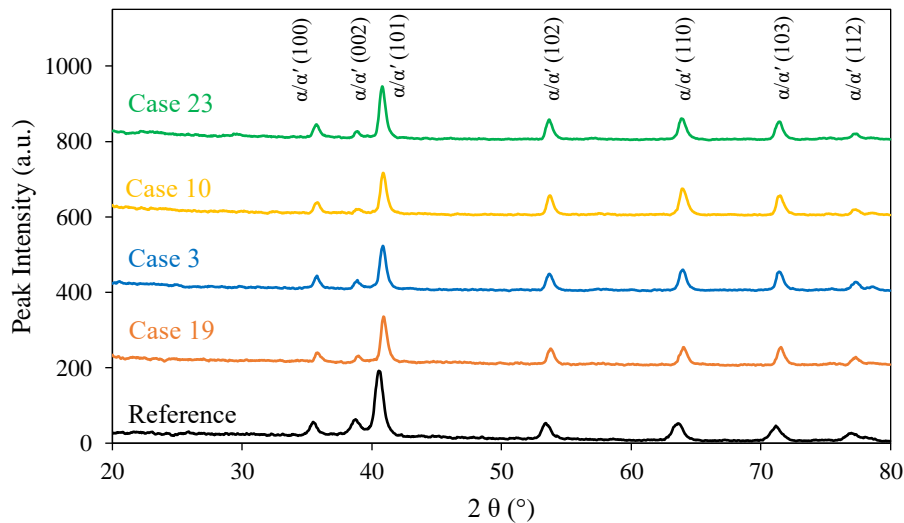


*Figure 4.7. The XRD you patterns of the reference (without additional laser scan) and the in-situ thermally processed samples including, case 3 (preheating: P=252W, V=1625 mm/s, post-heating: 56W, V=975 mm/s), case 10 (preheating: P=224W, V=1950 mm/s, post-heating: 98W, V=650 mm/s) case 19 (preheating: P=252W, V=1950 mm/s, post-heating: 56W, V=650 mm/s), case 23 (preheating: P=196W, V=1950 mm/s, post-heating: 56W, V=1300 mm/s)*

The W-H model was performed to determine the impact of the in-situ thermal process on the microstrain values for the selected cases that delivered the lowest porosity levels. The W-H model for the reference sample and the in-situ thermally processed samples are illustrated in Figure 4.8. When the W-H equation (Eq. 4.5) is viewed as a linear equation in the form of y = mx + c, then the slope of the equation corresponds to the strain value. The reference sample exhibits a positive slope. It is noteworthy that utilizing the in-situ thermal processing transformed the slope from positive to negative except one in-situ thermal

process condition (Figure 4.8). However, the in-situ thermal processing with the parameters of 252 W preheating laser scan power, 1950 mm/s preheating laser scan speed and 56 W post-heating laser scan power, 650mm/s post-heating laser scan speed (Figure 4.8 (c)) exhibits a different trend in which the slope is positive but the value is smaller than the reference microstructure. The transformation of the slope from a positive vale to negative value shows that the microstrain value shifted from tension mode to compression mode. Additionally, the change of the slope to a smaller positive value shows the decrease of the strain in the tension mode.
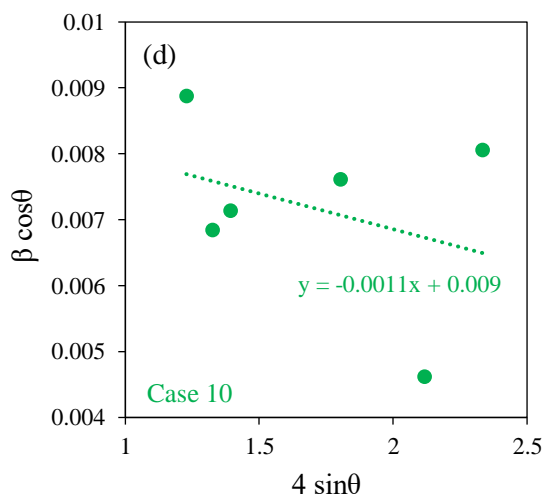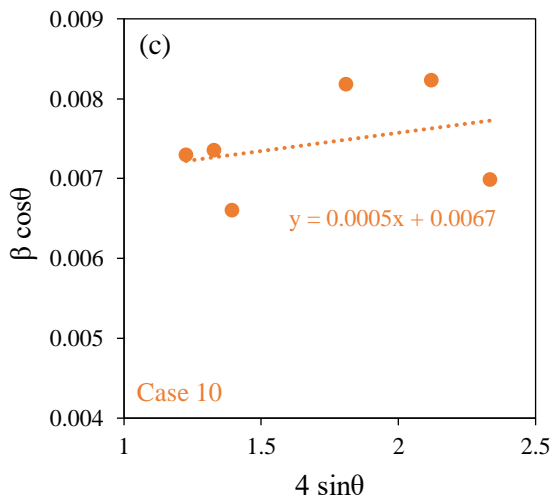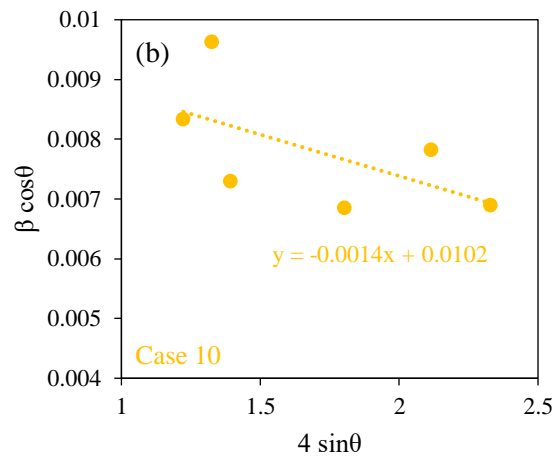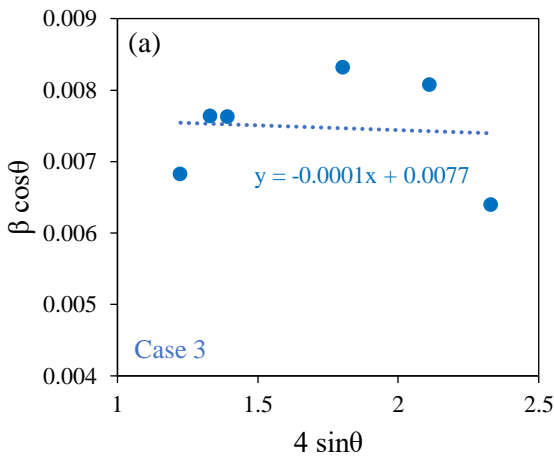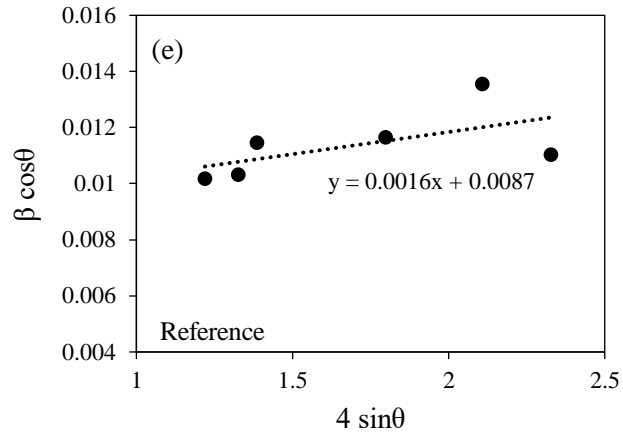
*Figure 4.8. The microstrain values were derived from the slope of the fitted linear trendline in the W-H analysis for different in-situ thermal processing conditions. (a) Case 3 (preheating: P=252W, V=1625 mm/s, post-heating: 56W, V=975 mm/s), (b) case 10 (preheating: P=224W, V=1950 mm/s, post-heating: 98W, V=650 mm/s), (c) Case 19 (preheating: P=252W, V=1950 mm/s, post-heating: 56W, V=650 mm/s), (d) Case 23 (preheating: P=196W, V=1950 mm/s, post-heating: 56W, V=1300 mm/s), (e) Reference sample without any additional laser scan application*

### 4.3.2.2 HCP Lattice Modification

The XRD data utilized in Bragg's model (Eq. 4.2) for additional microstructure characterization, particularly focusing on lattice deformation in the material [14]. As per the model, Figure 4.9 depicts the lattice parameters of the HCP phase, which is the prevailing stable phase indicated by the XRD data [42] with additional energy to the system, a reduction of 1.1% and 0.3% in both lattice parameters of a and c was observed, respectively(Figure 4.9 (a) and (b)). Furthermore, lattice strain was observed with the applied in-situ thermal process (Figure 4.9 (c)). The lattice strain was shown with a higher c/a ratio. The in-situ thermally processed samples exhibit lower 'a' and 'c' lattice parameters. However, the ratio of the parameters in the modified microstructure indicates a higher strain value.
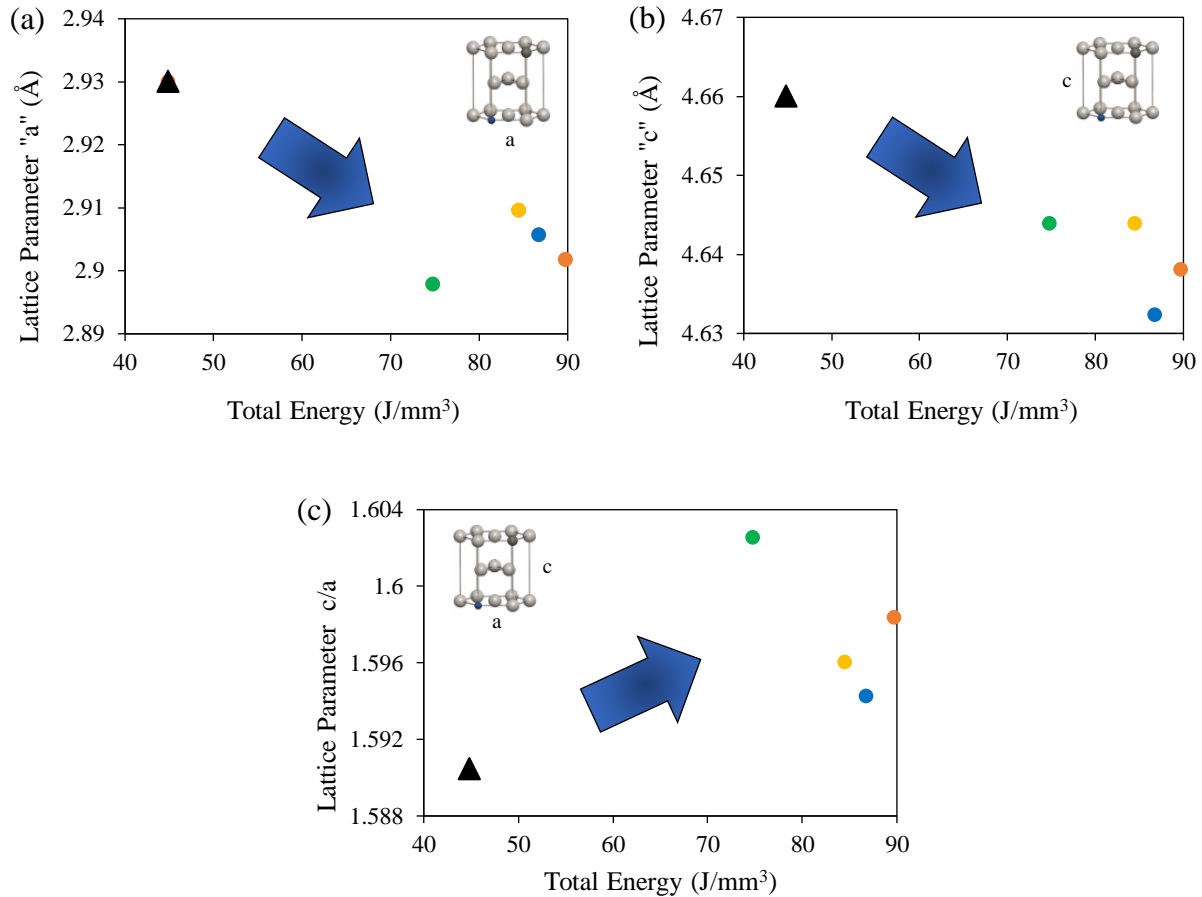
*Figure 4.9. Effect of the in-situ thermal processing on HCP lattice parameters. (a) The total energy of the preheating and post-heating laser scans effect on lattice parameter "a". (b) lattice parameter "c". (c) Lattice distortion variation at different total energy inputs.*

4.3.3 Mechanical Properties

The mechanical behavior of the modified microstructure with the in-situ thermal process was quantized through the tensile test. The stress-strain plot is depicted in Figure 4.10. It is evident that the application of the in-situ thermal process had a noticeable effect on the material's strength. It was observed both the UTS and the YS values were enhanced. A remarkable increase in the slope during elastic deformation achieved a higher YS for each in-situ thermally processed sample. The improvements in the YS for the four selected in-situ thermal process conditions were 53.5%, 61.8%, 34.2%, and 85.1% for sample numbers 3, 10, 19, and 23 respectively, as listed in Table 4.1. The process parameters of case 23 (preheated with196 W laser power,1950 mm/s laser scan speed, and post heated with 56 W laser power, and

650 mm/s laser scan speed) exhibit the highest UTS (1843.6 MPa) and YS (1394.8 MPa) which is about 85% and 55% improvement relatively compared to the reference case. The lowest improvement in the material's strength was observed in case 19 with the in-situ thermal process conditions of 252 W preheating laser power, 1950 mm/s preheating laser scan speed, 56 W post-heating laser power, and 650 mm/s post-heating laser scan speed. The measured UTS and YS were 1284.3 MPa and 1011.2 MPa, with an improvement of 34% and 8%, respectively.
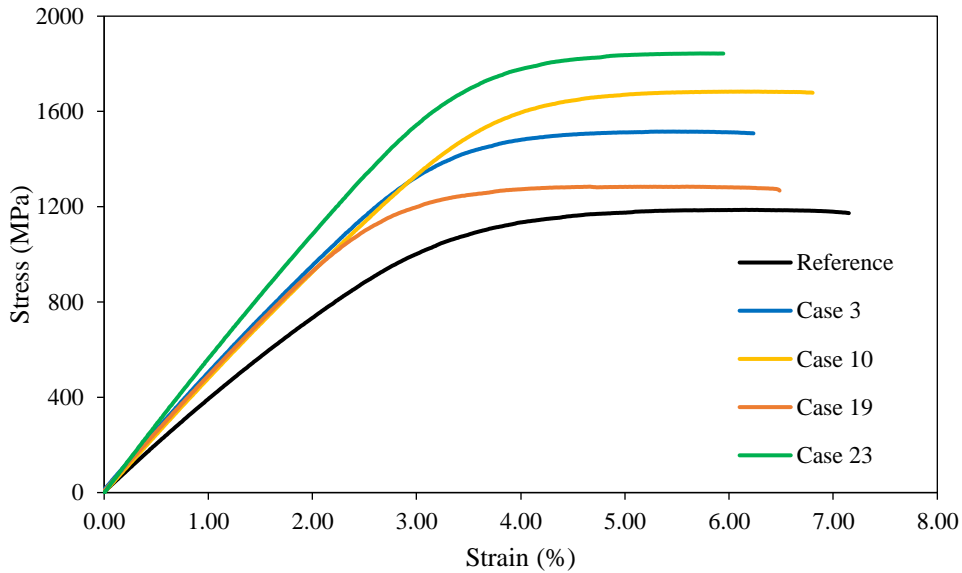


*Figure 4.10. Stress-strain plot of the reference (without additional laser scan) and the in-situ thermally processed samples including case 3 (preheating: P=252W, V=1625 mm/s, post-heating: 56W, V=975 mm/s); case 10 (preheating: P=224W, V=1950 mm/s, post-heating: 98W, V=650 mm/s); case 19 (preheating: P=252W, V=1950 mm/s, post-heating: 56W, V=650 mm/s); case 23 (preheating: P=196W, V=1950 mm/s, post-heating: 56W, V=1300 mm/s)*

Localized strain right before the rapture for the reference and the in-situ thermally processed samples are depicted in Figure 4.11. It was observed that the reference sample (Figure 4.11) has the highest deformation amount and the largest deformed region compared to the in-situ thermal processed samples. Among the in-situ thermal applications it is noteworthy that case 23 has the lowest deformation region cyan regions)
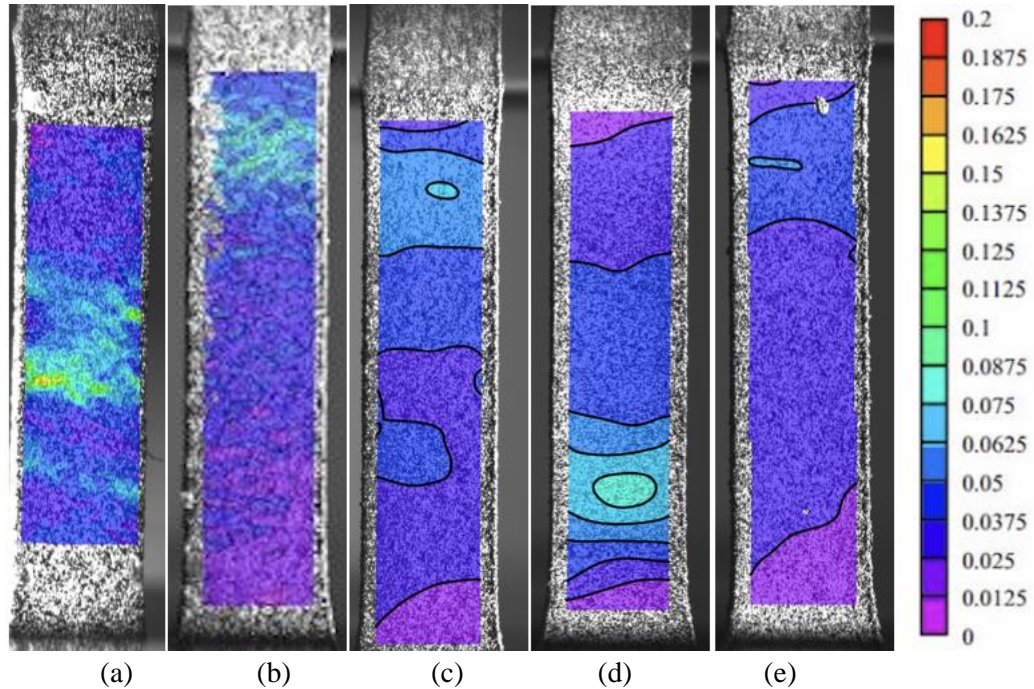
*Figure 4.11. Localized strain contour maps of $\varepsilon_{yy}$ from the DIC image analysis. (a) reference sample (without additional laser scan), (b) Case 3 (preheating: P=252W, V=1625 mm/s, post-heating: 56W, V=975 mm/s), (c) Case 10 (preheating: P=224W, V=1950 mm/s, post-heating: 98W, V=1300 mm/s, (d) Case 19 (preheating: P=252W, V=1950 mm/s, post-heating: 56W, V=650 mm/s), (e) Case 23( preheating: P=190W, V=1950 mm/s, post-heating: 98W, V=650 mm/s)*

## 4.4 Discussions

In the present chapter, an in-situ thermal process during the LPBF fabrication of Ti-6Al-4V was investigated. A preheating laser scan application, which is discussed in detail in the previous chapter, combined with a third laser scan strategy termed post-heating laser scan. The presented innovative in-situ thermal processing of the LPBF-fabricated Ti-6Al-4V modified the material's microstructure. It is noteworthy that in-situ thermal processing led to a significant reduction in the process-induced porosity level of the microstructure. Almost 98% improvement was observed by performing the in-situ thermal process at the porosity level. This improvement can be considered as a result of partial melting during the preheating laser scan and re-melting with the complementary post-heating laser scan. Low energy inputs cause partial melting [43] at this point the applied preheating can be considered the low energy input that powder particles partially melted at the particle connection regions, a sinter-like effect occurred. This led to larger particles with irregular geometries in the powder bed which impedes the powder particle spattering

82

during the melting. Spattering due to the high-speed laser and loose powder interactions is one of the reasons for the inherent porosity [44] in LPBF technology.  Similar improvements were observed in the literature and achieved by the re-melting effect [14,26,45]. Post-heating laser scan in the in-situ thermal process can be considered as the remelting effect. However, the post-heating laser scan has a lower energy value than the melting scan, the material has elevated temperatures in which even lower energy inputs might exceed the melting temperature of the material. Furthermore, Figure 4.5 (e) illustrates that elevated post-heating laser power corresponds to a relatively higher level of porosity, attributed to increased evaporation under higher post-heating energy.  Furthermore, it is reported that the complementary post-process of HIP [16,46] reduces the porosity level drastically. In the presented study a robust control of the multi-scan laser scan promises precise final microstructure adjustments rather than the existing literature which is limited to the multi-scan laser application of the single laser parameters to obtain the remelting effect. Furthermore, in the presented study improvement in the inherent porosity level was achieved without the necessity of costly and time-consuming additional processes such as HIP.

Additionally, the applied energy transformed the lath structure of the $\alpha/\alpha'$ phases which ultimately dictates the mechanical response of the LPBF-fabricated Ti-6Al-4V. The microstructure of LPBF-fabricated Ti-6Al-4V primarily consisted of $\alpha$ and $\alpha'$ phases. In the present chapter, both phases were referred to as the structure of $\alpha/\alpha'$ phases, in consideration of the complexity of the microstructure and the common literature practice. The mechanical response of the microstructure is a result of these $\alpha/\alpha'$ phases' structures [47]. The main structural feature of these phases that defines the mechanical property of the material is the lath thickness. Figure 4.6 demonstrates the variation of the $\alpha/\alpha'$ phase lath thickness in relation to the total energy input during the fabrication process. The measured lath thickness values in Figure 4.6 make it challenging to establish a clear trend relation between the $\alpha/\alpha'$ lath thickness and the total energy input during the in-situ thermal process of LPBF-fabricated Ti-6Al-4V.

Moreover, XRD analysis pronounced a transformation in the peak pattern of the material. Microstructure characterization was performed through XRD analysis to provide detailed insights into the impact of the in-situ thermal processing on LPBF-fabricated microstructure, specifically on the material's lattice

structure. Figure 4.7 exhibits the peak patterns of the reference sample without additional laser scan and the selected in-situ thermally processed samples. A noteworthy change in the peak pattern was observed with the application of the in-situ thermal process. The highest peak intensity was observed at the (101) plane at the reference condition and it was shifted to the (002) plane with the application of the in-situ thermal processing. Moreover, a reduction in the disparity between the peak intensity values was observed. This can be considered as an improvement in the isotropy of grain orientation within the microstructure, which is associated with the cooling rates and the inherent directional cooling behavior of the process. Introducing additional energy during the in-situ thermal processing changed the cooling rate of the material which turned out a transformation in the peak patterns. Additional introduced energy increased the total energy input which decreased the cooling rate. This observation is in parallel with the previous studies that reported the XRD diffraction patterns of the conventionally fabricated Ti-6Al-4V with slower cooling rates [48,49]. The change in the grain orientation will transform the deformation behavior of the material under tension loadings. Deformation is driven by the grain boundary network during the elastic region [50] and when it exceeds to plastic region it is driven by the active slip systems of the microstructure [51]. Change in the grain orientation highly affects the deformation mechanism in the elastic region as discussed in the subsequent paragraphs in this section.

XRD diffraction patterns were also employed to calculate the lattice parameters by Bragg's law. Figure 4.9 illustrates the lattice parameters of the reference sample and in-situ thermally processed samples. Figure 4.9 (a) and (b) pronounced a noteworthy reduction in both lattice parameters of 'a' and 'c' after the application of the additional energy compared to the reference sample. The HCP lattice parameters changed from the initial condition, and a notable strain was observed. The strained HCP lattice structure of the in-situ thermal process is shown in Figure 4.9 (c). The observed lattice strain due to the additional heat input to the powder with a preheating laser scan is in parallel with the previous chapter and study. The lattice distortion is recognized to have a direct influence on the dislocation density and mobility, ultimately impacting the mechanical strength of the material [52]. The lattice deformation of the Ti-6Al-4V material can be rationalized with the super-saturated lattice with substitutional V atoms and interstitial O atoms.

Additional energy during the in-situ thermal process modified the rapid cooling rates of the LPBF process. It is noteworthy that the lowest additional energy during the in-situ thermal process, case 23, exhibits the highest lattice distortion among all in-situ thermal process cases. The lower heat input is considered as the faster cooling rate which rationalizes smaller HCP lattices with limited vanadium diffusion. Vanadium atoms occupied the titanium atom positions with smaller radii. The lattice strain along the c-axis can be rationalized with the oxygen entrapment of the Ti-6Al-4V material at elevated temperatures. However, the material fabricated under shield gas of argon, there remains a limited amount of oxygen in the chamber, reaching up to 0.2%. Titanium is known for its high affinity to oxygen among metallic materials [53] which makes the material sensitive at elevated temperatures even at very low oxygen concentrations. Schematic of the lattice transformation is depicted in Figure 4.12.



| Lattice of the Ti-6Al-4V powder | Interstitial Oxygen atoms entrapped in the Ti-6Al-4V lattice. | Oxygen atoms at the octahedral positions |

○ Titanium　　● Vanadium　　● Aluminum　　○ Oxygen
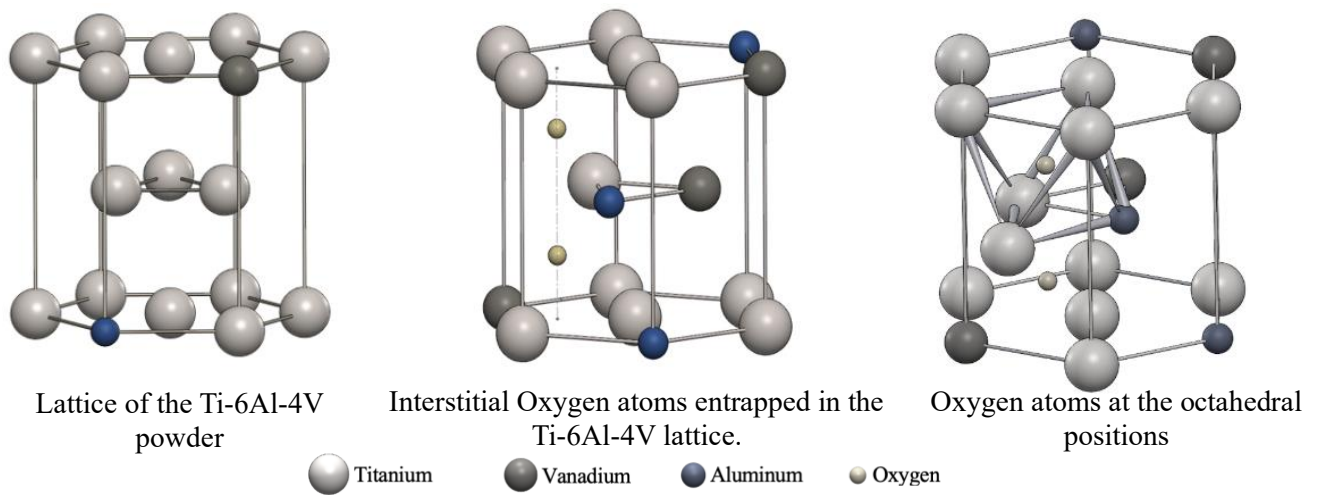
*Figure 4.12. Lattice deformation with the additional interstitial oxygen atoms in the octahedral positions during in-situ thermal processing of the LPBF-fabricated Ti-6Al-4V*

Mechanical testing was performed to evaluate the response of the modified microstructure by the in-situ thermal process suggested in the presented chapter. A remarkable improvement in the strength value was observed with the application of the preheating and post-heating laser scans. It is demonstrated in Figure 4.10 how the in-situ thermal process enhances the materials strength of LPBF-fabricated Ti-6Al-4V. The most significant enhancement in the strength was noticed at the in-situ thermal process parameters of

case 23(196 W preheating laser power, 1950 mm/s preheating laser scan speed, 56 W post-heating laser power, and 1300 mm/s post-heating laser scan speed (illustrated by the green line in Figure 4.10)). This fabrication case had the lowest energy input among the other in-situ thermally processed samples. This remarkable improvement was attributed to the modified microstructure which exhibited one of the lowest porosity values (Figure 4.2 & Figure 4.5 (d)) and the highest lattice strain value (Figure 4.9 (c)). It is rational to obtain a reduction in elongation following the material's strengthening [54]. The presented in-situ thermal process exhibits very high strength values with a very limited reduction in the elongation value of the material. The results of the presented study demonstrate that the innovative in-situ thermal process applied to LPBF-fabricated Ti-6Al-4V enhances the strength by up to 85% while limiting the reduction of the elongation which is a result of the strengthening mechanism of the materials.

## 4.5 References

1. Liu, S.; Shin, Y.C. Additive Manufacturing of Ti6Al4V Alloy: A Review. *Mater Des* **2019**, *164*, 107552, doi:https://doi.org/10.1016/j.matdes.2018.107552.
2. Tshephe, T.S.; Akinwamide, S.O.; Olevsky, E.; Olubambi, P.A. Additive Manufacturing of Titanium-Based Alloys- A Review of Methods, Properties, Challenges, and Prospects. *Heliyon* **2022**, *8*, e09041, doi:https://doi.org/10.1016/j.heliyon.2022.e09041.
3. Ngo, T.D.; Kashani, A.; Imbalzano, G.; Nguyen, K.T.Q.; Hui, D. Additive Manufacturing (3D Printing): A Review of Materials, Methods, Applications and Challenges. *Compos B Eng* **2018**, *143*, 172–196, doi:10.1016/j.compositesb.2018.02.012.
4. Rasiya, G.; Shukla, A.; Saran, K. Additive Manufacturing-A Review. *Mater Today Proc* **2021**, *47*, 6896–6901, doi:10.1016/j.matpr.2021.05.181.
5. Blakey-Milner, B.; Gradl, P.; Snedden, G.; Brooks, M.; Pitot, J.; Lopez, E.; Leary, M.; Berto, F.; du Plessis, A. Metal Additive Manufacturing in Aerospace: A Review. *Mater Des* **2021**, *209*, 110008, doi:10.1016/j.matdes.2021.110008.
6. Liu, Z.Y.; Li, C.; Fang, X.Y.; Guo, Y.B. Energy Consumption in Additive Manufacturing of Metal Parts. *Procedia Manuf* **2018**, *26*, 834–845, doi:10.1016/j.promfg.2018.07.104.
7. Peters, M.; Kumpfert, J.; Ward, C.H.; Leyens, C. Titanium Alloys for Aerospace Applications. *Adv Eng Mater* **2003**, *5*, 419–427, doi:10.1002/adem.200310095.
8. Wu, Z.; Narra, S.P.; Rollett, A. Exploring the Fabrication Limits of Thin-Wall Structures in a Laser Powder Bed Fusion Process. *The International Journal of Advanced Manufacturing Technology* **2020**, *110*, 191–207, doi:10.1007/s00170-020-05827-4.
9. L.-A. Airbus, Landing Gear Sensor Bracket. Https://Amfg.Ai/2020/01/23/ Applications-Spotlight-3d-Printed-Brackets/ .
10. F. 3D Systems, GE Aircraft Bracket. Https://Www.3dsystems.Com/Learningcenter/Case-Studies/Topology-Optimization-and-Dmp-Combine-Meet-Geaircraft-Engine-Bracket.
11. E. Airbus, Hydraulic Spoiler Manifold. Https://Www.Eos.Info/01_parts-Andapplications/Case_studies_applications_parts/_case_studies_pdf/En_cases/ Cs_m_aerospace_liebherr_en.Pdf.

12. Airbus, Reflector Bracket. Https://Www.Eos.Info/01_parts-Andapplications/Case_studies_applications_parts/_case_studies_pdf/En_cases/Cs_m_aerospace_airbus_en.Pdf.

13. Airbus, A350 XWB Pylon Bracket. Https://Www.Airbus.Com/Newsroom/Pressreleases/En/2017/09/First-Titanium-3d-Printed-Part-Installed-into-Serialproduction-.Html.

14. Karimi, J.; Suryanarayana, C.; Okulov, I.; Prashanth, K.G. Selective Laser Melting of Ti6Al4V: Effect of Laser Re-Melting. *Materials Science and Engineering: A* **2021**, *805*, 140558, doi:10.1016/j.msea.2020.140558.

15. Khorasani, A.M.; Gibson, I.; Ghasemi, A.; Ghaderi, A. Modelling of Laser Powder Bed Fusion Process and Analysing the Effective Parameters on Surface Characteristics of Ti-6Al-4V. *Int J Mech Sci* **2020**, *168*, 105299, doi:10.1016/j.ijmecsci.2019.105299.

16. Mishurova, T.; Artzt, K.; Rehmer, B.; Haubrich, J.; Ávila, L.; Schoenstein, F.; Serrano-Munoz, I.; Requena, G.; Bruno, G. Separation of the Impact of Residual Stress and Microstructure on the Fatigue Performance of LPBF Ti-6Al-4V at Elevated Temperature. *Int J Fatigue* **2021**, *148*, 106239, doi:10.1016/j.ijfatigue.2021.106239.

17. Peterson, J.; Issariyapat, A.; Umeda, J.; Kondoh, K. The Effects of Heat Treatment and Carbon Content on the Microstructure and Mechanical Properties of Laser Powder Bed Fusion Ti-6Al-4V with Dissolved TiC Particles. *J Alloys Compd* **2022**, *920*, 165930, doi:10.1016/j.jallcom.2022.165930.

18. Ter Haar, G.M.; Becker, T.H. The Influence of Microstructural Texture and Prior Beta Grain Recrystallisation on the Deformation Behaviour of Laser Powder Bed Fusion Produced Ti–6Al–4V. *Materials Science and Engineering: A* **2021**, *814*, 141185, doi:10.1016/j.msea.2021.141185.

19. Liu, J.; Li, G.; Sun, Q.; Li, H.; Sun, J.; Wang, X. Understanding the Effect of Scanning Strategies on the Microstructure and Crystallographic Texture of Ti-6Al-4V Alloy Manufactured by Laser Powder Bed Fusion. *J Mater Process Technol* **2022**, *299*, 117366, doi:10.1016/j.jmatprotec.2021.117366.

20. He, Y.; Ma, Y.; Zhang, W.; Wang, Z. Anisotropic Tensile and Fatigue Properties of Laser Powder Bed Fusion Ti6Al4V under High Temperature. *Eng Fract Mech* **2022**, *276*, 108948, doi:10.1016/j.engfracmech.2022.108948.

21. Manikandan, P.; Kumar, V.A.; Pradeep, P.I.; Vivek, R.; Manwatkar, S.K.; Rao, G.S.; Murty, S.V.S.N.; Sivakumar, D.; Narayanan, P.R. On the Anisotropy in Room-Temperature Mechanical Properties of Laser Powder Bed Fusion Processed Ti6Al4V-ELI Alloy for Aerospace Applications. *J Mater Sci* **2022**, *57*, 9599–9618, doi:10.1007/s10853-022-07032-y.

22. Jamshidi, P.; Aristizabal, M.; Kong, W.; Villapun, V.; Cox, S.C.; Grover, L.M.; Attallah, M.M. Selective Laser Melting of Ti-6Al-4V: The Impact of Post-Processing on the Tensile, Fatigue and Biological Properties for Medical Implant Applications. *Materials* **2020**, *13*, 2813, doi:10.3390/ma13122813.

23. Xue, M.; Chen, X.; Ji, X.; Xie, X.; Chao, Q.; Fan, G. Effect of Particle Size Distribution on the Printing Quality and Tensile Properties of Ti-6Al-4V Alloy Produced by LPBF Process. *Metals (Basel)* **2023**, *13*, 604, doi:10.3390/met13030604.

24. Eskandari, H.; Lashgari, H.R.; Zangeneh, Sh.; Kong, C.; Ye, L.; Eizadjou, M.; Wang, H. Microstructural Characterization and Mechanical Properties of SLM-Printed Ti–6Al–4V Alloy: Effect of Build Orientation. *J Mater Res* **2022**, *37*, 2645–2660, doi:10.1557/s43578-021-00468-z.

25. Karimi, J.; Suryanarayana, C.; Okulov, I.; Prashanth, K.G. Selective Laser Melting of Ti6Al4V: Effect of Laser Re-Melting. *Materials Science and Engineering: A* **2021**, *805*, 140558, doi:10.1016/j.msea.2020.140558.

26. Bedmar, J.; de la Pezuela, J.; Riquelme, A.; Torres, B.; Rams, J. Impact of Remelting in the Microstructure and Corrosion Properties of the Ti6Al4V Fabricated by Selective Laser Melting. *Coatings* **2022**, *12*, 284, doi:10.3390/coatings12020284.

27. Bartolomeu, F.; Gasik, M.; Silva, F.S.; Miranda, G. Mechanical Properties of Ti6Al4V Fabricated by Laser Powder Bed Fusion: A Review Focused on the Processing and Microstructural Parameters Influence on the Final Properties. *Metals (Basel)* **2022**, *12*, 986, doi:10.3390/met12060986.

28. Kasperovich, G.; Hausmann, J. Improvement of Fatigue Resistance and Ductility of TiAl6V4 Processed by Selective Laser Melting. *J Mater Process Technol* **2015**, *220*, 202–214, doi:10.1016/j.jmatprotec.2015.01.025.

29. Vrancken, B.; Thijs, L.; Kruth, J.-P.; Van Humbeeck, J. Heat Treatment of Ti6Al4V Produced by Selective Laser Melting: Microstructure and Mechanical Properties. *J Alloys Compd* **2012**, *541*, 177–185, doi:10.1016/j.jallcom.2012.07.022.

30. Vilaro, T.; Colin, C.; Bartout, J.D. As-Fabricated and Heat-Treated Microstructures of the Ti-6Al-4V Alloy Processed by Selective Laser Melting. *Metallurgical and Materials Transactions A* **2011**, *42*, 3190–3199, doi:10.1007/s11661-011-0731-y.

31. Leuders, S.; Thöne, M.; Riemer, A.; Niendorf, T.; Tröster, T.; Richard, H.A.; Maier, H.J. On the Mechanical Behaviour of Titanium Alloy TiAl6V4 Manufactured by Selective Laser Melting: Fatigue Resistance and Crack Growth Performance. *Int J Fatigue* **2013**, *48*, 300–307, doi:10.1016/j.ijfatigue.2012.11.011.

32. Huang, Q.; Liu, X.; Yang, X.; Zhang, R.; Shen, Z.; Feng, Q. Specific Heat Treatment of Selective Laser Melted Ti–6Al–4V for Biomedical Applications. *Front Mater Sci* **2015**, *9*, 373–381, doi:10.1007/s11706-015-0315-7.

33. *EOS Titanium Ti64 Grade 5 Material Data Sheet Metal Solutions*;

34. Thijs, L.; Verhaeghe, F.; Craeghs, T.; Humbeeck, J. Van; Kruth, J.-P. A Study of the Microstructural Evolution during Selective Laser Melting of Ti–6Al–4V. *Acta Mater* **2010**, *58*, 3303–3312, doi:https://doi.org/10.1016/j.actamat.2010.02.004.

35. Ferreira, S.L.C.; Bruns, R.E.; Ferreira, H.S.; Matos, G.D.; David, J.M.; Brandão, G.C.; da Silva, E.G.P.; Portugal, L.A.; dos Reis, P.S.; Souza, A.S.; et al. Box-Behnken Design: An Alternative for the Optimization of Analytical Methods. *Anal Chim Acta* **2007**, *597*, 179–186, doi:10.1016/j.aca.2007.07.011.

36. Schneider, C.A.; Rasband, W.S.; Eliceiri, K.W. NIH Image to ImageJ: 25 Years of Image Analysis. *Nat Methods* **2012**, *9*, 671–675, doi:10.1038/nmeth.2089.

37. Khorsand Zak, A.; Abd. Majid, W.H.; Abrishami, M.E.; Yousefi, R. X-Ray Analysis of ZnO Nanoparticles by Williamson-Hall and Size-Strain Plot Methods. *Solid State Sci* **2011**, *13*, 251–256, doi:10.1016/j.solidstatesciences.2010.11.024.

38. Bagasol, A.J.I.; Kaschel, F.R.; Ramachandran, S.; Mirihanage, W.; Browne, D.J.; Dowling, D.P. The Influence of a Large Build Area on the Microstructure and Mechanical Properties of PBF-LB Ti-6Al-4 V Alloy. *The International Journal of Advanced Manufacturing Technology* **2023**, *125*, 1355–1369, doi:10.1007/s00170-022-10671-9.

39. Pasang, T.; Tavlovich, B.; Yannay, O.; Jakson, B.; Fry, M.; Tao, Y.; Turangi, C.; Wang, J.C.; Jiang, C.P.; Sato, Y.; et al. Directionally-Dependent Mechanical Properties of Ti6Al4V Manufactured by Electron Beam Melting (EBM) and Selective Laser Melting (SLM). *Materials* **2021**, *14*, doi:10.3390/ma14133603.

40. Zhao, Z.; Chen, J.; Lu, X.; Tan, H.; Lin, X.; Huang, W. Formation Mechanism of the α Variant and Its Influence on the Tensile Properties of Laser Solid Formed Ti-6Al-4V Titanium Alloy. *Materials Science and Engineering: A* **2017**, *691*, 16–24, doi:10.1016/j.msea.2017.03.035.

41. Baufeld, B.; van der Biest, O. Mechanical Properties of Ti-6Al-4V Specimens Produced by Shaped Metal Deposition. *Sci Technol Adv Mater* **2009**, *10*, 015008, doi:10.1088/1468-6996/10/1/015008.

42. Tanrikulu, A.A.; Ganesh-Ram, A.; Farhang, B.; Amerinatanzi, A. Unveiling the Impact of Layerwise Laser Preheating on Microstructure and Mechanical Response in Laser Powder Bed Fusion. *J Mater Sci* **2023**, doi:10.1007/s10853-023-09066-2.

43. Pal, S.; Gubeljak, N.; Hudák, R.; Lojen, G.; Rajťúková, V.; Brajlih, T.; Drstvenšek, I. Evolution of the Metallurgical Properties of Ti-6Al-4V, Produced with Different Laser Processing Parameters, at Constant Energy Density in Selective Laser Melting. *Results Phys* **2020**, *17*, 103186, doi:10.1016/j.rinp.2020.103186.

44. Li, Z.; Li, H.; Yin, J.; Li, Y.; Nie, Z.; Li, X.; You, D.; Guan, K.; Duan, W.; Cao, L.; et al. A Review of Spatter in Laser Powder Bed Fusion Additive Manufacturing: In Situ Detection, Generation, Effects, and Countermeasures. *Micromachines (Basel)* **2022**, *13*, 1366, doi:10.3390/mi13081366.

45. Yasa, E.; Kruth, J.-P. Microstructural Investigation of Selective Laser Melting 316L Stainless Steel Parts Exposed to Laser Re-Melting. *Procedia Eng* **2011**, *19*, 389–395, doi:10.1016/j.proeng.2011.11.130.

46.    Jamhari, F.I.; Foudzi, F.M.; Buhairi, M.A. Effect of HIP on Porosity of Ti6Al4V Manufactured by Laser Powder Bed Fusion: A Brief Review. In Proceedings of the Proceedings of the 7th International Conference and Exhibition on Sustainable Energy and Advanced Materials (ICE-SEAM 2021), Melaka, Malaysia; Abdollah, M.F. Bin, Amiruddin, H., Phuman Singh, A.S., Abdul Munir, F., Ibrahim, A., Eds.; Springer Nature Singapore: Singapore, 2022; pp. 22–25.

47.    Cepeda-Jiménez, C.M.; Potenza, F.; Magalini, E.; Luchin, V.; Molinari, A.; Pérez-Prado, M.T. Effect of Energy Density on the Microstructure and Texture Evolution of Ti-6Al-4V Manufactured by Laser Powder Bed Fusion. *Mater Charact* **2020**, *163*, 110238, doi:10.1016/j.matchar.2020.110238.

48.    Pantawane, M. V.; Ho, Y.H.; Joshi, S.S.; Dahotre, N.B. Computational Assessment of Thermokinetics and Associated Microstructural Evolution in Laser Powder Bed Fusion Manufacturing of Ti6Al4V Alloy. *Sci Rep* **2020**, *10*, 1–14, doi:10.1038/s41598-020-63281-4.

49.    Huang, J.-Y.; Chang, C.-H.; Wang, W.-C.; Chou, M.-J.; Tseng, C.-C.; Tu, P.-W. Systematic Evaluation of Selective Fusion Additive Manufacturing Based on Thermal Energy Source Applied in Processing of Titanium Alloy Specimens for Medical Applications. *The International Journal of Advanced Manufacturing Technology* **2020**, *109*, 2421–2429, doi:10.1007/s00170-020-05797-7.

50.    Farabi, E.; Tari, V.; Hodgson, P.D.; Rohrer, G.S.; Beladi, H. On the Grain Boundary Network Characteristics in a Martensitic Ti–6Al–4V Alloy. *J Mater Sci* **2020**, *55*, 15299–15321, doi:10.1007/s10853-020-05075-7.

51.    Gong, J.; Wilkinson, A.J. Anisotropy in the Plastic Flow Properties of Single-Crystal α Titanium Determined from Micro-Cantilever Beams. *Acta Mater* **2009**, *57*, 5693–5705, doi:10.1016/j.actamat.2009.07.064.

52.    Muiruri, A.; Maringa, M.; du Preez, W. Evaluation of Dislocation Densities in Various Microstructures of Additively Manufactured Ti6Al4V (Eli) by the Method of X-Ray Diffraction. *Materials* **2020**, *13*, 5355, doi:10.3390/ma13235355.

53.    Hasegawa, M. Ellingham Diagram. In *Treatise on Process Metallurgy*; Elsevier, 2014; pp. 507–516.

54.    Brandl, E.; Palm, F.; Michailov, V.; Viehweger, B.; Leyens, C. Mechanical Properties of Additive Manufactured Titanium (Ti–6Al–4V) Blocks Deposited by a Solid-State Laser and Wire. *Mater Des* **2011**, *32*, 4665–4675, doi:10.1016/j.matdes.2011.06.062.

5. SELECTIVE MICROSTRUCTURE MODIFICATION FOR HIGHER STIFFNESS FOR

REINFORCED SINGLE-MATERIAL METAL ADDITIVE MANUFACTURING OF Ti-6Al-4V

5.1. Introduction and overview

Laser powder bed fusion (LPBF) stands as one of the most common Additive Manufacturing (AM) techniques for metallic components. It has garnered significant attention due to its fine feature resolution and superiorities in complex geometry fabrication. This advancement has enabled the bio-inspired [1] and lightweight component [2] fabrication in the near-net shape without the necessity of final machining. Furthermore, LPBF is capable of fabricating sub-assemblies in a single part, leading to a reduction in production costs and time [3].

Ti-6Al-4V alloy is highly demanding because of its outstanding mechanical properties such as impressive specific strength, excellent corrosion resistivity, biocompatibility, and superb fracture toughness explain its widespread use in aerospace [4–6] and biomedical industries [7–9]. Moreover, its versatility in accommodating various manufacturing processes broadens its applications across various engineering industries.

LPBF fabrication capabilities and exceptional material properties of Ti-6Al-4V advanced the popularity and usage mostly in the aerospace industry [10–12]. This compelling combination of the LPBF process and the Ti-6Al-4V material has recently earned approval from the Federal Aviation Administration (FAA) for a flight critic component fabrication [13]. However, challenges persist in certifying applications, because of the microstructure complexity, and the anisotropic mechanical behavior of LPBF-fabricated Ti-6Al-4V. While there are many studies performed to comprehensively investigate the process and materials, the challenges have not been fully addressed by researchers.

In the LPBF technique, a high-power laser beam is precisely focused onto micron-sized areas. The focused laser beam interacts with the loose powder bed at extremely high scanning speeds, resulting in rapid solidification and cooling rates [14,15]. Consequently, the LPBF technique leads to higher residual stresses in the part due to accelerated shrinkage and contraction arising from the processing method [16].

Furthermore, the heat dissipation through the built material underneath the molten metal leads to directional cooling, resulting in a grain texture in the microstructure [17–19]. This induces anisotropy in the mechanical properties of the fabricated part which is directionally dependent. This directionally dependent mechanical response of the final part is considered an extensive problem that needs to be addressed [20,21]. Commonly used approaches encompass alterations in the design and setting up the fabrication orientation which increase the production time and cost including the number of test qualifications required [22].

Researchers in materials science have been studying this highly stressed and oriented microstructure to envision how the fabrication process impacts it to novel methodologies for modifying its mechanical response. Post-heat treatment (HT) has been widely investigated as a possible technique to transform the microstructure for desired improvements in mechanical response [23–25]. The influence of the different HT techniques on the LPBF-fabricated microstructure has been studied comprehensively [26–28] and revealed for instance, an improvement in elongation up to 15.8% [24] accompanied by a notable reduction in the strength of the material.

Additionally, materials researchers have performed different strengthening mechanisms to modify the microstructure and address the challenges related to the mechanical properties of the LPBF-fabricated Ti-6Al-4V material [29–32]. An impressive milestone reported was a 26.50% enhancement in the material's strength with the addition of TiC particles during the fabrication which resulted in a drastic reduction of the elongation [33]. There is an inverse relation between strengthening and plastic deformability.

It was noted that the investigated complementary processes aimed at modifying the microstructure had the potential to either enhance the plastic deformation ability or improve the mechanical strength of the LPBF-fabricated Ti-6Al-4V. Here, a process-induced microstructure modification was examined for the impact on the material's reinforcement. This led to remarkable improvements in both mechanical strength and plastic deformation ability for LPBF-fabricated Ti-6Al-4V. Although strength and plastic deformation are inversely proportional, findings indicated that with the studied innovative reinforcement approach it is possible to achieve remarkable improvement in strength along with a significant enhancement in elongation for LPBF-fabricated Ti-6Al-4V.

A locally layerwise post-heating laser scan was introduced upon the melting scan for the corresponding regions of the selected pilar geometries for each layer where the fiber texture of the composite materials was mimicked for stiffness and reinforcement. The post-heating laser scan was studied at different laser power values and scan speeds to monitor the effect on microstructure. It was observed that optimized post-heating laser scan parameters have a significant effect on the inherent process-induced defects. The post-heating laser scan parameters that delivered the lowest porosity were assigned to the selected regions to modify the LPBF-fabricated Ti-6Al-4V material's microstructure. The novel approach, which was inspired by the composite material's nature, performed a tremendous strengthening in LPBF-fabricated Ti-6Al-4V material. Contrary to the common approaches in the literature, according to the results of the presented study, it is evident that the proposed in-situ strengthening enhances the strength along with the elongation of the material without the necessity of any complementary thermal processing or any additional compound during the fabrication.

5.2 Experimental Methods and Fabrication

5.2.1 Materials and fabrication

Ti-6Al-4V Grade 5 powder used for the fabrication was gas atomized and supplied by EOS North America (Pflugerville, TX, USA). The particle diameter of the powder ranged from 20 μm to 80 μm with a chemical composition of (wt.%) 5.50 - 6.75 Al, 3.50 - 4.50 V, 0.20 O, 0.05 N, 0.08 C, 0.015 H, 0.30 Fe, and the balance was Ti [34].

Two series of fabrications were fabricated in this study. Firstly, microstructural samples (20 mm × 6 mm × 6 mm) were fabricated using LPBF technology with an EOS M290 printer (EOS GmbH, Electro Optical Systems, Krailling, Germany) with a capacity of 400 W Ytterbium fiber laser. Before the building process, the building plate was preheated to 80 °C to prevent the delamination of the initial layers caused by high thermal gradients.

To quantize the heat input in the layerwise preheating scanning strategy and optimize the process parameters, preheating energy density was calculated using Eq. (1), where $E_v$ is the energy

density, *P* is the laser power (W), *v* is the laser scanning speed (mm/s), *t* is the layer thickness (mm), and *h* is the hatch spacing (mm) [35].

$$E_v = \frac{P}{v.h.t} \tag{5.1}$$

In this investigation, a novel approach using melting scans and fully layerwise post-heating was implemented to explore the material properties of the fabricated microstructural samples. A reference sample (non-preheated) was fabricated only with the melting laser scan. The laser process parameters for the melting scan, as suggested by the manufacturer, had a laser power of 280 W, scan speed of 1300 mm/s, hatch spacing of 120 μm, and layer thickness of 40 μm, resulting in an energy density of 44.87 J/mm³. Other scanning parameters consisted of a Gaussian-distributed laser spot size of 100 μm, a stripe scanning strategy, and a hatch angle of 67°. For the post-heating process, a fully layerwise post-heating laser scan was conducted after the melting laser scan in each layer. The fully layerwise post-heating scan encompassed a range of scanning speeds, varying from 650 mm/s to 1950 mm/s, and corresponding laser powers spanning from 140 W to 252 W, all while maintaining a consistent hatch spacing of 120 μm. The post-heating scanning parameters investigated in this chapter for each sample are provided in Table 5.1. All specimens were carefully cut out from the building plate using a wire Electrical Discharge Machining (EDM) cutter (EDM Network, Inc., Sugar Grove, IL, USA).

*Table 5.1 Laser exposure process parameters of layerwise preheating scan.*

| Sample # | Laser Power (P, W) | Scan Speed (v, mm/s) | Energy Density (E, J/mm$^3$) |
|---|---|---|---|
| 1 | 140 | 1950 | 14.96 |
| 2 | 140 | 1625 | 17.95 |
| 3 | 140 | 1300 | 22.44 |
| 4 | 140 | 650 | 44.87 |
| 5 | 196 | 1950 | 20.94 |
| 6 | 196 | 1625 | 25.13 |
| 7 | 196 | 1300 | 31.41 |
| 8 | 196 | 650 | 62.82 |
| 9 | 252 | 1950 | 26.92 |
| 10 | 252 | 1625 | 32.31 |
| 11 | 252 | 1300 | 40.38 |
| 12 | 252 | 650 | 80.77 |
| Reference | 280 | 1300 | 44.87 |

In the microstructural analysis of the initial 16 fabricated samples, Sample #11 exhibited the highest density and was subsequently selected for further investigation (refer to Section 5.3.1). The laser processing parameters for post-heating of this sample, characterized by a laser power (P) of 140 W and a scan speed (V) of 650 mm/s, were identified as the optimized conditions for the post-heating process.

Building upon the data derived from the first fabrication phase, the second fabrication was strategically designed. This phase involved the creation of four dog-bone shaped tensile samples, aimed at assessing the impact of the post-heated region's size on the structural and mechanical properties of the samples. Figure 5.1 illustrates the experimental setup: Sample 1 was produced without any post-heating laser treatment. In contrast, Samples 2 to 4 underwent an initial melting process using the recommended laser parameters, followed by a localized post-heating treatment applying the optimized laser parameters on the same layer. This localized post-heating zone, designed in SolidWorks, formed several rods along the length of the tensile samples with varying diameters. Specifically, as depicted in Figure 5.1, Samples 2, 3, and 4 incorporated designed rods with diameters of 0.4 mm, 0.6 mm, and 0.8 mm, respectively. The designs

incorporate pillar geometries with diameters of Ø0.4 mm, Ø0.6 mm, and Ø0.8 mm, corresponding to double

scanned region areas of 47.5%, 66.7%, and 55.4%, respectively.
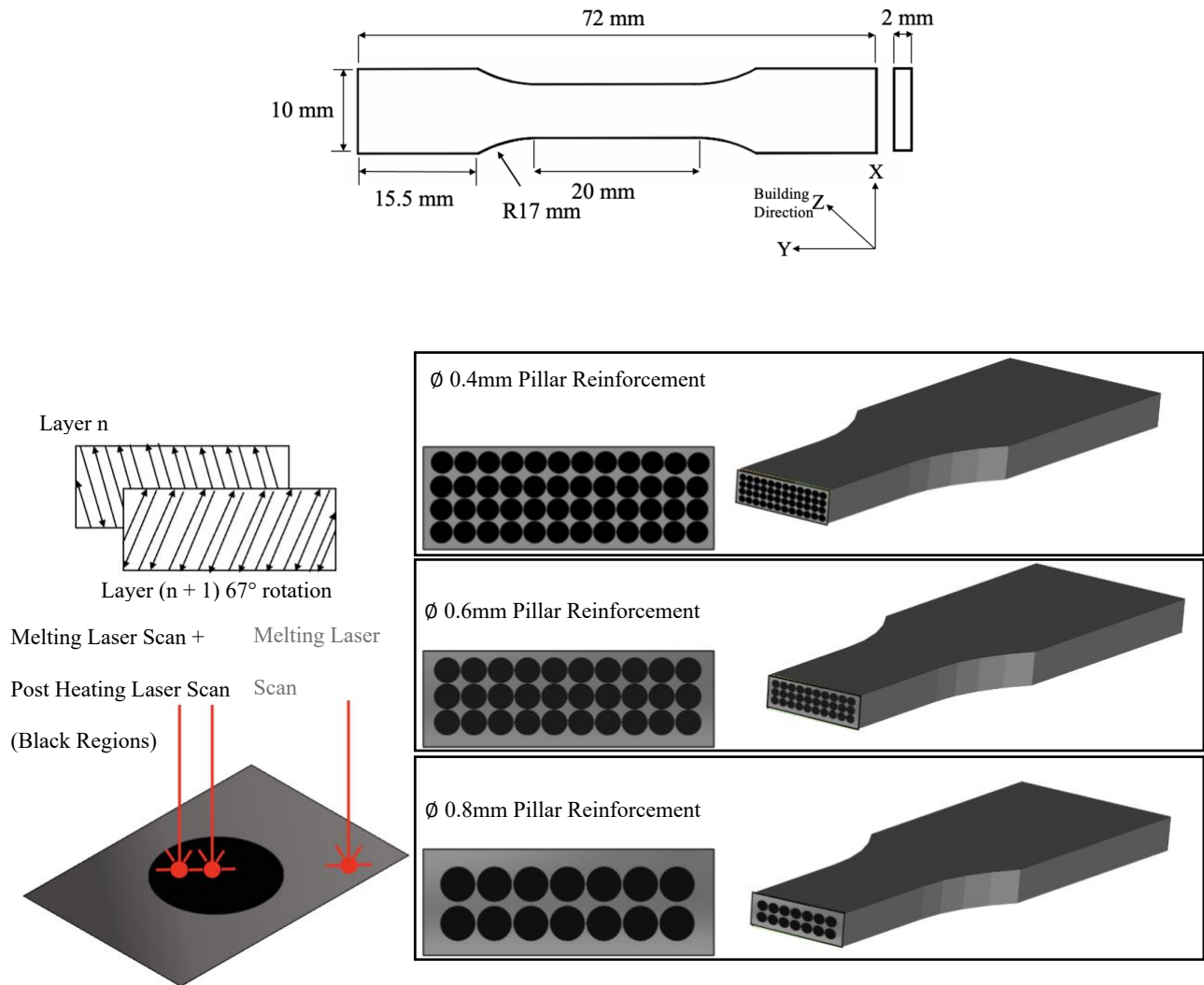




*Figure 5.1. 'Dimensions of tensile test samples with highlighted post-heating regions. The black-marked areas in the gauge cross-section indicate zones subjected to dual scanning processes (initial melting laser scan followed by optimized post-heating laser scan) .'*

Samples were fabricated using laser powder bed fusion (LPBF) technology with an EOS M290

printer (EOS GmbH, Electro Optical Systems, Krailling, Germany) using Ytterbium fiber laser power of

400 W. To quantize the effect of the applied post-heating scan after melting the laser track, post-heating

energy density was calculated from the energy density equation reported by Thijs *et al.* (Eq 1) [36].

$$E_v = \frac{P}{v.h.t} \tag{1}$$

The suggested process parameters by the with a Gaussian distribution of energy, and 40 μm of layer thickness with 67° angle stripes scanning strategy. These parameters were used for the melting laser scan on each layer initially and defined as the default parameters. These parameter sets were kept constant for the melting laser scan for all fabrications. To explore the impact of the post-heating laser scan on the microstructure central composite design (CCD) [37] was used for the post-heating laser scan process parameters covering a range of laser scan speeds from 650 mm/s to 1950 mm/s and laser power from 140 W to 252 W. In this design of experiment (DoE) 15 different variants were defined by the Box-Behnken method (Table 5.2). The cross-section of the microstructure samples was fully exposed to the post-heating laser scan application at each layer.

The second fabrication aimed to produce locally layerwise post-heated regions in the tensile coupons, to create higher stiffness at the designated areas in the cross-section of the coupons. Fibers of the composite materials were mimicked and different pillar shape regions were designed along the longitude axis of the tensile testing coupons in the loading direction. The post-heating process parameter that delivered the lowest porosity value from the first fabrication and the microstructural evaluation assigned as the post-heating laser scan parameters during the second fabrication which is referred as the locally layerwise post-heating laser scan application.

The third fabrication process printed fatigue coupons to investigate the impact of the locally layerwise post-heating application on the material properties under cycling loadings. A continuous radius coupon design was selected from the ASTM E466-21 standard practice for the fatigue tests. The radius of the gauge length is R56mm with a minimum width of 7mm. According to the standard limitations of the cross section the thickness was designed with a thickness of 3mm.

All specimens were cut from the building plate using a wire Electrical Discharge Machining (EDM) cutter (EDM Network, Inc., Sugar Grove, IL, USA).

5.2.2 Experimental Methods

5.2.2.1 Microstructure Characterization

Scanning Electron Microscopy (SEM) imaging studies were performed for porosity, $\alpha$-phase lath thickness, and grain morphology caused by various post-heating energy inputs. Samples were cut out by a TECHCUT 5™ precision low-speed cutter (Allied High-Tech Products, Inc., Rancho Dominguez, CA, USA) from the center of the specimen along the building plane, prior to the sample preparation. Samples were cold mounted and prepared by grinding from 320 to 1200 grit size of SiC sandpaper. Afterward, the first step of polishing was performed on a DiaMat ® polishing cloth with 1 μm diamond suspension. Polishing finalized with 0.04 μm colloidal silica suspension on Red Final C ® polishing pad used to obtain scratch-free, mirror-like finish sample surfaces. Polished samples were rinsed in micro-organic soap and cleaned with isopropyl alcohol. Samples were etched with Kroll's reagent (1–3 mL HF, 2–6 mL $HNO_3$, 100 mL water) to identify the grain boundaries and phases of the microstructure.

Image J [38], an image analysis software, was used to calculate the porosity level of each microstructure. The porosity distribution was determined from at least three different regions at 2 magnification levels (500x and 1000x). Image J was also used for the lath thickness calculation of the $\alpha$-phase. For image processing, microstructure images were first converted to RGB stack-type grayscale images prior to setting the auto contrast level. Thresholding was generated to create a clear contrast between $\alpha/\alpha'$ phases' lath borders. Particles were analyzed between 0.2 μm to 2.0 μm then total counts of the particle at each size were calculated for the mean value. This calculation made at least 6 different images for statistically meaningful data from every sample's building plane orientation.

X-ray diffraction analyses were performed for phase identification, calculation of the lattice parameters, and orientations of the microstructure of each sample. A Bruker D8 Advance X-ray diffractometer (Bruker Corporation, Madison, WI, USA) was used for the analysis with 1.5406 Å Cu k-alpha wavelength, 40 mA current, 40 kV voltage at room temperature, and the measurements were taken with step intervals of 0.2° and a scan speed of 1sec/step while the 2θ varied between 20° to 80°.

Lattice parameters were calculated according to Bragg's law (Eq (2)) where d, is inter-planar spacing, a and c are the lattice parameters and h, k, l are the Miller indices.

$$\frac{1}{d^2} = \frac{4}{3}\left(\frac{h^2+hk+k^2}{a^2}\right) + \frac{l^2}{c^2} \tag{2}$$

$$\lambda = 2d\ sin\theta$$

The Williamson – Hall (W–H) model [39] was employed to assess the microstrain condition of the microstructure of the reference and post-heating laser scan application. The XRD data was utilized in the following equations (Eq (3) (4) (5)). Peak broadening of the XRD data is caused by crystal imperfections and distortion which is related by $\varepsilon \approx \beta_s / \tan\theta$. The W–H plot was used for the calculation of the microstrain value. Si standard reflection (0.0013 rad) [40] was subtracted before strain analysis using W–H method. The Scherrer's equation (Eq (3)) derived to Eq (5) where $\beta$ is peak broadening, $\lambda$ is the wavelength (Å). K is the Cu $K_s$ (0.94), D is the crystallite size (nm) and $\theta$ is the peak position.

$$D = \frac{\lambda\ K}{\beta\ cos\theta} \tag{3}$$

$$\beta = \sqrt{\beta_T{}^2 - \beta_i{}^2} \tag{4}$$

$$\beta\ cos\theta = \frac{\lambda\ K}{D} + 4\varepsilon\ sin\theta \tag{5}$$

5.2.2.2 Mechanical testing

Shimadzu EHF E-Series (100kN) equipped with a 4830-servo controller (Shimadzu Scientific Instruments, Inc., Missouri City, TX, USA) was used for tensile testing. Strain measurements of the gauge region were made by using a digital image correlation (DIC) system. The surface strain and displacements were captured by tracking the patterns of the high-contrast speckles on the coupon surface. This contactless technique can measure the local strains at the fracture as well as the global strain during the loading of the coupons. Two 2.3MP CCD cameras, Grasshopper GS3-U3-23S6M (FLIR Systems, Inc., Santa Barbra, CA, USA) with a pixel array of 1920 x 1200 were used for image capturing. Processing of the captured images and correlation with the stress loading were made using VIC-3D® software (Correlated Solutions, Inc.,

Irmo, SC, USA). Considering the previous studies [41], the loading rate was set to 1.2 mm/min for all tests. Fatigue tests were also performed with the Shimadzu EHF E-series (100kN) test machine. $\sigma_{max}$ applied as 300 MPa with a frequency of 50Hz and R=0.1 during the fatigue testing.

5.3. Results

5.3.1. Microstructure Defects

The porosity levels corresponding to the selected post-heating laser power values and post-heating laser scan speeds were studied using the Box-Behnken DoE model on the fabricated 15 microstructural samples fabricated in the first fabrication. A total of fifteen post-heating laser power and scan speed variations were characterized and their effect on porosity was evaluated. The impact of the layerwise post-heating on the porosity level of the microstructure is shown in Figure 5.2. Additionally,  SEM micrographs at various regions and magnification levels for each scenario revealed that the post-heating laser scan significantly impacted the inherent porosity level of LPBF Ti-6Al-4V. the response surface plot for the layerwise fully post-heating laser power between 140 – 252W and post-heating laser scan speed between 650 – 1950 mm/s was depicted in Figure 5.3 (a). It was confirmed that 650 mm/s post-heating laser scan speed delivered the minimum porosity levels for each post-heating laser scan power.
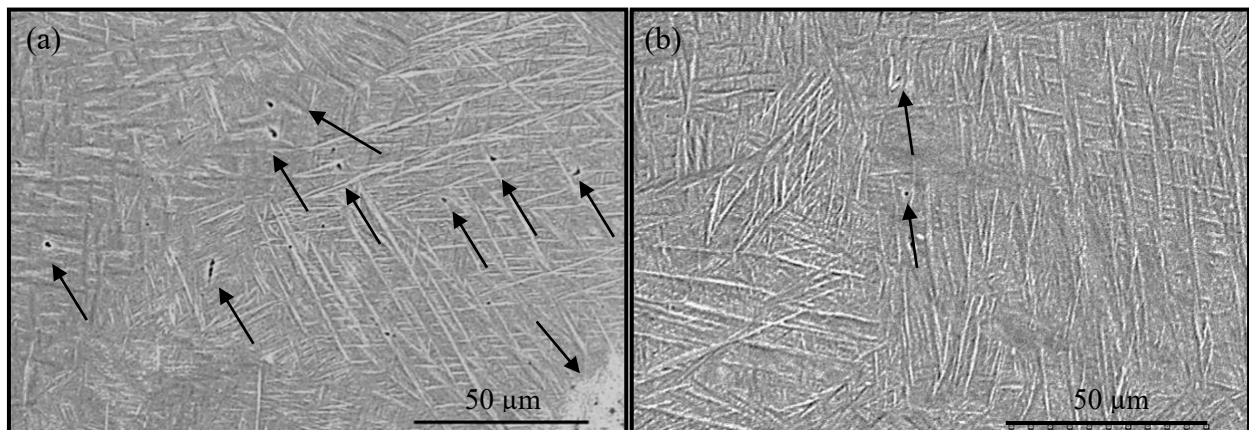


*Figure 5.2. SEM images comparing porosity defects in (a) reference sample without post-heating and (b) fully layerwise post-heated sample (Post-heating Laser P:140W and V: 650 mm/s)*

Additionally, it was observed the post-heating laser power of 140W minimized the porosity during the experimental study. The relation between the post-heating laser scan speed and the porosity level of the

microstructure at the constant post-heating laser scan power (140 W) was depicted in Figure 5.3 (b). The porosity level of the reference sample without a complemental post-heating laser scan was measured at 0.47% ± 0.015 [42]. It was undoubted that a subsequent laser scan decreased the initial porosity level, and it was measured to be up to 90%. The denser microstructure of the post-laser scan can be ascribed to remelting [43,44]. The inherent porosity level of the LPBF Ti-6Al-4V was minimized with the post-heating laser scan parameters of 140 W laser power and 650 mm/s laser scan speed. These optimized parameters delivered almost a fully dense (>99.95%) microstructure and were subjected to further microstructural and mechanical testing as the post-heating laser scan sample and selected for the post-heating laser applications of the presented study. The microstructure response after the locally layerwise post-heating laser scan for pillar diameters of Ø0.4 mm, Ø0.6 mm, and Ø0.8 mm was illustrated in Figure 5.3 (c), and the porosity levels were measured as 0.08 ± 0.01%, 0.07 ± 0.06%, 0.07 ± 0.07%, respectively.

(c)
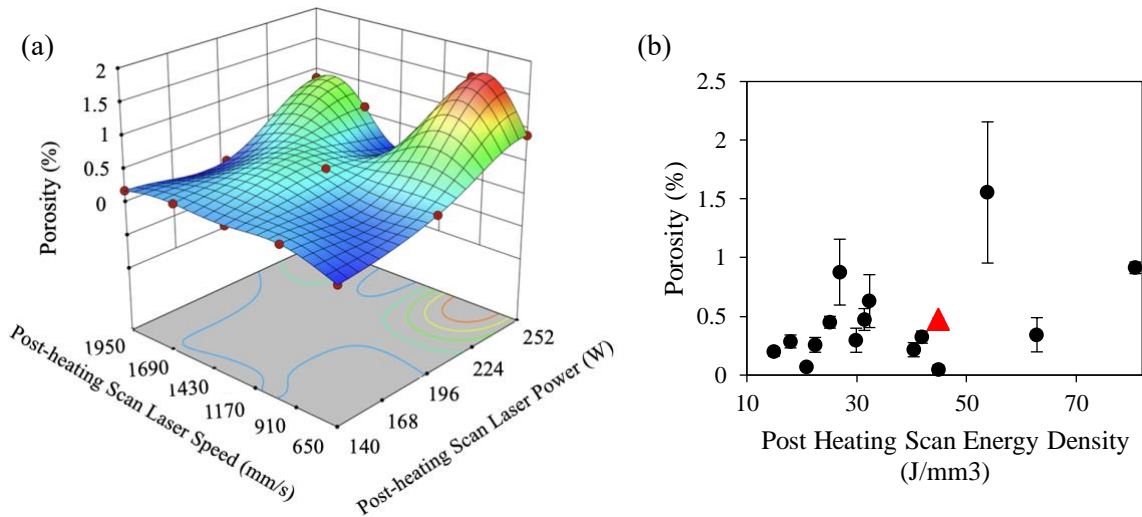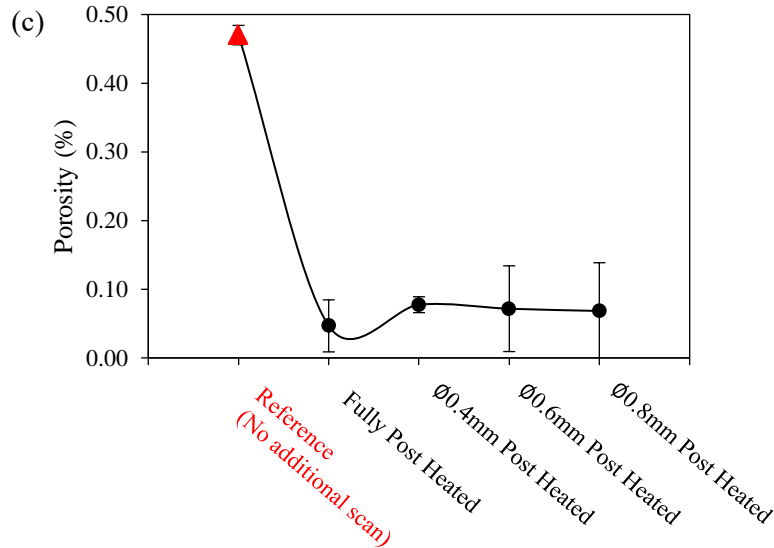
*Figure 5.3. 'Porosity level was optimized at a post-heating laser scan speed of 650 mm/s for a variety of post-heating laser scan speeds. Post-heating laser power of 140W minimized the porosity of the microstructure, (a) RSM analysis of porosity in LPBF fabricated Ti-6Al-4V microstructure with varying post-heating laser scan power and speed, (b) Porosity values of the fully layerwise post-heating laser scan at various laser parameters,*
*(c) Impact of different locally layerwise post-heating scanning areas on microstructural response to porosity.*

### 5.3.2. Grain Morphology and Lattice Structure

The microstructure of the Ti-6Al-4V, an α + β alloy, fabricated via LPBF consists of a greater number of α/α′ phases at room temperature, which exhibits a basketweave-like structure [45]. The lath thickness of the basketweave-like structure determines the mechanical response of the alloy [46]. The grain morphology of the Ti-6Al-4V alloy was assessed, and the response of the α/α′ phases' lath structure to the applied processes was evaluated. Table 1 depicts the average lath thickness and the lath angle for each application. The average lath thickness of the samples was measured with image processing [38] of the SEM micrographs at magnification levels of 500x, 800x, 1200x, and 1500x. The lath thickness of the reference sample was measured to be 0.797 ± 0.005 μm. The highest lath thickness was observed in the microstructure samples which were fully exposed to the optimized post-heating laser scan (0.894 ± 0.051 μm). The lowest lath thickness was observed in the double-scanned regions of the Ø0.4 mm pillar reinforcement application (0.687 ± 0.007). It was evident that an additional post-heating laser scan across

101

the entire cross-section of the samples had a significant effect on lath thickness. Results showed a 12% increase in the lath thickness between the reference (no additional laser scan) and the sample fully exposed to the post-heating laser scan. The variation in lath thickness between the single and double-scanned regions in the microstructure of reinforcement applications was also evaluated. The limited application of the post-heating laser scan only to the projection of the pillar geometries on the samples' cross-section, locally layerwise post-heating, did not have a major effect compared to the fully applied post-heating laser to the samples' cross-section. The highest variation was observed in the Ø0.8 mm pillar application and calculated as a 3.6% increase with the addition of a locally layerwise post-heating laser scan.
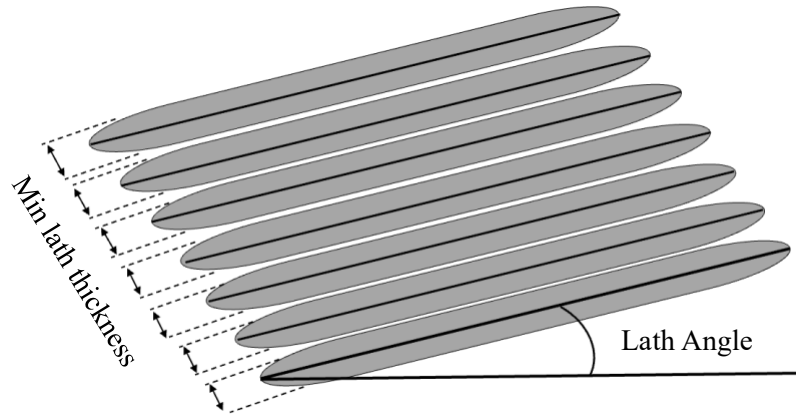


*Figure 5.4. Representative image of an α/α' colony and how the microstructure image is processed by the software for the lath thickness and angle.*

Table 5.2. *HCP – Ti (α/α' phases) lath thickness and angle*

| | Reference (No additional laser scan) | Fully Post-heated | Ø0.4mm Pillar Reinforcement Scan | | Ø0.6mm Pillar Reinforcement Scan | | Ø0.8mm Pillar Reinforcement Scan | |
| --- | --- | --- | --- | --- | --- | --- | --- | --- |
| | | | Melting Scan (single scan region) | Melting + Post-heating Scan (double scan region) | Melting Scan (single laser region) | Melting + Post-heating Scan (double laser region) | Melting Scan (single laser region) | Melting + Post-heating Scan (double laser scan) |
| Ave. Lath thickness (μm) | 0.797 ± 0.005 | 0.894 ± 0.051 | 0.691 ± 0.006 | 0.687 ± 0.007 | 0.749 ± 0.007 | 0.727 ± 0.006 | 0.690 ± 0.010 | 0.715 ± 0.005 |
| Ave. Lath Angle (°) | 118.08 ± 2.69 | 81.88 ± 7.27 | 95.13 ± 3.77 | 98.38 ± 3.07 | 95.20 ± 1.99 | 98.00 ± 1.85 | 98.19 ± 0.81 | 94.36 ± 1.32 |

Lath structure micrograph images of the α/α′ phases of each application are shown in Fig.3. The representative images of the microstructure variation between the single-scan and double-scanned regions (projection of the pillar geometries on the cross-section) for Ø0.4, Ø0.6, and Ø0.8 mm pillar reinforcement application are illustrated in Figure 5.5 (c), (d), and (e) respectively. The lath thickness slightly decreased in the double-scanned scan regions for Ø0.4 mm and Ø0.6 mm pillar size. In opposition, the lath thickness was measured thicker in Ø0.8 mm pillar size at the double scanned regions.
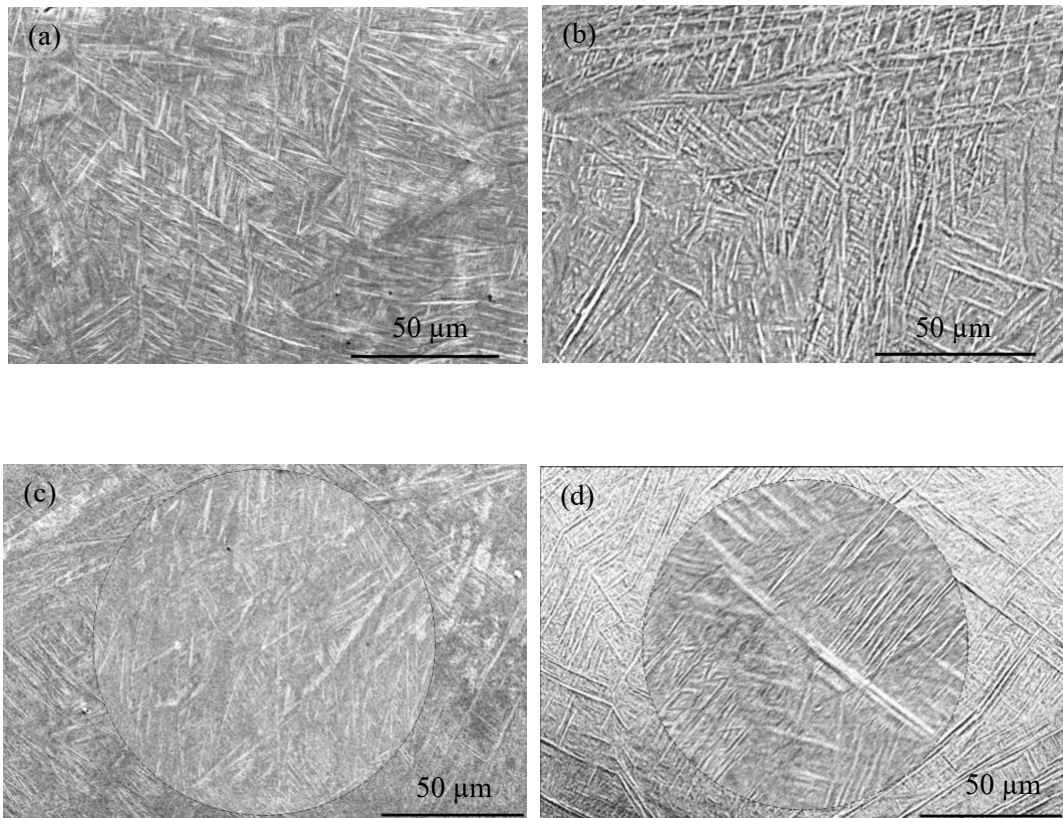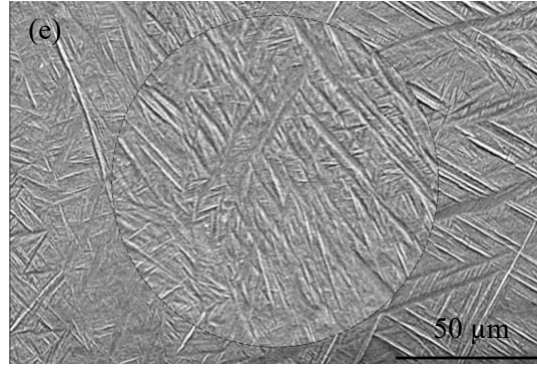
*Figure 5.5. 'SEM micrograph of LPBF fabricated Ti-6Al-4V; (a) microstructure of reference sample with no additional laser scan, (b) Thicker α/α' lath structure (12% higher) after the application of the optimized post-heating laser scan fully across the cross-section, Lath structure variation between the locally layerwise post-heated regions (pillar geometry projection on the cross-section was double-scanned (melting laser scan + post-heating laser scan)) and the single-scanned (only melting laser scan) regions for (c) Ø0.4 mm pillar size, (d) Ø0.6 mm pillar size, and Ø0.8 mm pillar size.'*

In addition to size, the angle of the α-colonies affects the deformation mechanism and the strength of the Ti-6Al-4V alloy [47]. The lath angle of the α/α' phases was analyzed with image processing [38]. The lath angles with respect to their width have been presented in Figure 5.6. Lath sizes between the range of 0 to 2 μm have been plotted with their corresponding angles. It was observed that almost all the laths concentrated themselves either within 0º and 75º or between 75º and 180º. The lath densities in the measured window are found to be higher in the double-exposed region than in the single-exposed region as seen in Figure 5.6. This phenomenon was observed with all other pillar sizes tested.

(c) Ø0.4 mm Pillar Reinforcement Single-scanned region (c) Ø0.4 mm Pillar Reinforcement Double-scanned region



(d) Ø0.6 mm Pillar Reinforcement Single-scanned region (e) Ø0.6 mm Pillar Reinforcement Double-scanned region

(f) Ø0.8 mm Pillar Reinforcement Single-scanned region (g) Ø0.8 mm Pillar Reinforcement Double-scanned region
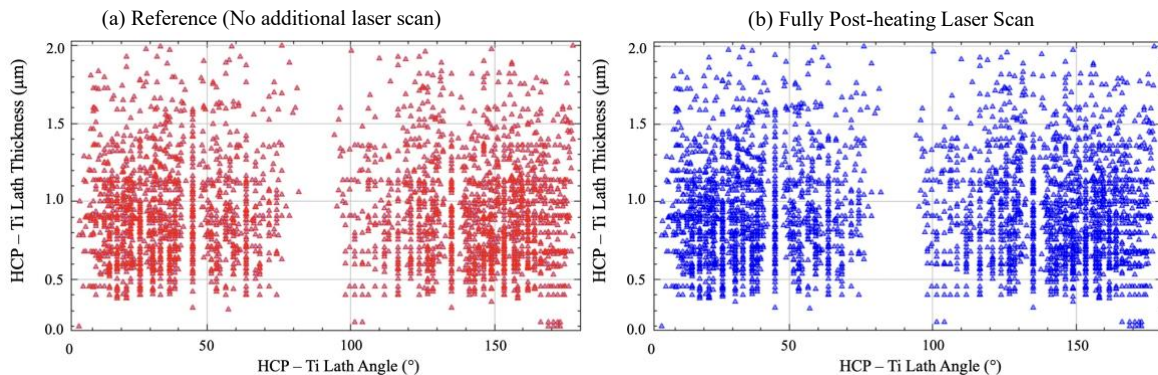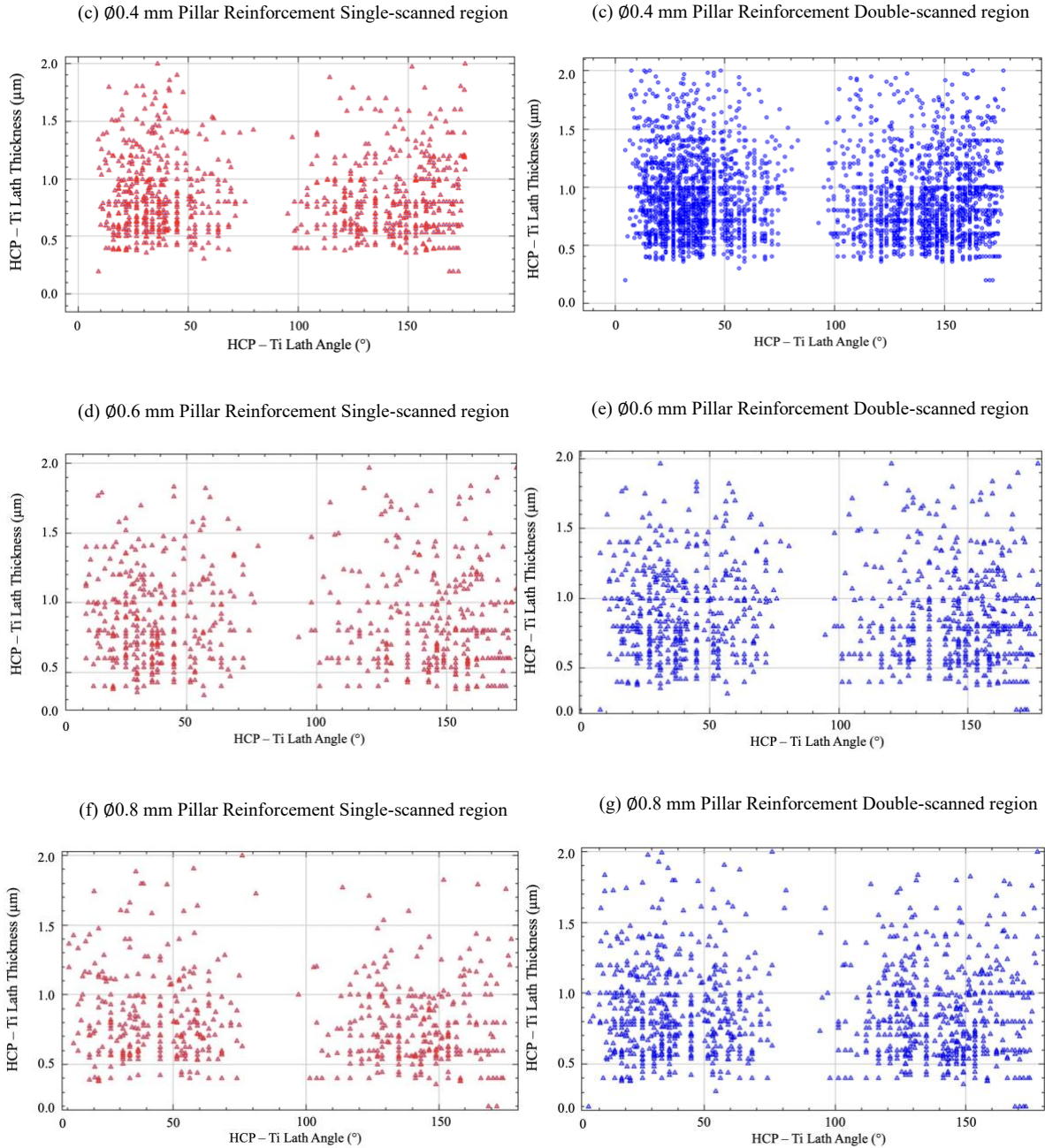
*Figure 5.6. '(a) Lath distribution of the reference sample with no additional laser scan, (b) lath distribution of the fully post-heated sample, (c) single-scanned (only melting laser scan) regions of the Ø0.4 mm pillar reinforcement application have lower lath angle compared to the (d) doubled-scanned regions. Ø0.6 mm pillar reinforcement application has the same behavior (d) single-scanned regions have lower lath angle compared to (e) double-scanned regions. On the contrary, (f) single-scanned regions have higher lath angle compared to double-scanned regions in Ø0.8 mm pillar reinforcement application.*

The investigated grain morphology of the α/α′ phases have a hexagonal close-packed (HCP) lattice structure. Lattice parameters HCP structure of the α/α′ phases were calculated according to Bragg's law

[48] and plotted in Figure 5.7. A reduction in both lattice parameters of a and c was observed (Figure 5.7 (a) and (b)). Additionally, a strain on the lattice was observed with the applied post-heating laser scan. Figure 5.7 (c) shows the strain with a higher c/a ratio with the additional laser scan. The post-heating laser scan increased the c/a ratio of the lattice which is a result of the lower cooling rate [49] of the post-heating laser scan application.
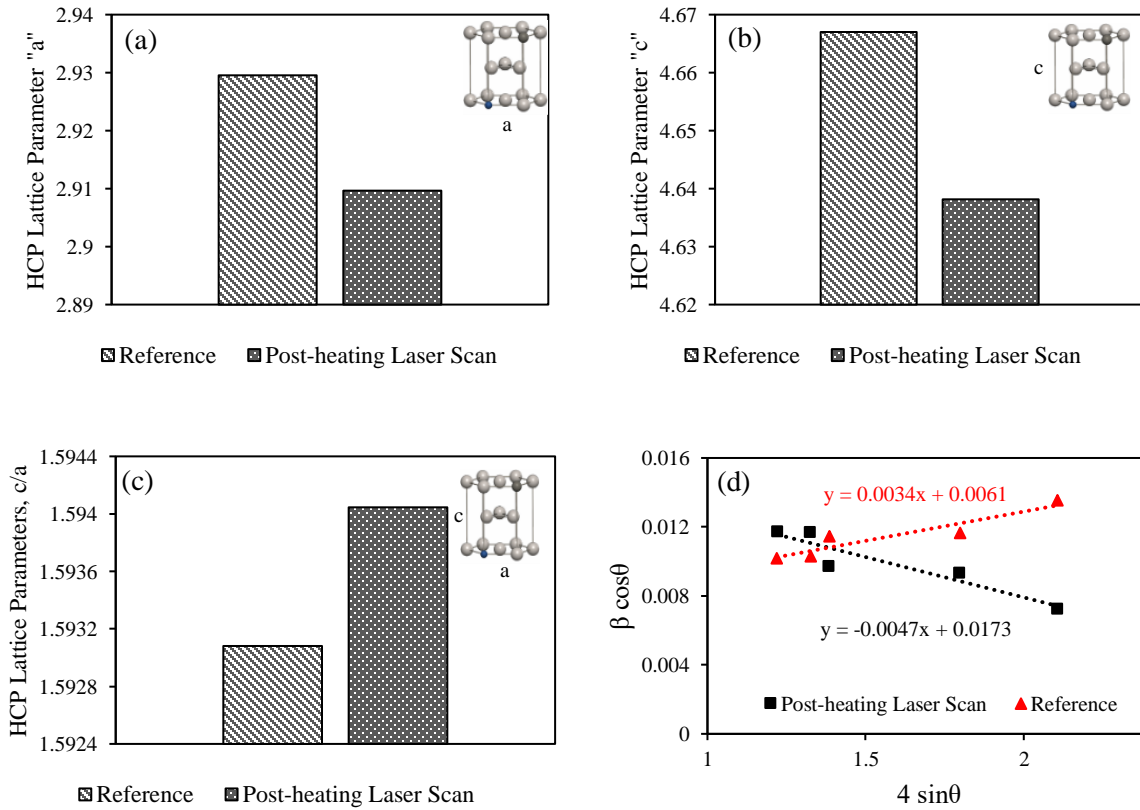


*Figure 5.7. The effect of the post-heating laser scan on HCP Lattice parameters; Sequent laser scan decreased the HCP lattice parameters "a" (a) and "c" (b). Post-heating laser scan increased the lattice distortion, c/a (c). The W-H model shows that the tension stress mode of the reference sample turned out to be a compression mode with the application of the post-heating laser scan (d).*

The W-H model was employed for further microstructure analysis to gain a better understanding of the strain and stress condition of the samples. Eq (5) was considered as a y = mx + c equation and the equation was plotted as the W-H model in which the slope of this equation is the microstrain value [39]. According to the model, the initial microstrain condition of the microstructure at the reference sample without a complementary post-heating laser scan was determined as tension. The positive slope of the

plotted model of the reference sample is shown in red in Figure 5.7 (d). A remarkable change in the initial condition of the LPBF Ti-6Al-4V was observed after the application of the post-heating laser scan. The plotted model of the post-heating laser scan shows a negative slope which indicates that the microstrain condition of the microstructure was turned out in compression mode. The effect of the tension and compression mode of the microstructure on the mechanical response will be discussed in the discussion section.

### 5.3.3. Compositional Analysis XRD

Figure 5.8 depicts the XRD profiles of the reference and fully layerwise post-heated specimens. The highest intensity of Bragg's peak was observed at the (101) plane on the reference sample. It is noteworthy that the strongest peak intensity was observed at the (002) plane on fully layerwise post-heated sample. The remarkable change in the peak intensities indicated that the majority of the grain orientation was modified with the applied post-heating laser scan along the (002) plane.
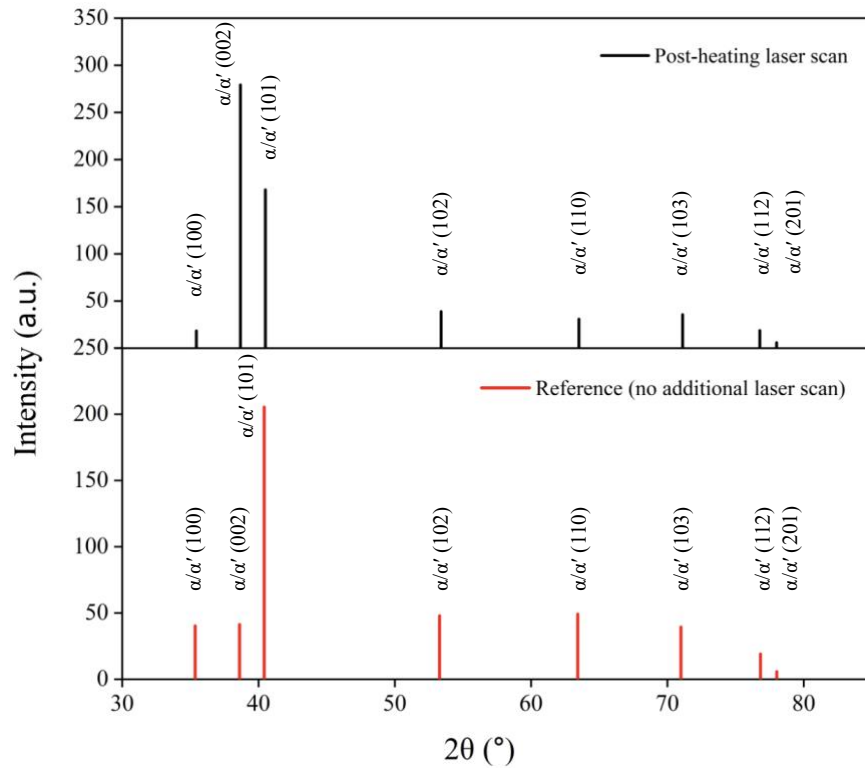


*Figure 5.8. 'The XRD patterns of the reference without additional laser scan and the post-heating laser scan specimens'*

5.3.4. Mechanical Testing

The mechanical response of the modified microstructure was quantized through tensile testing. The stress-strain plot is depicted in Figure 5.9. The locally layerwise post-heating laser scan reinforcement strategy had a significant effect on the mechanical response of the material. It was observed that both ultimate tensile strength (UTS) and yield strength (YS) values were enhanced. A remarkable increase in the slope during elastic deformation led to a higher YS for each locally layerwise post-heating laser scan strategy applied in the present study. The enhancements in YS were 31.47%, 20.15%, 49.40%, and 41.83% for the reinforcement applications of fully post-heating, $\emptyset 0.4$ mm, $\emptyset 0.6$ mm, and $\emptyset 0.8$ mm pillar size, respectively. The $\emptyset 0.6$ mm pillar reinforcement delivered an extensive advancement in UTS with a strength value of $1477 \pm 121.7$ MPa. This is followed by $\emptyset 0.8$ mm pillar reinforcement, fully post-heated application, and $\emptyset 0.4$ mm pillar reinforcement with the strength values of $1401.6 \pm 90.9$ MPa, $1357.1 \pm 96.2$ MPa, $1166.4 \pm 44.0$ MPa, respectively. Pillar geometries of $\emptyset 0.4$ mm and $\emptyset 0.6$ mm delivered exceptional elongations, which were 12.5% and 22.2% higher compared to the reference sample, respectively. On the contrary $\emptyset 0.8$ mm pillar reinforcement coupons and the fully post-heating coupons ended up with a slightly lower elongation compared to the reference sample.

Figure 5.9. (a) Stress-strain curves for reference (black) and locally layerwise post-heating laser scan reinforcement applications. Each locally layerwise post-heating laser scan strategy, coupled with the specific reinforcement geometry, contributed to the enhanced strength of the LPBF-fabricated Ti-6Al-4V material. Notably, Ø0.6 mm (yellow) pillar reinforcement demonstrated the most significant strength advancement. Ø0.4 mm (green) and Ø0.6 mm (yellow) pillar reinforcement also enhanced the elongation extensively. However, fully post-heated (gray) and Ø0.8 mm (blue) pillar reinforcement only enhanced the material's strength. (b) Detailed values for the material elongation and strength are listed in the table.

Fatigue tests were performed under the loading conditions of $\sigma_{max}$ = 300 MPa, R= 0.1, and 50 Hz Figure 5.10. illustrates the total number of cycles for each reinforcement application. There was no significant contribution was observed with the application of the reinforcement strategy in the fatigue lifetime of the coupons.
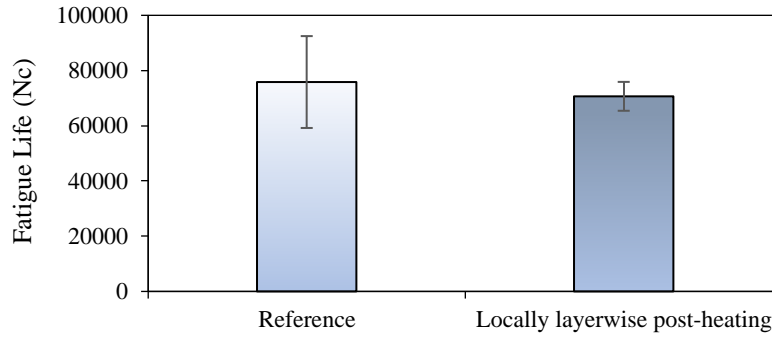
*Figure 5.10. Number of total cycles under dynamic loading conditions for the reference and the locally layerwise preheating reinforcement strategy of the LPBF-fabricated Ti-6Al-4V.*

Further fractography analyses were performed on the fracture surfaces of each specimen to gain a deeper understanding of the effects of fatigue loading on the microstructure. Figure 5.11 exhibits the fracture surface of the samples specifically the interface between the reinforced regions and the single scan regions. It was observed that each application exhibits cracks in the interface between the reinforced and non-reinforced regions. This can be explained by the stiffness variation between the regions.
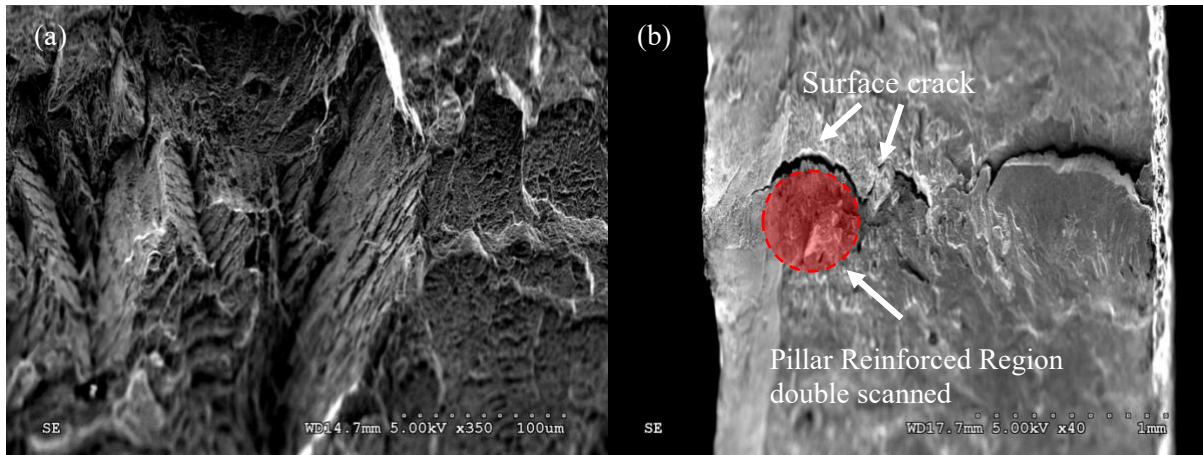


*Figure 5.11. Fracture surface of the fatigue samples (a) Reference Sample with no additional thermal process, (b) crack at the interface of the pillar reinforcement sample*

## 5.4. Discussions

In the present study, an in-situ strengthening strategy during the LPBF process for Ti-6Al-4V was evaluated. A post-heating laser scan was employed upon the melting scan to maximize the relative density and modify the Ti-6Al-4V material's microstructure in terms of α/α′ phases (HCP-Ti) grain and lattice

structure. Furthermore, the complementary post-heating laser scans aimed to enhance the inherent grain texture of the LPBF-fabricated Ti-6Al-4V through directional solidification and cooling. The post-heating laser scan was applied both fully across the microstructure and only to the designated regions in the specimens' cross-section. The fiber structure of the composite materials was replicated in the presented study, and pillar geometries with different diameters were assigned into the samples as the fibers during the design process and a building file was generated for the scan strategy for each application accordingly. The projection of these geometries onto the cross-section of the coupons was exposed to an additional post-heating laser scan which parameters minimized the inherent porosity value. The preliminary data of the microstructure, which was fully exposed to the post-heating laser scan, clearly indicated a strengthening effect. It is rational to observe a reduction in the material's elongation for the strengthened materials [50]. With this strategy, ~50% of the cross-section was aimed at strengthening, thus the reduction in the elongation would be limited compared to the fully post-heated sample. Results proved that the reinforcement strategy presented in this study improved the elongation whereas the LPBF fabricated Ti-6Al-4V delivered higher strength compared to previous thermal processing studies.

The impact of the post-heating laser scan parameters (laser power (W), laser scan speed (mm/s)) on the process-induced porosity can be seen in Figure 5.3. (a). The figure provides significant insights regarding the correlation between post-heating laser scan parameters, such as laser power and scanning speed, and their impact on reducing the porosity level. It was observed the post-heating laser scan power of 140W and scanning speed of 650 mm/s delivered the lowest porosity level. Post-heating laser scan with 140W laser power and 650 mm/s scanning speed decreased the porosity level from 0.470% to 0.046%. Additionally, results indicated that the lowest porosity value for different post-heating laser powers (252W and 196W) was delivered with a scanning speed of 650 mm/s (Fig.2 (b)). A similar effect was reported in re-melting studies with higher energy inputs to the powder bed [51–53] and Hot Isostatic Pressure (HIP) applications in which additional processing was required  [54,55].

Figure 5.3. (c) illustrates the porosity level of the applied reinforcement strategies with different pillar sizes. However, the improvement in porosity was not as much as the fully post-heated microstructure, a significant improvement in porosity level was observed. This can be rationalized by the decrease in the total area of the double-scanned regions.

The predominant stable phases in the LPBF-fabricated Ti-6Al-4V microstructure at room temperature were observed as α and α′ phases. Due to the complexity of the LPBF fabricated Ti-6Al-4V alloy's microstructure it requires additional microstructure characterization tools to distinguish these phases from each other which is not the scope of the presented study. It has been a common practice in the literature to evaluate the microstructure of LPBF-fabricated Ti-6Al-4V alloy for its mechanical properties together as the α/α′ phases, α-Ti or HCP-Ti [56]. The difference between these phases depends on the cooling rate and their structure is distinct from each other due to the lath thickness. The higher cooling rate delivers a thinner lath thickness which is called as martensite and annotated as α′ phase, and the relatively slower cooling regions are α phases with a pattern called Widmanstätten [57]. It is rational to examine both phases together since the average lath thickness was considered for the microstructure investigation. In addition, both phases have an HCP lattice structure, which cannot be distinguished when computing the lattice parameters using XRD data. The impact of the post-heating laser scan on α-Ti lath thickness is listed in Table 5.1. The application of the post-heating laser scan fully across the microstructure increased the average lath thickness of the material. A comparable effect was observed with the conventional HTs, however, the observed lath coarsening after the applied post-heating laser scan (12.17% increase) was below the reported HT applications; Zou *et al.* [58] applied heat treatment to LPBF Ti-6Al-4V below the β-transus temperature (925°C/2hr/FC(7°C/min)) and authors reported a 40% increase on lath thickness, Lu *et al.* [59] applied a heat treatment above the β-transus temperature (1015°C/1hr/AC) and a 75% increase on lath thickness was reported. In addition to these conventional post-heat treatments, Karami *et al.* [60] reported a ~110% increase with the application of hot isostatic processing (HIP) HIP (920°C/2hr/100MPa) was reported.

*Table 5.3 Effect of the post-HT on the mechanical behavior of the LPBF Ti-6Al-4V*

| | Heat Treatment | YS As-Built (MPa) | YS HTed (MPa) | As-Built Elongation (%) | HTed Elongation (%) | Change of YS (%) | Change of Elongation (%) |
|---|---|---|---|---|---|---|---|
| Etesami *et al.*[61] | 900°/2hr/AC | ~1180 | ~1100 | 8.7 | 4.9 | -6.77 | -43.67 |
| Simonelli *et al.* [62] | 730°C/2h/FC | 1075±25(H) 967±10(V) | 974±7(H) 937±7(V) | 7.6±0.5(H) 8.9±0.4(V) | 7.0±0.5(H) 9.6±0.9(V) | -9.39 -3.10 | -8.57 7.86 |
| Vilaro *et al.* [63] | Supersolvus | 1137±20(H) 962±47(V) | 913±7(H) 836±64(V) | 7.6±2(H) 1.7±0.3(V) | 8.9±1(H) 7.9±1(V) | -19.70 -13.09 | 17.11 364.7 |
| | Subtransus | 1137±20(H) 962±47(V) | 944±8(H) 925±14(V) | 7.6 ± 2(H) 1.7±0.3(V) | 8.5±1(H) 7.5±2(V) | -19.70 -3.84 | 11.84 341.1 |
| | Low Temperature | 1137±20(H) 962±47(V) | 965±16(H) 900±101(V) | 7.6 ± 2(H) 1.7±0.3(V) | 9.5 ± 1(H) 1.9±0.8(V) | -15.12 -6.44 | 25.00 11.76 |
| Vrancken *et al.* [64] | 540°C/5hr/WQ | 1110±9 | 1118±39 | 7.28±1.12 | 5.36±2.02 | 0.72 | -26.37 |
| | 1020°C /2hr/FC | 1110±9 | 760±19 | 7.28±1.12 | 14.06±2.53 | -31.53 | 93.13 |
| | 850°C/5hr/FC | 1110±9 | 909±6 | 7.28±1.12 | Premature failure | -18.10 | N/A |
| | 1050°C/0.5hr/AC + 730°C/2hr/AC | 1110±9 | 822 ± 19 | 7.28±1.12 | 12.74±0.56 | -25.94 | 75.00 |
| Cao *et al.* [65] | 800°C/2hr | ~1020(H) ~950(V) | ~950(H) ~850(V) | ~4 ~4 | ~9 ~6 | -6.86 -10.52 | 125.00 50.00 |
| Sabban *et al.* [66] | 975°C - 875°C (Cyclic HT) /24hr/AC | 1047±23(H) 1043±18(V) | 865±19(H) 849±12(V) | 10±1(H) 12±1(V) | 18±1(H) 16±1(V) | -17.38 -18.60 | 80.00 33.33 |
| Zhang *et al.* [67] | 900°C/6hr/AC | 1112±8 | 864±3 | 7 ± 1 | 10 ± 1 | -22.30 | 42.86 |
| Yan *et al.* [68] | 750°C/2hr/FC | 1351 | 1185 | 3.14 | 3.4 | -12.29 | 8.28 |
| | 800°C/2hr/FC+AC | 1065 | 996 | 6 | 7 | -6.47 | 16.67 |
| | 1080°C/2hr/FC+AC | 1065 | 840 | 6 | 4 | -21.12 | -33.33 |
| Kasperovich *et al.* [69] | 900°C/2hr + 700°C/1hr /FC(10K/min) | 986 | 908 | 11.9 | 9.5 | -7.91 | -20.17 |
| Facchini *et al.*[70] | Annealed 600°C | 990±5 | 870±15 | 8.1±0.3 | 11.0±0.5 | -12.12 | 35.80 |
| Fully Post Heating Laser Scan | - | 753.5 ± 37.7 | 990.6 ± 80.4 | 7.2 ± 0.4 | 7.0 ± 0.4 | 31.4 | -2.7 |

| | | | | | | | |
|---|---|---|---|---|---|---|---|
| Ø0.4 mm Pillar Post Heating Laser Scan | - | 753.5 ± 37.7 | 905.5 ± 44.3 | 7.2 ± 0.4 | 8.1 ± 0.2 | 20.2 | 12.5 |
| Ø0.6 mm Pillar Post Heating Laser Scan | - | 753.5 ± 37.7 | 1125.6± 85.4 | 7.2 ± 0.4 | 8.8 ± 0.7 | 49.4 | 22.2 |
| Ø0.8 mm Pillar Post Heating Laser Scan | - | 753.5 ± 37.7 | 1068.8 ± 61.7 | 7.2 ± 0.4 | 6.5 ± 0.2 | 41.8 | -9.7 |

α/α′ lath colonies decompose from the β-grain boundaries during the phase transformation below the allotropic transformation temperature. The cooling rate during the phase transformation defines the nucleation and grain growth of the precipitate phase. Faster cooling rates resulted in thinner laths with more randomly distributed structures since α/α′ nucleation starts irregularly inner side of the β-grain as well as the β-grain boundaries [45]. A schematic view of the α/α′ lath colonies formation is depicted in Figure 5.11.

| β-grains: Above β-transus temperature | β-phase decomposition to α + β: Phase transformation temperature | α/α′ colonies: Room temperature |
|---|---|---|
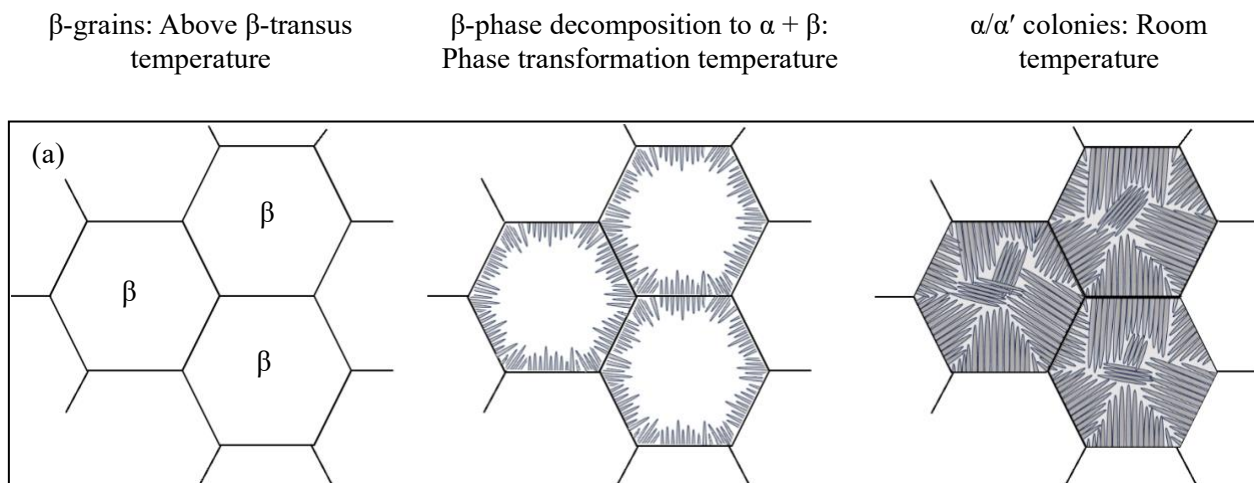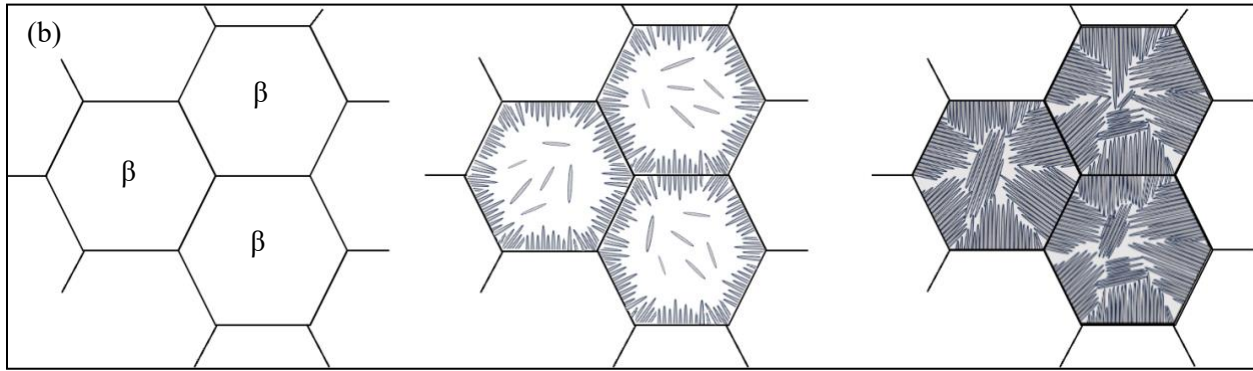
*Figure 5.11. Phase transformation of the Ti-6Al-4V (a) β → α + β decomposition at a slower cooling rate ends up with relatively thicker α/α' colonies. (b) β → α + β decomposition at a faster cooling rate starts with more random nucleation and ends up with relatively thinner α/α' colonies.*

A slight decrease in the lath thickness of the α/α′ colonies was observed in the double-scanned regions of the ∅0.4 mm and ∅0.6 mm reinforcement applications. Authors considered this as a result of a faster cooling rate. The effective thermal conductivity of the Ti-6Al-4V powder bed during the melting scan is 0.13 W/mK [71] which is much less compared to the bulk Ti-6Al-4V. Findings revealed a linear relation between the temperature of the Ti-6Al-4V and its thermal conductivity, according to the study presented by Saini *et al.*[72] thermal conductivity of Ti-6Al-4V exceeds 20 W/mK at 1200 °C. This value is almost 154 times higher than the thermal conductivity of the loose powder. The complementary post-heating process applied the high-temperature solidified Ti-6Al-4V material which has relatively higher thermal conductivity and led to a faster cooling rate and delivered thinner α/α′ colonies (Table 1). The reinforcement application of the ∅0.8 mm had a different response which will be evaluated in future studies.

The angle at which the laths align themselves gives us an idea of the homogeneity in microstructure formation and thus the strength of the resulting part [73]. In-homogeneity in the grain orientations is one of the primary sources of dislocation sites from where the crack initiates before leading to failure upon mechanical loading. Figure 5.6. helps us comment on the grain orientations observed in the pillar regions compared to non-pillar regions. Looking at the lath density concentrations, grain orientation homogeneity seems to improve within the pillar regions. This highlights that the resulting solid part comprises homogeneous and in-homogeneous grain orientations. It should also be noted that as the pillar size reduced,

the largely variant lath densities in the pillar region when compared to the non-pillar regions seem to be reduced. This might be because of the fact that the volume of material receiving the higher energy density has a direct correlation to its effect on the lath formation in the neighboring regions. Bigger pillars transfer higher thermal energy to the non-processed regions thus making the entire region of a cross-section with uniformly orienting laths.

The lath thickness of the α/α′ phase had a significant effect on the mechanical response of the LPBF Ti-6Al-4V material [61,74]. Hadadzadeh *et al.* [74] attributed the high strength of LPBF Ti-6Al-4V to finer α/α′ laths through the Hall-Petch effect [75] and Etesami *et al* [61] reported the remarkable effect of the α/α′ laths width on elongation during the tensile test. In the present study, lath coarsening was observed, and it is one of the reasons for the preferred elongation.

The findings, as depicted in Figure 5.7, demonstrated the post-heating laser scan has a remarkable effect on the LPBF-fabricated Ti-6Al-4V lattice structure as well as the microstrain. An increase in the lattice parameters was reported in previous studies [76,77] with the application of the post-heat treatment. The increase in the lattice parameters was attributed to the higher diffusivity of the vanadium atoms [77,78] of Ti-6Al-4V during the post-heat treatment temperatures. Vanadium atoms diffused out of the HCP lattice and larger titanium atoms [79] occupied their positions which transformed the structure into a larger lattice. On the contrary to the conventional post-heat treatment applications, a slight decrease in the lattice parameters both a and c was observed with the application of the post-heating laser scan (Figure 5.7 (a) & (b)). Lattice shrinkage can be explained by the vanadium atoms diffusion mechanism. It is well-known that additional heat leads to an increase in temperature which improves the solubility of the substitutional atoms in this case of the post-heating laser scan application it is vanadium atoms [80]. The increasing amount of the substitutional vanadium atoms leads to a decrease in the lattice parameters since vanadium has smaller atomic radii compared to titanium atoms that were substituted by vanadium during the post-heating laser scan. Compared to the conventional HTs, the post-heating laser scan exhibits a relatively higher cooling rate. The smaller lattice parameters of the post-heating laser scan can be rationalized with faster cooling

116

rates with lower diffusivity, which limits the diffusion of the excessive vanadium atoms from their positions inside the HCP lattice.

The previous study demonstrated that introducing an additional laser scan to the powder bed exceeds the operation temperature, causing an increase in the amount of oxygen in titanium [42]. This makes the molten metal more sensitive to oxidation, even under shield gas protection. The lattice strain measured in the presented study (Figure 5.7) can be justified by the same phenomenon. Figure 5.12 depicts the representative image of the super-saturated HCP lattice with the octahedral position occupied by the oxygen atoms which strains the lattice along the c-axis. In addition to the lattice strain, Figure 5.7 depicts the decrease in both a and c lattice parameters, the result of the trapped vanadium atoms in the HCP lattice which occupies the titanium atom positions with smaller atomic radii.

Single-scanned Regions Lattice

Doubled-scanned Regions Lattice

Post-heating



Titanium          Vanadium          Aluminum          Oxygen
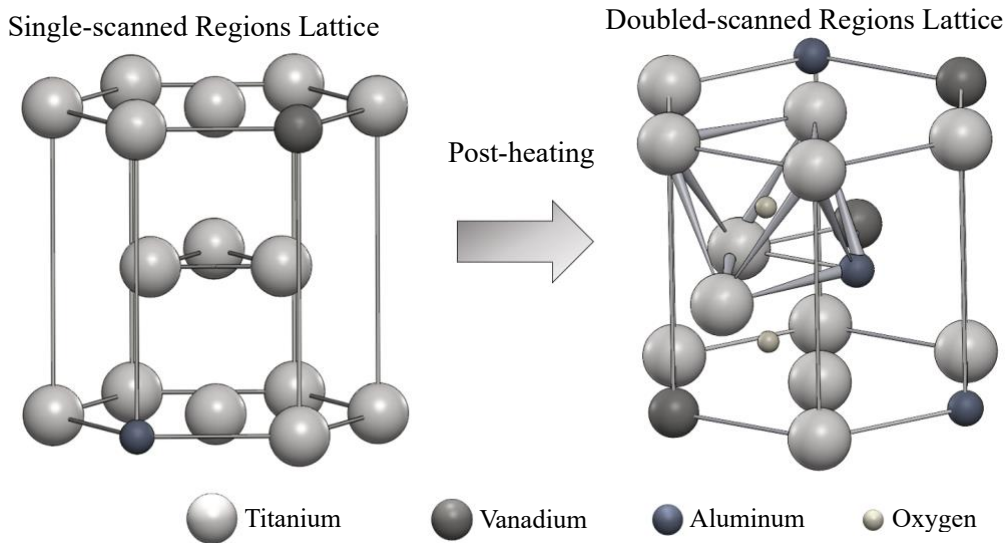
*Figure 5.12. Super-saturated HCP-Ti with the energy addition of the post-heating laser scan. Substitutional vanadium atoms occupied the titanium atom positions with the applied post-heating laser scan. Additionally, with additional laser scans oxygen atoms occupied the octahedral positions in the HCP-Ti.*

The resulting tensile strength and elongation on the reinforcement applications have been studied (Figure 5.9.) It was observed that post-heating through a second laser scan resulted in a remarkable enhancement in the material's strength. It is rational to have a lower elongation with the increase in strength after the strengthening process [33]. This is noticeable when the post-heating laser scan was applied fully

across the cross-section of the material (Figure 5.9. (a) gray line). Considering that, when the post-heating laser was carried out in limited localized regions (circular area of the pillar geometry projection on the sample cross-section), there seems to be a significant increase in the elongation along with tensile strength for the 0.4 mm and 0.6 mm pillar diameter (Figure 5.9. (a) green and yellow line). It is interesting to note that the highest elongation was observed for the 0.6 mm pillar size reinforcements which also had the highest tensile strength among all the test cases. This fascinating occurrence of obtaining higher strength and higher elongation can be explained by the reinforcement matrix formation due to the combination of finer and coarser $\alpha/\alpha'$ lath regions obtained within the cross-section of a solidified Ti6Al4 microstructure. It further helped to direct research attention toward identifying the limits at which the matrix strengthening occurs depending on the reinforced area of the post-heated section. It should also be noted that the shape of the region that is being post-heated might influence the properties as well which need to be further investigated.

The common practice of strengthening in the literature has been studied by introducing additional elements and components to the microstructure of the LPBF-fabricated Ti-6Al-4V such as nitrogen, and titanium-carbide. Liu *et al.* [81] investigated the in-situ nitrogen strengthening of the LPBF-fabricated Ti-6Al-4V by introducing nitrogen to the build chamber through the shield gas. The highest improvement in the YS was reported as 20.01% with a drastic reduction in elongation. However, the authors reported a significant improvement in the material's strength, the elongation of the strengthened material was decreased by almost half of the initial condition. He *et al.* [82] studied the strengthening of the Ti-6Al-4V with the addition of $LaB_6$ to the LPBF process. In their study, the highest improvement in the material's strength was 14.50% with a 37.2% reduction in elongation. TiC addition to the Ti-6Al-4V components during the LPBF process is also a preferred way to reinforce the material [33,83]. Jiang *et al.* [83] investigated the effect of TiC in Ti-6Al-4V during the LPBF process and the authors reported titanium matrix composites with TiC addition had a 10.68% higher strength with a very limited elongation. Tang *et al.* [33] in their TiC reinforcement study, it was reported that the highest improvement in strength was ~26.50% with an elongation of 3.65% which is less than half of the initial as-built condition of the material.

118

Previous studies have revealed that the strengthening of LPBF fabricated Ti-6Al-4V was limited to ~26.50% and caused a notable reduction in elongation. The proposed innovative reinforcement strategy of locally layerwise post-heating laser scan was assigned to designated regions on the specimen. It was observed that the studied reinforcement strategy of locally layerwise post-heating laser scan resulted in a remarkable improvement of ~50% in YS which is the highest enhancement in the strength among the previously reported studies. More importantly, a remarkable improvement in the elongation (>22% improvement) was also achieved with the proposed composite additive manufacturing application for the first time. Thus, the elongation reduction due to the strengthening is promised to be controlled as well as improved for the engineering applications.

Post-heating HT is one of the most popular complementary processes that was applied to modify the microstructure of the LPBF-fabricated Ti-6Al-4V. Table 2 depicts the mechanical response of the modified microstructure after the HT. However, there are some studies that reported a decrease both in strength and elongation, the general response after HT was a decrease in the strength and an increase in elongation. It is due to the lath coarsening and the stress relieving effect of the HT which is discussed previously. The studied post-heating laser scan strategy modified the LPBF Ti-6Al-4V microstructure by reforming the α/α′ phases lath structure (Table 5.1. and Figure 5.6.), HCP lattice structure (Fig.5.5), initial microstrain mode (Figure 5.7.) and the grain texture (Figure 5.8.). Figure 5.13 depicts the yield strength and the elongation of the LPBF fabricated Ti-6Al-4V material after conventional HT and the locally layerwise post-heating laser scan reinforcement application (green region). Considering the studies listed in Table 5.2 and Figure 5.9 the proposed reinforcement application that mimicked the composite materials with a complementary post-heating laser scan of the limited regions of the cross-section during the fabrication promised to dismiss the thermal post-processing of LPBF fabricated Ti-6Al-4V with superior mechanical properties.
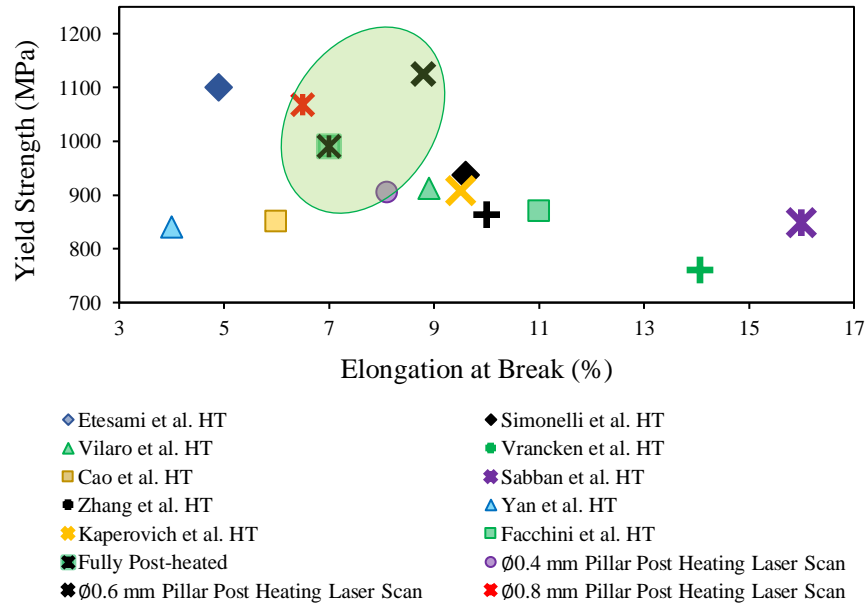
*Figure 5.13. The general trend in the applied post-heating as HT after fabrication is a decrease in strength and an increase in elongation. The locally layerwise post-heating laser scan reinforcement application promises remarkable improvement in strength as well as elongation.*

A notable enhancement in YS was observed for each reinforcement application, attributed to the modification of the α/α′ colonies by locally layerwise post-heating laser scan (Figure 5.9). Compared to the reference sample each post-heating application had limited deformation in the elastic region, the steeper graphs are evident of the higher stiffness of the materials. It is known that the grain boundary network with respect to the population and connectivity enhances the polycrystalline materials [84]. The stiffness improvement with the reinforcement application can be explained by the modified α/α′ lath colonies where the grain boundaries are resistant to grain boundary sliding. At further deformation, modified grain boundary crystallography impacts the dislocation motion [85] which was observed in the present study with higher UTS values during the tensile testing (Figure 5.9).

Fractography images (Figure 5.11) show that the stiffness variation between the double-scanned (reinforcement region) and the single-scan regions causes stress concentration points and micro-cracks initiated during the cyclic loading. Thus, the process-induced reinforcement with locally layerwise post-heating did not contribute to the fatigue life of the material.

## 5.5. References

[1]     J. Yang, D. Gu, K. Lin, Y. Zhang, M. Guo, L. Yuan, H. Zhang, H. Zhang, Laser Additive Manufacturing of Bio-inspired Metallic Structures, Chinese Journal of Mechanical Engineering: Additive Manufacturing Frontiers. 1 (2022) 100013. https://doi.org/10.1016/j.cjmeam.2022.100013.

[2]     A. Scarpellini, V. Finazzi, P. Schito, A. Bionda, A. Ratti, A.G. Demir, Laser Powder Bed Fusion of a Topology Optimized and Surface Textured Rudder Bulb with Lightweight and Drag-Reducing Design, J Mar Sci Eng. 9 (2021) 1032. https://doi.org/10.3390/jmse9091032.

[3]     C. Tan, F. Weng, S. Sui, Y. Chew, G. Bi, Progress and perspectives in laser additive manufacturing of key aeroengine materials, Int J Mach Tools Manuf. 170 (2021) 103804. https://doi.org/10.1016/j.ijmachtools.2021.103804.

[4]     Z. Liu, B. He, T. Lyu, Y. Zou, A Review on Additive Manufacturing of Titanium Alloys for Aerospace Applications: Directed Energy Deposition and Beyond Ti-6Al-4V, JOM. 73 (2021) 1804–1818. https://doi.org/10.1007/s11837-021-04670-6.

[5]     A.K. Jha, S.K. Singh, M. Swathi Kiranmayee, K. Sreekumar, P.P. Sinha, Failure analysis of titanium alloy (Ti6Al4V) fastener used in aerospace application, Eng Fail Anal. 17 (2010) 1457–1465. https://doi.org/10.1016/j.engfailanal.2010.05.007.

[6]     A.A. Antonysamy, P. Prangnell, Microstructure, Texture and Mechanical Property Evolution during Additive Manufacturing of Ti6Al4V Alloy for Aerospace Applications, 2012. https://login.ezproxy.uta.edu/login?url=https://www.proquest.com/dissertations-theses/microstructure-texture-mechanical-property/docview/1771283583/se-2?accountid=7117.

[7]     W.S.W. Harun, N.S. Manam, M.S.I.N. Kamariah, S. Sharif, A.H. Zulkifly, I. Ahmad, H. Miura, A review of powdered additive manufacturing techniques for Ti-6al-4v biomedical applications, Powder Technol. 331 (2018) 74–97. https://doi.org/10.1016/j.powtec.2018.03.010.

[8]     J.A. Tamayo, M. Riascos, C.A. Vargas, L.M. Baena, Additive manufacturing of Ti6Al4V alloy via electron beam melting for the development of implants for the biomedical industry, Heliyon. 7 (2021) e06892. https://doi.org/10.1016/j.heliyon.2021.e06892.

[9]     L.E. Murr, S.A. Quinones, S.M. Gaytan, M.I. Lopez, A. Rodela, E.Y. Martinez, D.H. Hernandez, E. Martinez, F. Medina, R.B. Wicker, Microstructure and mechanical behavior of Ti–6Al–4V produced by rapid-layer manufacturing, for biomedical applications, J Mech Behav Biomed Mater. 2 (2009) 20–32. https://doi.org/10.1016/j.jmbbm.2008.05.004.

[10]    A. Pathania, A.K. S., N. B.K., S. Barad, Effect of post-heat treatment with super β transus temperature on the damping behaviour of LPBF-processed Ti6Al4V thin rotor blade, Proceedings of the Institution of Mechanical Engineers, Part L: Journal of Materials: Design and Applications. (2023). https://doi.org/10.1177/14644207231186511.

[11]    A. Marques, A. Cunha, M. Gasik, O. Carvalho, F.S. Silva, F. Bartolomeu, 3D multi-material laser powder bed fusion: Ti6Al4V–CuNi2SiCr parts for aerospace applications, Progress in Additive Manufacturing. (2023). https://doi.org/10.1007/s40964-023-00460-5.

[12]    Lütjering Gerd, Williams James C, Titanium Matrix Composites, in: Titanium, Springer Berlin Heidelberg, Berlin, Heidelberg, n.d.: pp. 367–382. https://doi.org/10.1007/978-3-540-73036-1_9.

[13]    Kerry Lynch, Honeywell Gains FAA Nod for 3D-printed Flight-critical Part, Ainonline. (2020). https://www.ainonline.com/aviation-news/defense/2020-08-20/honeywell-gains-faa-nod-3d-printed-flight-critical-part (accessed July 11, 2023).

[14]    J. Karimi, C. Suryanarayana, I. Okulov, K.G. Prashanth, Selective laser melting of Ti6Al4V: Effect of laser re-melting, Materials Science and Engineering: A. 805 (2021) 140558. https://doi.org/10.1016/j.msea.2020.140558.

[15]    A.M. Khorasani, I. Gibson, A. Ghasemi, A. Ghaderi, Modelling of laser powder bed fusion process and analysing the effective parameters on surface characteristics of Ti-6Al-4V, Int J Mech Sci. 168 (2020) 105299. https://doi.org/10.1016/j.ijmecsci.2019.105299.

[16]    T. Mishurova, K. Artzt, B. Rehmer, J. Haubrich, L. Ávila, F. Schoenstein, I. Serrano-Munoz, G. Requena, G. Bruno, Separation of the impact of residual stress and microstructure on the fatigue performance of

LPBF Ti-6Al-4V at elevated temperature, Int J Fatigue. 148 (2021) 106239. https://doi.org/10.1016/j.ijfatigue.2021.106239.

[17] J. Peterson, A. Issariyapat, J. Umeda, K. Kondoh, The effects of heat treatment and carbon content on the microstructure and mechanical properties of laser powder bed fusion Ti-6Al-4V with dissolved TiC particles, J Alloys Compd. 920 (2022) 165930. https://doi.org/10.1016/j.jallcom.2022.165930.

[18] G.M. Ter Haar, T.H. Becker, The influence of microstructural texture and prior beta grain recrystallisation on the deformation behaviour of laser powder bed fusion produced Ti–6Al–4V, Materials Science and Engineering: A. 814 (2021) 141185. https://doi.org/10.1016/j.msea.2021.141185.

[19] J. Liu, G. Li, Q. Sun, H. Li, J. Sun, X. Wang, Understanding the effect of scanning strategies on the microstructure and crystallographic texture of Ti-6Al-4V alloy manufactured by laser powder bed fusion, J Mater Process Technol. 299 (2022) 117366. https://doi.org/10.1016/j.jmatprotec.2021.117366.

[20] Y. He, Y. Ma, W. Zhang, Z. Wang, Anisotropic tensile and fatigue properties of laser powder bed fusion Ti6Al4V under high temperature, Eng Fract Mech. 276 (2022) 108948. https://doi.org/10.1016/j.engfracmech.2022.108948.

[21] P. Manikandan, V.A. Kumar, P.I. Pradeep, R. Vivek, S.K. Manwatkar, G.S. Rao, S.V.S.N. Murty, D. Sivakumar, P.R. Narayanan, On the anisotropy in room-temperature mechanical properties of laser powder bed fusion processed Ti6Al4V-ELI alloy for aerospace applications, J Mater Sci. 57 (2022) 9599–9618. https://doi.org/10.1007/s10853-022-07032-y.

[22] Standard Terminology for Additive Manufacturing-Coordinate Systems and Test Methodologies 1 This international standard was developed in accordance with internationally recognized principles on standardization established in the Decision on Principles for the Development of International Standards, Guides and Recommendations issued by the World Trade Organization Technical Barriers to Trade (TBT) Committee, n.d. http://www.ansi.org.

[23] K. Zhang, W.H. Kan, Y. Liu, X. Gao, Y. Zhu, S.C.V. Lim, H. Peng, A. Huang, Microstructure control by heat treatment for better ductility and toughness of Ti-6Al-4V produced by laser powder bed fusion, Australian Journal of Mechanical Engineering. 19 (2021) 680–691. https://doi.org/10.1080/14484846.2021.2004654.

[24] F.I. Jamhari, F.M. Foudzi, M.A. Buhairi, A.B. Sulong, N.A. Mohd Radzuan, N. Muhamad, I.F. Mohamed, N.H. Jamadon, K.S. Tan, Influence of heat treatment parameters on microstructure and mechanical performance of titanium alloy in LPBF: A brief review, Journal of Materials Research and Technology. 24 (2023) 4091–4110. https://doi.org/10.1016/j.jmrt.2023.04.090.

[25] M.-T. Tsai, Y.-W. Chen, C.-Y. Chao, J.S.C. Jang, C.-C. Tsai, Y.-L. Su, C.-N. Kuo, Heat-treatment effects on mechanical properties and microstructure evolution of Ti-6Al-4V alloy fabricated by laser powder bed fusion, J Alloys Compd. 816 (2020) 152615. https://doi.org/10.1016/j.jallcom.2019.152615.

[26] B. Vrancken, L. Thijs, J.-P. Kruth, J. Van Humbeeck, Heat treatment of Ti6Al4V produced by Selective Laser Melting: Microstructure and mechanical properties, J Alloys Compd. 541 (2012) 177–185. https://doi.org/10.1016/j.jallcom.2012.07.022.

[27] G. Yu, Z. Li, Y. Hua, H. Liu, X. Zhao, W. Li, X. Wang, The Effects of Post Heat Treatment on the Microstructural and Mechanical Properties of an Additive-Manufactured Porous Titanium Alloy, Materials. 13 (2020) 593. https://doi.org/10.3390/ma13030593.

[28] X. Yan, C. Shi, T. Liu, Y. Ye, C. Chang, W. Ma, C. Deng, S. Yin, H. Liao, M. Liu, Effect of heat treatment on the corrosion resistance behavior of selective laser melted Ti6Al4V ELI, Surf Coat Technol. 396 (2020) 125955. https://doi.org/10.1016/j.surfcoat.2020.125955.

[29] J. Peterson, A. Issariyapat, J. Umeda, K. Kondoh, The effects of heat treatment and carbon content on the microstructure and mechanical properties of laser powder bed fusion Ti-6Al-4V with dissolved TiC particles, J Alloys Compd. 920 (2022) 165930. https://doi.org/10.1016/j.jallcom.2022.165930.

[30] Y. Xiao, Y. Yang, D. Wang, L. Liu, Z. Liu, S. Wu, H. Zhou, Z. Liu, C. Song, In-situ synthesis of high strength and toughness TiN/Ti6Al4V sandwich composites by laser powder bed fusion under a nitrogen-containing atmosphere, Compos B Eng. 253 (2023) 110534. https://doi.org/10.1016/j.compositesb.2023.110534.

[31]  C. Cai, J.C.D. Qiu, T.W. Shian, C. Han, T. Liu, L.B. Kong, N. Srikanth, C.-N. Sun, K. Zhou, Laser powder bed fusion of Mo2C/Ti-6Al-4V composites with alternately laminated α′/β phases for enhanced mechanical properties, Addit Manuf. 46 (2021) 102134. https://doi.org/10.1016/j.addma.2021.102134.

[32]  H.S. Maurya, K. Kosiba, K. Juhani, F. Sergejev, K.G. Prashanth, Effect of powder bed preheating on the crack formation and microstructure in ceramic matrix composites fabricated by laser powder-bed fusion process, Addit Manuf. 58 (2022) 103013. https://doi.org/10.1016/j.addma.2022.103013.

[33]  M. Tang, L. Zhang, N. Zhang, Microstructural evolution, mechanical and tribological properties of TiC/Ti6Al4V composites with unique microstructure prepared by SLM, Materials Science and Engineering: A. 814 (2021) 141187. https://doi.org/10.1016/j.msea.2021.141187.

[34]  EOS Titanium Ti64 Grade 5 Material Data Sheet Metal Solutions, n.d.

[35]  L. Thijs, F. Verhaeghe, T. Craeghs, J. Van Humbeeck, J.-P. Kruth, A study of the microstructural evolution during selective laser melting of Ti–6Al–4V, Acta Mater. 58 (2010) 3303–3312. https://doi.org/https://doi.org/10.1016/j.actamat.2010.02.004.

[36]  L. Thijs, F. Verhaeghe, T. Craeghs, J. Van Humbeeck, J.-P. Kruth, A study of the microstructural evolution during selective laser melting of Ti–6Al–4V, Acta Mater. 58 (2010) 3303–3312. https://doi.org/https://doi.org/10.1016/j.actamat.2010.02.004.

[37]  J. Xia, S. Liu, B. Zhang, Y. Chen, Central Composite Experiment Design (CCD)-Response Surface Method (RSM) to Optimize the Sintering Process of Ti-6Al-4V Alloy, Metals (Basel). 11 (2021) 197. https://doi.org/10.3390/met11020197.

[38]  C.A. Schneider, W.S. Rasband, K.W. Eliceiri, NIH Image to ImageJ: 25 years of image analysis, Nat Methods. 9 (2012) 671–675. https://doi.org/10.1038/nmeth.2089.

[39]  A. Khorsand Zak, W.H. Abd. Majid, M.E. Abrishami, R. Yousefi, X-ray analysis of ZnO nanoparticles by Williamson-Hall and size-strain plot methods, Solid State Sci. 13 (2011) 251–256. https://doi.org/10.1016/j.solidstatesciences.2010.11.024.

[40]  A.J.I. Bagasol, F.R. Kaschel, S. Ramachandran, W. Mirihanage, D.J. Browne, D.P. Dowling, The influence of a large build area on the microstructure and mechanical properties of PBF-LB Ti-6Al-4 V alloy, The International Journal of Advanced Manufacturing Technology. 125 (2023) 1355–1369. https://doi.org/10.1007/s00170-022-10671-9.

[41]  T. Pasang, B. Tavlovich, O. Yannay, B. Jakson, M. Fry, Y. Tao, C. Turangi, J.C. Wang, C.P. Jiang, Y. Sato, M. Tsukamoto, W. Misiolek, Directionally-dependent mechanical properties of Ti6Al4V manufactured by electron beam melting (EBM) and selective laser melting (SLM), Materials. 14 (2021). https://doi.org/10.3390/ma14133603.

[42]  A.A. Tanrikulu, A. Ganesh-Ram, B. Farhang, A. Amerinatanzi, Unveiling the impact of layerwise laser preheating on microstructure and mechanical response in laser powder bed fusion, J Mater Sci. (2023). https://doi.org/10.1007/s10853-023-09066-2.

[43]  P. Kumar, O. Prakash, U. Ramamurty, Micro-and meso-structures and their influence on mechanical properties of selectively laser melted Ti-6Al-4V, Acta Mater. 154 (2018) 246–260. https://doi.org/10.1016/j.actamat.2018.05.044.

[44]  E. Lee, R. Banerjee, S. Kar, D. Bhattacharyya, H.L. Fraser, Selection of α variants during microstructural evolution in *α/β* titanium alloys, Philosophical Magazine. 87 (2007) 3615–3627. https://doi.org/10.1080/14786430701373672.

[45]  Z. Zhao, J. Chen, X. Lu, H. Tan, X. Lin, W. Huang, Formation mechanism of the α variant and its influence on the tensile properties of laser solid formed Ti-6Al-4V titanium alloy, Materials Science and Engineering: A. 691 (2017) 16–24. https://doi.org/10.1016/j.msea.2017.03.035.

[46]  B. Baufeld, O. van der Biest, Mechanical properties of Ti-6Al-4V specimens produced by shaped metal deposition, Sci Technol Adv Mater. 10 (2009) 015008. https://doi.org/10.1088/1468-6996/10/1/015008.

[47]  E. Wielewski, C.R. Siviour, N. Petrinic, On the correlation between macrozones and twinning in Ti–6Al–4V at very high strain rates, Scr Mater. 67 (2012) 229–232. https://doi.org/10.1016/j.scriptamat.2012.04.026.

[48]    J. Karimi, M.S. Xie, Z. Wang, K.G. Prashanth, Influence of substructures on the selective laser melted Ti-6Al-4V alloy as a function of laser re-melting, J Manuf Process. 68 (2021) 1387–1394. https://doi.org/10.1016/j.jmapro.2021.06.059.

[49]    A. Takase, T. Ishimoto, N. Morita, N. Ikeo, T. Nakano, Comparison of Phase Characteristics and Residual Stresses in Ti-6Al-4V Alloy Manufactured by Laser Powder Bed Fusion (L-PBF) and Electron Beam Powder Bed Fusion (EB-PBF) Techniques, Crystals (Basel). 11 (2021) 796. https://doi.org/10.3390/cryst11070796.

[50]    E. Brandl, F. Palm, V. Michailov, B. Viehweger, C. Leyens, Mechanical properties of additive manufactured titanium (Ti–6Al–4V) blocks deposited by a solid-state laser and wire, Mater Des. 32 (2011) 4665–4675. https://doi.org/10.1016/j.matdes.2011.06.062.

[51]    E. Yasa, J.-P. Kruth, Microstructural investigation of Selective Laser Melting 316L stainless steel parts exposed to laser re-melting, Procedia Eng. 19 (2011) 389–395. https://doi.org/10.1016/j.proeng.2011.11.130.

[52]    J. Bedmar, J. de la Pezuela, A. Riquelme, B. Torres, J. Rams, Impact of Remelting in the Microstructure and Corrosion Properties of the Ti6Al4V Fabricated by Selective Laser Melting, Coatings. 12 (2022) 284. https://doi.org/10.3390/coatings12020284.

[53]    J. Karimi, C. Suryanarayana, I. Okulov, K.G. Prashanth, Selective laser melting of Ti6Al4V: Effect of laser re-melting, Materials Science and Engineering: A. 805 (2021) 140558. https://doi.org/10.1016/j.msea.2020.140558.

[54]    F.I. Jamhari, F.M. Foudzi, M.A. Buhairi, Effect of HIP on Porosity of Ti6Al4V Manufactured by Laser Powder Bed Fusion: A Brief Review, in: M.F. Bin Abdollah, H. Amiruddin, A.S. Phuman Singh, F. Abdul Munir, A. Ibrahim (Eds.), Proceedings of the 7th International Conference and Exhibition on Sustainable Energy and Advanced Materials (ICE-SEAM 2021), Melaka, Malaysia, Springer Nature Singapore, Singapore, 2022: pp. 22–25.

[55]    T. Mishurova, K. Artzt, B. Rehmer, J. Haubrich, L. Ávila, F. Schoenstein, I. Serrano-Munoz, G. Requena, G. Bruno, Separation of the impact of residual stress and microstructure on the fatigue performance of LPBF Ti-6Al-4V at elevated temperature, Int J Fatigue. 148 (2021) 106239. https://doi.org/10.1016/j.ijfatigue.2021.106239.

[56]    C.M. Cepeda-Jiménez, F. Potenza, E. Magalini, V. Luchin, A. Molinari, M.T. Pérez-Prado, Effect of energy density on the microstructure and texture evolution of Ti-6Al-4V manufactured by laser powder bed fusion, Mater Charact. 163 (2020) 110238. https://doi.org/10.1016/j.matchar.2020.110238.

[57]    E.H. Jimenez, A. Kreitcberg, E. Moquin, V. Brailovski, Influence of Post-Processing Conditions on the Microstructure, Static, and Fatigue Resistance of Laser Powder Bed Fused Ti-6Al-4V Components, Journal of Manufacturing and Materials Processing. 6 (2022) 85. https://doi.org/10.3390/jmmp6040085.

[58]    Z. Zou, M. Simonelli, J. Katrib, G. Dimitrakis, R. Hague, Microstructure and tensile properties of additive manufactured Ti-6Al-4V with refined prior-β grain structure obtained by rapid heat treatment, Materials Science and Engineering: A. 814 (2021) 141271. https://doi.org/10.1016/j.msea.2021.141271.

[59]    S.L. Lu, Z.J. Zhang, R. Liu, Z. Qu, S.J. Li, X.H. Zhou, Q.Q. Duan, B.N. Zhang, X.M. Zhao, W. Zhao, P. Ramasamy, J. Eckert, Z.F. Zhang, Tailoring hierarchical microstructures to improve the strength and plasticity of a laser powder bed fusion additively manufactured Ti-6Al-4V alloy, Addit Manuf. 71 (2023) 103603. https://doi.org/10.1016/j.addma.2023.103603.

[60]    K. Karami, A. Blok, L. Weber, S.M. Ahmadi, R. Petrov, K. Nikolic, E.V. Borisov, S. Leeflang, C. Ayas, A.A. Zadpoor, M. Mehdipour, E. Reinton, V.A. Popovich, Continuous and pulsed selective laser melting of Ti6Al4V lattice structures: Effect of post-processing on microstructural anisotropy and fatigue behaviour, Addit Manuf. 36 (2020) 101433. https://doi.org/10.1016/j.addma.2020.101433.

[61]    S.A. Etesami, B. Fotovvati, E. Asadi, Heat treatment of Ti-6Al-4V alloy manufactured by laser-based powder-bed fusion: Process, microstructures, and mechanical properties correlations, J Alloys Compd. 895 (2022) 162618. https://doi.org/10.1016/j.jallcom.2021.162618.

[62]    M. Simonelli, Y.Y. Tse, C. Tuck, Effect of the build orientation on the mechanical properties and fracture modes of SLM Ti–6Al–4V, Materials Science and Engineering: A. 616 (2014) 1–11. https://doi.org/10.1016/j.msea.2014.07.086.

[63]   T. Vilaro, C. Colin, J.D. Bartout, As-Fabricated and Heat-Treated Microstructures of the Ti-6Al-4V Alloy Processed by Selective Laser Melting, Metallurgical and Materials Transactions A. 42 (2011) 3190–3199. https://doi.org/10.1007/s11661-011-0731-y.

[64]   B. Vrancken, L. Thijs, J.-P. Kruth, J. Van Humbeeck, Heat treatment of Ti6Al4V produced by Selective Laser Melting: Microstructure and mechanical properties, J Alloys Compd. 541 (2012) 177–185. https://doi.org/10.1016/j.jallcom.2012.07.022.

[65]   S. Cao, Z. Chen, C.V.S. Lim, K. Yang, Q. Jia, T. Jarvis, D. Tomus, X. Wu, Defect, Microstructure, and Mechanical Property of Ti-6Al-4V Alloy Fabricated by High-Power Selective Laser Melting, JOM. 69 (2017) 2684–2692. https://doi.org/10.1007/s11837-017-2581-6.

[66]   R. Sabban, S. Bahl, K. Chatterjee, S. Suwas, Globularization using heat treatment in additively manufactured Ti-6Al-4V for high strength and toughness, Acta Mater. 162 (2019) 239–254. https://doi.org/10.1016/j.actamat.2018.09.064.

[67]   K. Zhang, W.H. Kan, Y. Liu, X. Gao, Y. Zhu, S.C.V. Lim, H. Peng, A. Huang, Microstructure control by heat treatment for better ductility and toughness of Ti-6Al-4V produced by laser powder bed fusion, Australian Journal of Mechanical Engineering. 19 (2021) 680–691. https://doi.org/10.1080/14484846.2021.2004654.

[68]   X. Yan, S. Yin, C. Chen, C. Huang, R. Bolot, R. Lupoi, M. Kuang, W. Ma, C. Coddet, H. Liao, M. Liu, Effect of heat treatment on the phase transformation and mechanical properties of Ti6Al4V fabricated by selective laser melting, J Alloys Compd. 764 (2018) 1056–1071. https://doi.org/10.1016/j.jallcom.2018.06.076.

[69]   G. Kasperovich, J. Hausmann, Improvement of fatigue resistance and ductility of TiAl6V4 processed by selective laser melting, J Mater Process Technol. 220 (2015) 202–214. https://doi.org/10.1016/j.jmatprotec.2015.01.025.

[70]   L. Facchini, E. Magalini, P. Robotti, A. Molinari, S. Höges, K. Wissenbach, Ductility of a Ti-6Al-4V alloy produced by selective laser melting of prealloyed powders, Rapid Prototyp J. 16 (2010) 450–459. https://doi.org/10.1108/13552541011083371.

[71]   K. Bartsch, B. Bossen, W. Chaudhary, M. Landry, D. Herzog, Thermal Conductivity of Ti-6Al-4V in Laser Powder Bed Fusion, Front Mech Eng. 8 (2022). https://doi.org/10.3389/fmech.2022.830104.

[72]   A. Saini, B. Pabla, S. Dhami, Developments in cutting tool technology in improving machinability of Ti6Al4V alloy: A review, Proc Inst Mech Eng B J Eng Manuf. 230 (2016) 1977–1989. https://doi.org/10.1177/0954405416640176.

[73]   A.E. Davis, A.E. Caballero, R. Biswal, S. Williams, P.B. Prangnell, Comparison of Microstructure Refinement in Wire-Arc Additively Manufactured Ti–6Al–2Sn–4Zr–2Mo–0.1Si and Ti–6Al–4V Built With Inter-Pass Deformation, Metallurgical and Materials Transactions A. 53 (2022) 3833–3852. https://doi.org/10.1007/s11661-022-06811-1.

[74]   A. Hadadzadeh, E. Asadi, S. Imam Shakil, B. Shalchi Amirkhiz, M. Mohammadi, M. Haghshenas, Indentation-derived mechanical properties of Ti-6Al-4V: Laser-powder bed fusion versus electron beam melting, Mater Lett. 301 (2021) 130273. https://doi.org/10.1016/j.matlet.2021.130273.

[75]   S.L. Semiatin, T.R. Bieler, The effect of alpha platelet thickness on plastic flow during hot working of TI–6Al–4V with a transformed microstructure, Acta Mater. 49 (2001) 3565–3573. https://doi.org/10.1016/S1359-6454(01)00236-1.

[76]   M. Strantza, R.K. Ganeriwala, B. Clausen, T.Q. Phan, L.E. Levine, D.C. Pagan, J.P.C. Ruff, W.E. King, N.S. Johnson, R.M. Martinez, V. Anghel, G. Rafailov, D.W. Brown, Effect of the scanning strategy on the formation of residual stresses in additively manufactured Ti-6Al-4V, Addit Manuf. 45 (2021) 102003. https://doi.org/10.1016/j.addma.2021.102003.

[77]   E. Ghio, E. Cerri, Additive Manufacturing of AlSi10Mg and Ti6Al4V Lightweight Alloys via Laser Powder Bed Fusion: A Review of Heat Treatments Effects, Materials. 15 (2022) 2047. https://doi.org/10.3390/ma15062047.

[78]   F.R. Kaschel, R.K. Vijayaraghavan, A. Shmeliov, E.K. McCarthy, M. Canavan, P.J. McNally, D.P. Dowling, V. Nicolosi, M. Celikin, Mechanism of stress relaxation and phase transformation in additively

manufactured Ti-6Al-4V via in situ high temperature XRD and TEM analyses, Acta Mater. 188 (2020) 720–732. https://doi.org/10.1016/j.actamat.2020.02.056.

[79]   J.C. Slater, Atomic Radii in Crystals, J Chem Phys. 41 (1964) 3199–3204. https://doi.org/10.1063/1.1725697.

[80]   G. Grewal, S. Ikem, Particle coarsening behavior of α-β titanium alloys, Metallurgical Transactions A. 21 (1990) 1645–1654. https://doi.org/10.1007/BF02672579.

[81]   L. Liu, C. Chen, R. Zhao, X. Wang, H. Tao, S. Shuai, J. Wang, H. Liao, Z. Ren, In-situ nitrogen strengthening of selective laser melted Ti6Al4V with superior mechanical performance, Addit Manuf. 46 (2021) 102142. https://doi.org/10.1016/j.addma.2021.102142.

[82]   D. He, H. Wang, W. Huang, X. Chen, G. Lian, Y. Wang, Microstructure and Mechanical Properties of LaB6/Ti-6Al-4V Composites Fabricated by Selective Laser Melting, Metals (Basel). 13 (2023) 264. https://doi.org/10.3390/met13020264.

[83]   Q. Jiang, S. Li, S. Guo, M. Fu, B. Zhang, Comparative study on process-structure-property relationships of TiC/Ti6Al4V and Ti6Al4V by selective laser melting, Int J Mech Sci. 241 (2023) 107963. https://doi.org/10.1016/j.ijmecsci.2022.107963.

[84]   E. Farabi, V. Tari, P.D. Hodgson, G.S. Rohrer, H. Beladi, On the grain boundary network characteristics in a martensitic Ti–6Al–4V alloy, J Mater Sci. 55 (2020) 15299–15321. https://doi.org/10.1007/s10853-020-05075-7.

[85]   G. Lütjering, Influence of processing on microstructure and mechanical properties of (α+β) titanium alloys, Materials Science and Engineering: A. 243 (1998) 32–45. https://doi.org/10.1016/S0921-5093(97)00778-8.

# 6. CONCLUSION AND FUTURE STUDIES

## 6.1. Conclusion

In this study, three different in-situ thermal processes of LPBF-fabricated Ti-6Al-4V material were investigated. The impact of the proposed strategies on the material's microstructure and metallurgical properties was analyzed through characterization techniques including Scanning Electron Microscopy (SEM), Energy Dispersive X-ray Spectroscopy (EDS), X-ray Diffraction (XRD), and Optical Microscopy (OM). The microstructure data was subjected to analysis performing image processing, Bragg's law, and the Williamson - Hall model to ensure accurate quantification of the findings for a reliable evaluation in the context of this Ph.D. dissertation. The microstructure modification during the proposed innovative thermal processing was validated with complementary mechanical testing. Digital image correlation (DIC) equipment was utilized during the tensile testing to measure the strain instantly and accurately both at local and global levels. Performing three different in-situ thermal processing, several outcomes were achieved for LPBF-fabricated Ti-6Al-4V.

In the first study, layerwise in-situ preheating of Ti-6Al-4V, process-induced defects, grain morphology, lattice structure, composition, and mechanical properties of the material were investigated. Findings revealed a remarkable improvement in the relative density of the material, reaching up to 99.99%. Additionally, it was observed that applied thermal processing modified the prior $\beta$ grain boundaries and the $\alpha/\alpha'$ phases. Applying a relatively low layerwise preheating energy of 26.92 $J/mm^3$ before the melting scan modifies the prior $\beta$ grain shape on the XY plane into a square form. An increase in the preheating energy to 35.90 $J/mm^3$ leads to the formation of circular prior $\beta$ grain regions on the same plane. Furthermore, the findings prove that the preheating scan prompts an increase in the thickness of $\alpha/\alpha'$ phase laths. After the preheating laser scan, each microstructure exhibits thicker $\alpha/\alpha'$ phase laths compared to the reference sample. A key finding of this study is the impact of layerwise preheating on the uniformity of $\alpha/\alpha'$ lath thickness in LPBFed samples, reducing the difference between the XY and ZX planes to only 4.7%

XRD analysis was employed for the characterization of the material's crystallography. The XRD pattern exhibited the strongest Bragg's peak at the (101) plane on the XY surface for the reference sample

without any additional laser scan. In contrast, preheated samples displayed the highest peak intensity at the (002) plane, indicating predominant grain orientation along this direction in the XY plane. The preheating scans induced a shift in microstrain from tensile to compressive, particularly notable at higher preheating scan speeds. The predominant phase of the microstructure was the HCP phase. Layerwise preheating promotes a higher c/a ratio in the samples, indicating more lattice distortion along the c-axis compared to the a-axis. A reduction in the volume of the HCP lattice with a decrease in preheating energy density was also observed. Furthermore, the research investigated the stable phases at room temperature after the decomposition of the phases.

The research also delved into the stable phases present at room temperature following the decomposition of the allotropic transformation. Preheating exerted a discernible influence on the decomposition of the $\alpha'$ phase, as evidenced by quantifying the $\beta$-phase content within the microstructure across various preheating energy densities. It is worth noting that all preheated samples exhibited a lower percentage of the $\beta$-phase compared to the reference microstructure. Microstructural images illustrated the decomposition of $\alpha'$ into $\alpha + \beta$ phases for the reference sample, while no detectable $\beta$ phase particles were observed in the preheated samples.

The first presented study unveiled the substantial impact of layerwise preheating on the mechanical properties of LPBF-fabricated Ti-6Al-4V. This included an elevation in UTS and elastic modulus, albeit with a reduction in elongation values relative to the reference sample. Notably, among the preheated samples, a UTS value of 1235 MPa was achieved, marking the highest reported for thermally processed LPBF-fabricated Ti-6Al-4V to date. Despite a reduction in elongation, the rigidity of the preheated samples exceeded that of the reference sample. The sample subjected to a preheating scan speed of 1625 mm/s (252 W, 32.32 J/mm3) exhibited an 8% increase in elastic modulus. Furthermore, the application of preheating was found to markedly influence the orientation of localized strains before rupture. This study imparts novel insights into the effects of preheating on the structure and mechanical properties of LPBF-fabricated Ti-6Al-4V, thereby setting a significant precedent for future research and potential applications in the additive manufacturing domain.

The second study investigated the Ti-6Al-4V alloy's microstructure and its mechanical response through the application of in-situ thermal processing in LPBF. This was achieved by integrating preheating and post-heating laser scans. The results from the separate applications of preheating and post-heating laser scans unveiled that the process-induced porosity defect was highly dependent on the energy value of the additional laser scans. It was observed that the reduction in porosity percentage was minimized when the energy input was maintained within the range of 25 $J/mm^3$ to 45 $J/mm^3$. In the context of this study, the fabrication parameters for the in-situ thermal process parameter were modeled using the Box-Behnken Design of Experiment (DOE) approach, ensuring that the energy input remained below 45 $J/mm^3$. The porosity level decreased to 0.01% with the application of the proposed in-situ thermal processing.

XRD analysis was performed for additional microstructure characterization. However, the impact of the in-situ thermal process on α/α′ lath thickness was insignificant compared to the individual applications of the preheating and post-heating laser scans; the impact on the HCP lattice was relatively pronounced. A similar trend with the individual preheating and post-heating application was observed which was smaller HCP lattices with higher strain value. Additionally, the XRD peak pattern changed with the application of the in-situ thermal process. It was observed the highest peak intensity transitioned from the (101) plane in the reference sample to the (002) plane in the in-situ thermally processed samples.

The third study, selective microstructure modification for high stiffness for reinforced single-material metal AM, an innovative strengthening strategy for the LPBF process was investigated. The fiber texture of the composite materials was mimicked. The pillar shape was selected to replicate the fiber function of reinforcement in the matrix. Different pillar diameters were selected according to the resolution of the LPBF technology to study the effect of the pillar size on the mechanical response of the material. The corresponding regions of the assigned pillar shape at each layer were exposed to a secondary laser scan through the sample during the fabrication.

Studied microstructure clearly demonstrated that the optimized post-heating laser scan modified the LPBF-fabricated Ti-6Al-4V alloy's microstructure by recrystallizing the $\alpha/\alpha'$ phases lath structure, stretching the HCP lattice, transforming the initial strain mode, and the inherent grain texture.

Notably, the mechanical response of the tailored microstructure for reinforcement indicated a remarkable improvement in strength. The post-heating laser scan reinforcement application was observed to limit the decrease in elongation, and even in some pillar diameters, a significant enhancement was observed.

The results apparently indicated that the proposed innovative thermal processing of the LPBF-fabricated Ti-6Al-4V during the fabrication can alternate the requirement of the complementary post-processing of heat treatment to modify the microstructure for the desired mechanical response. Additionally, results promised to strengthen the material without the requirement of auxiliary components such as nitrides, or carbides which makes the LPBF process more challenging in non-uniform chemical composition distribution.

6.2 Future Work

The future research direction could involve investigating the influence of dwell time in the multi-scan strategy. This would entail varying the dwell time between the preheating-melting laser scans and the melting-post-heating laser scans. This investigation aims to provide additional insights into the in-situ thermal processing of LPBF-fabricated Ti-6Al-4V by introducing another variable.

The strength value obtained in this study suggests that twinning may play a dominant role in the deformation of Ti-6Al-4V. Secondly, it is proposed to conduct further microstructure characterizations to elucidate the transformation of deformation mechanisms in Ti-6Al-4V. Particularly it is aimed to conduct TEM analysis.

Finally, a future avenue, extending the application of in-situ thermal processing to other AM metals is recommended. This expansion could potentially widen the engineering applications of the in-situ thermal processing for LPBF technology.